© 2021 Cristina Schlesier

MEASURING THE ANOMALOUS PRECESSION FREQUENCY OF THE MUON IN RUN 2 OF THE FERMILAB MUON G-2 EXPERIMENT

BY

CRISTINA SCHLESIER

DISSERTATION

Submitted in partial fulfillment of the requirements
for the degree of Doctor of Philosophy in Physics
in the Graduate College of the
University of Illinois Urbana-Champaign, 2021

Urbana, Illinois

Doctoral Committee:

Associate Professor Benjamin Hooberman, Chair
Professor Kevin T. Pitts, Director of Research
Professor Aida X. El-Khadra
Professor Matthias Grosse Perdekamp

Abstract

The E989 Muon $g-2$ Experiment at Fermilab aims to measure the anomalous magnetic moment of the muon, a_μ, to an unprecedented precision of 140 parts per billion (ppb). Currently, a 4.2σ discrepancy exists between the experimental value of a_μ and the theoretical value given by the Standard Model. The goal of E989 is to either confirm this discrepancy and suggest new physics, or show the discrepancy to be an error. The first result from E989 has been published [1], using data collected during Run 1, which confirms the tension between theory and experiment. A total of 5 runs are planned, increasing the amount of data by roughly a factor of 10. This thesis outlines the history, motivations, and physics of the E989 experiment, and presents a preliminary analysis of data collected during Run 2.

Determining a_μ requires a precision measurement of two main quantities: (1) the anomalous precession frequency of muons in a magnetic storage ring and (2) the magnetic field experienced by those muons. The anomalous precession frequency, ω_a must be measured with a systematic uncertainty below 70ppb in order for the collaboration to achieve its target precision. The analysis presented here concerns ω_a.

In loving memory of my grandmother
Mary Margaret Schlesier

Acknowledgments

This work would not exist without the help of countless people. First, I would like to thank my advisor, Kevin Pitts, for his guidance, patience, and support. My group members, especially Adithya Kuchibhotla and Sudeshna Ganguly, have been great teachers and friends, making my progress through graduate school not only possible but also fun. I feel particularly lucky to have come up in the physics department at UIUC, where I have been nurtured by the warm and intellectually stimulating community both in Loomis Lab and elsewhere on campus.

I am deeply grateful for the entire E989 collaboration, who have poured considerable time and energy into building up this experiment and each other. Thanks to Antoine Chapelain, Jarek Kaspar, Sabato Leo, Esra Barlas, Joe Grange, James Stapleton, Chris Polly, among many others, who all provided significant assistance or support at some point or other. Thanks to Tammy Walton, who gave me much needed encouragement during my time at Fermilab and is a scientist I deeply admire. Special thanks to Midhat Farooq who made my time in E989 richer with her inspiring dedication and friendship.

Thanks to the students that I've been fortunate enough to work with who have helped me understand teaching and learning as two sides of the same coin. Profound thanks especially to the students I met and worked with in the Education Justice Project, whose exemplary scholarship, ebullience, and sincerity have made me a better scientist and person.

Unfathomable kindness has been shown to me by the Butler-Jaffray family, who have made me feel like one of their own and made the Midwest feel like home to this Jersey girl. Big thanks to Molly for watching Donna while I worked on parts of this analysis. Thanks to Will for being a pal and a confidant. Without Will's humor, curiosity, patience, generosity, and finesse at maneuvering out of any crisis, this thesis would not have been written, as I would have probably been eaten by a bear by now.

Thanks to my friends back home and elsewhere who kept me going over the years with their love, geniality, and votes of confidence. I'm a lucky person who can claim there are too many to name, but you know who you are.

Thanks to my family for encouraging me from a young age to pursue my interests and always supporting my path, no matter how winding it may be. Thanks to my parents, Scott and Jacqueline, my brother, Jason, my grandfather, Edward, and my grandmother, Ketty. Thanks to my late grandmother Margie, who left us shortly before I started my PhD but was and continues to be a guardian and guide in my life. Thank you all for everything. I love you all dearly. ♡

My participation in this work was supported by U.S. Department of Energy award DE-SC0015640.

Table of contents

List of Abbreviations ..... **vi**
List of Symbols ..... **viii**
Chapter 1 Introduction **1**
Chapter 2 Muon $g-2$ in the Standard Model **7**
Chapter 3 History of Muon g-2 Experiments **14**
Chapter 4 The E989 Muon g-2 Experiment **18**
Chapter 5 Anomalous Spin Precession Measurement **31**
Chapter 6 SLAC Test Beam Experiment **49**
Chapter 7 Timing and Synchronization Tests **55**
Chapter 8 Anomalous Precession Frequency Analysis with Run 2 Data **63**
Chapter 9 Conclusion **98**
Appendix A Ratio Method **100**
Appendix B Pileup Corrected Bin Errors **104**
Appendix C Correlation Matrices **107**
Bibliography **112**

List of Abbreviations

BNL	Brookhaven National Laboratory
FNAL	Fermi National Accelerator Laboratory
CERN	European Council for Nuclear Research
SLAC	Stanford Linear Accelerator Center
E821	Brookhaven Muon $g-2$ experiment
E989	Fermilab Muon $g-2$ experiment
SM	Standard Model of Particle Physics
BSM	Beyond the Standard Model
LHC	Large Hadron Collider
SUSY	Supersymmetry
AMC	Advanced Mezzanine Card
DAQ	Data Acquisition
DoF	degrees of freedom
MIDAS	Maximum Integrated Data Acquisition System
μTCA	Micro Telecommunications Computing Architecture
ESQ	electrostatic quadrupole
NMR	nuclear magnetic resonance
xtal	calorimeter crystal
xtalNum	crystal number
SiPM	silicon photomultiplier
STDP	short term double pulse
OOF	out-of-fill
WFD	waveform digitizer
TTC	Timing, Trigger, and Control (protocol)
EW	Electroweak

QCD	Quantum Chromodynamics
QED	Quantum Electrodynamics
HVP	hadronic vacuum polarization
HLbL	hadronic light-by-light
FFT	fast Fourier transform
ppt	parts per thousand
ppm	parts per million
ppb	parts per billion
CBO	Coherent betatron oscillation
VW	Vertical waist
VO	vertical oscillation

List of Symbols

e^+	positron
μ^+	positive muon
τ_μ	muon lifetime
α	fine structure constant
c	speed of light
g_i	g-factor ($i = e$ for eletron, μ for muon)
a_i	magnetic moment anomaly ($i = e$ for eletron, μ for muon)
ν_i	neutrino ($i = e$ for eletron, μ for muon)

Chapter 1

Introduction

This chapter introduces the most ideas concepts required to understand the measurement presented in this thesis and the motivation for such a measurement. There is an elementary overview of spin, magnetic dipoles, magnetic moments, and spin precession. These concepts will be revisited at a higher level in subsequent chapters.

1.1 The Muon

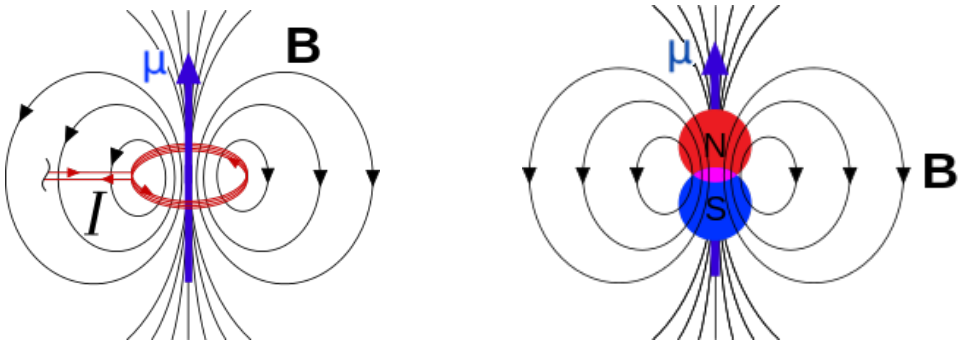
The muon is an elementary particle similar to the electron, with an electric charge of $-e$ and a spin of $\frac{1}{2}\hbar$[1]. Muons have a mass of 105.66 MeV/c^2, about 207 times that of the electron. Muons have a mean lifetime of 2.2 μs, much longer than most other unstable particles. Because muon decay is mediated by the weak interaction exclusively and because the mass difference between the muon and the set of decay products is small, muon decay is relatively slow compared to many other decay processes in the Standard Model. Muon decay always produces at least three particles, which must include an electron of the same charge as the muon and two neutrinos of different flavors. As a particle with electric charge and non-zero spin, the muon produces a magnetic dipole. The deviation of its dipole moment from the expected value motivates the Muon $g-2$ experiment.

1.2 Magnetic Dipoles

1.2.1 Classical Dipoles

A magnetic dipole, as illustrated in Figure 1.1, is an object which produces a magnetic field profile identical to the field produced by a closed loop of current, if viewed from a sufficient distance. So-called "natural" magnetic dipoles are characterized by a north and south pole which produce the dipole field in the absence of any current. Many objects produce dipole fields, including simple bar magnets, Earth, and many elementary particles. The orientation and strength of the dipole is given by its magnetic dipole moment, $\vec{\mu}$, which characterizes a dipole's ability to align itself with an external field. For a classical particle with mass m, charge q, and angular momentum $\vec{L}$, the magnetic moment is

[1] Hereafter, units are used such that $\hbar = 1$ and $c = 1$.



(a) (b)

Figure 1.1: The magnetic field due to (a) a current loop and (b) a natural magnetic dipole. Both configurations generate the same magnetic field and dipole moment when viewed from a sufficient distance.

$$\vec{\mu} = \frac{q}{2m}\vec{L} \tag{1.1}$$

The ratio of an object's magnetic moment to its angular momentum is called the gyromagnetic ratio, in the case of a charged particle, given by $q/2m$. The interaction between a magnetic moment and an external field results in a potential energy U which depends on the magnetic moment's orientation relative to the external field. A system will be in its lowest energy state when the magnetic moment is parallel to the external magnetic field $\vec{B}$, asserted by the expression below.

$$U = -\vec{\mu} \cdot \vec{B} \tag{1.2}$$

1.2.2 Quantum Dipoles

Although it is not quite correct to consider the muon as a tiny bar magnet or tiny loop of current, this line of thinking does help to conceptualize how elementary particles also produce dipole fields. As an elementary particle, the muon is point-like, meaning it has no discernible internal structure or spatial extension. This raises the question, how can a structureless, point-like object be a dipole when a dipole is consists of a pair of magnetic poles separated by some distance? Quantum mechanics provides some relief to this apparent contradiction with the concept of spin, which refers to the intrinsic angular momentum of an object. A common analogy used to convey the meaning of spin is to liken it to the angular momentum of a spinning top. However, thinking of spin as rotation about a central axis restores the aforementioned conundrum–a point particle should possess no extended volume with which to rotate. The takeaway here is that spin is a quantum property and cannot be illustrated with macroscopic analogues. Instead of focusing on the rotation of a particle, spin can simply be understood as a quantity that defines the direction of a magnetic moment of a particle. The magnetic moment, in turn, has macroscopic observable effects.

Particles in the Standard Model belong to one of two main groups, fermions and bosons, where fermions have half-integer spin and bosons have integer spin. Different mathematical objects are required to represent particles of different spins. For example, spin-0 particles, such as the Higgs boson, are understood as scalars while spin-1 particles are understood as vectors. Spin-$\frac{1}{2}$ particles are represented by spinors, which are objects comparable to vectors but with different behavior under rotation.

The expression for the magnetic moment of a quantum particle follows the classical case–the gyromagnetic ratio times the angular momentum, which in this case is spin. However, the observed gyromagnetic ratios of subatomic particles differ from the classical prediction. For muons and electrons, the gyromagnetic ratio is roughly a factor of 2 off from the classical estimate. For protons, the discrepancy is roughly a factor of 5.6. This factor, known the g-factor, or g, is included in the definition of the magnetic moment of subatomic particles.

$$\vec{\mu} = g\frac{q}{2m}\vec{s} \tag{1.3}$$

Effects due to both quantum mechanics and special relativity cause the magnetic moment to deviate from the classical value. Relativistic quantum mechanics, through the framework of quantum electrodynamics, predicts a g-factor of 2 for spin-$\frac{1}{2}$ particles, which matched measurements during the time that relativistic quantum mechanics was being developed. The basis for the calculation is Dirac's equation for an electron in an electromagnetic field. By taking the non-relativistic limit of the solution to the Dirac equation, $g_e = 2$ can be obtained. A rough sketch of the derivation is shown here. Starting with the Dirac equation, where ψ is the four-component Dirac spinor for the electron, and including a term for an external electromagnetic field, A, gives

$$(i\not{\partial} - e\not{A} - m)\psi = 0 \tag{1.4}$$

Multiplying this equation by $(i\not{\partial} - e\not{A} + m)$ results in

$$\begin{aligned} 0 &= (i\not{\partial} - e\not{A} - m)(i\not{\partial} - e\not{A} + m)\psi \\ &= (\frac{1}{4}\{i\partial_\mu - eA_\mu, i\partial_\nu - eA_\nu\}\{\gamma^{mu}, \gamma^{mu}\} + \frac{1}{4}[i\partial_\mu - eA_\mu, i\partial_\nu - eA_\nu][\gamma^{mu}, \gamma^{mu}] - m^2)\psi \end{aligned} \tag{1.5}$$

From this equation, the antisymmetric part drops out and the middle term becomes $-eiF_{\mu\nu}$, resulting in

$$((i\not{\partial} - e\not{A})^2 - \frac{e}{2}F_{\mu\nu}\sigma^{\mu\nu} - m^2)\psi = 0 \tag{1.6}$$

This equation comes with an extra term $-\frac{e}{2}F_{\mu\nu}\sigma^{\mu\nu}$ as compared to the analogous equation for spinless particles. It turns out this terms corresponds to a magnetic dipole interaction with the external field. (Spinless particles, on the other hand, have no magnetic dipole and therefore have no such interaction term.) In the non-relativistic limit, this equation reduces to a familiar Hamiltonian.

$$H = \frac{\vec{p}^2}{2m} + V(r) + \frac{e}{2m}\vec{B}\cdot(\vec{L} + 2\vec{S}) \tag{1.7}$$

Pulling out the term which defines the magnetic dipole interaction between the field $\vec{B}$ and the spin $\vec{S}$,

$$\frac{e}{2m}\vec{B}\cdot(2\vec{S}) \tag{1.8}$$

yields a coefficient of $\frac{2e}{2m}$, which gives $g_e = 2$. As the Dirac equation describes all spin-$\frac{1}{2}$ particles, this result hold for muons as well. Contemporaneous experimental measurements by Stern-Gerlach and Phipps-Taylor produced results consistent with Dirac's calculation [2]. Dirac's formulation was foundational to contemporary physics not only for his calculation of the electron g-factor, but also for the prediction of anti-matter and the theoretical justification for spin.

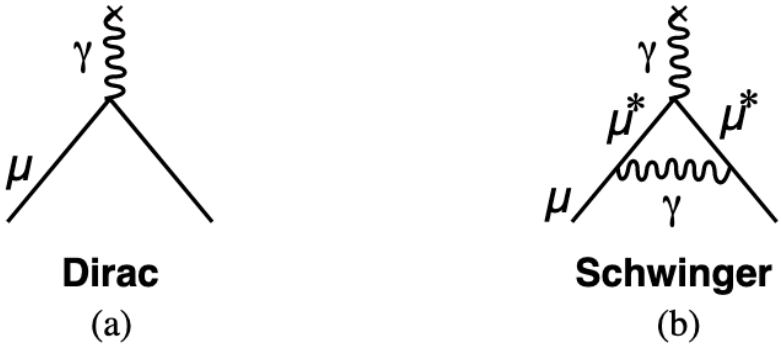


Figure 1.2: Feynman diagrams for the (a) tree-level and (b) one-loop correction to the muon magnetic moment. The diagram for Schwinger's correction shows the muon interacting with itself by way of a virtual photon. Though these diagrams illustrate interactions between a muon and an electromagnetic field, the muon could just as well be exchanged for an electron or tau.

1.3 Anomalous Magnetic Moment

However, due to other interactions beyond those predicted in relativistic quantum mechanics, the value for g_e actually deviates from 2 slightly. In fact, puzzling results started to emerge only a few years after Dirac's calculation. At the time, the proton was thought to be a spin-$\frac{1}{2}$ particle, so when Stern measured $g = 5.5$ for the proton, physicists had to consider the possibility that Dirac's formulation may not be complete. It turns out that this discrepancy between experiment and theory was not a flaw of the Dirac equation per-se but a misunderstanding of the composite nature of the proton. Regardless, this and other experiments opened the door to additional explorations of the theory. In 1947, motivated by such experiments, Julian Schwinger presented a radiative correction to the Dirac magnetic moment which appeared to account for the experimental discrepancies. Schwinger obtained the value for the electron anomaly equal to

$$a_e = \frac{g_e - 2}{2} = \frac{\alpha}{2\pi} \cong 0.00116 \tag{1.9}$$

where α is the fine-structure constant, also known as the coupling constant for the electromagnetic force. This one-loop correction to $g_e = 2$ became the first of thousands of processes that have been calculated since. These processes are represented by Feynman diagrams, such as those shown in Figure 1.2.

The dominant contribution to the anomalous magnetic moment, $a = (g - 2)/2$, comes from this one-loop diagram. Since the leading order Schwinger term depends only on α and not on mass, this means that it has the same value for electrons, muons, and taus. Most higher order contributions depend on mass, however. For example, electroweak contributions contain factors of mass-squared which means that the electroweak contribution to the muon anomaly is roughly $(m_\mu/m_e)^2 \approx 43000$ times larger than the electroweak contribution to the electron anomaly and the electroweak contribution to the tau anomaly is about 12 million times larger than electroweak contribution to the electron anomaly. More details about the Standard Model's predication for the muon anomaly can be found in Chapter 2. Any contributions due to physics beyond the Standard Model should also appear larger with increasing lepton mass, since such contributions generally scale with mass squared.

Currently, the electron anomaly a_e is known to 0.24 parts per billion while the muon anomaly a_μ is known to 0.35 parts per million [1].

1.4 Spin Precession

If a magnetic dipole finds itself in the presence of an external field, the system will have some potential energy that depends on the dipole's orientation relative to the external field. For example, when the dipole is aligned with the external field, the system is in equilibrium with minimal potential energy. Likewise, when the dipole is anti-parallel to the external field, the system has maximum potential energy which results in a tendency of the dipole to align itself with the external field. Both classical and quantum systems exhibit this property of tending towards the lowest energy state. This relationship is expressed in Equation 1.2. Given a potential energy, the dynamics of a quantum mechanical system, such as a muon in an external field, can be derived from the Hamiltonian, $H = -\lambda \vec{s} \cdot \vec{B}$, where $\lambda = g\frac{q}{2m}$. The associated time evolution operator for a system in which the magnetic field only has a z-component is

$$U(t,0) = exp(-\frac{iHt}{\hbar}) = exp(-\frac{i(\lambda Bt)S_z}{\hbar}) \tag{1.10}$$

This operator rotates the spin state about the z-axis by some angle which turns out to be $-\lambda Bt$. Thus, the system evolves in time via spin rotation about the axis of the external magnetic field with angular frequency given by

$$\omega = \frac{d\phi}{dt} = \frac{d(-\lambda Bt)}{dt} = -\lambda B \tag{1.11}$$

Spin rotation in the presence of an external magnetic field is called spin precession and results directly from the potential energy in the system. This form of spin precession is also referred to as Larmor precession.

1.5 Anomalous Spin Precession

If a charged particle in an external field has some velocity, it will not only experience spin precession due to its magnetic moment, but will also travel in a circular path due to the Lorentz force $\vec{F} = q\vec{v} \times \vec{B}$. Assuming the particle travels perpendicular to the external field, this motion has a cyclotron frequency given by

$$\vec{\omega_c} = -\frac{e\vec{B}}{m\gamma} \tag{1.12}$$

where γ is the Lorentz factor. To account for the continuous rotation of the orbiting particle's frame of reference, a relativistic correction called the Thomas precession is added to the spin precession expression.

$$\vec{\omega_s} = g\frac{e\vec{B}}{2m} - (1-\gamma)\frac{e\vec{B}}{m\gamma} \tag{1.13}$$

The combination of these two effects results in the spin rotating about the momentum direction, as in Figure 1.3. This rotation has its own frequency which is given by the difference between ω_s and ω_c and called the anomalous precession frequency.

$$\vec{\omega_a} = \vec{\omega_s} - \vec{\omega_c} = -(\frac{g-2}{2})\frac{e\vec{B}}{m} = -a\frac{e\vec{B}}{m} \tag{1.14}$$

Note that the anomalous precession frequency is proportional to $g-2$. Hence, in the absence of an anomaly, i.e. if $g = 2$ exactly, then $g - 2 = 0$ which makes $\omega_a = 0$. The spin and momentum would rotate at the same frequency and thus remain parallel at all times. The E989 experiment is based on this principle of measuring

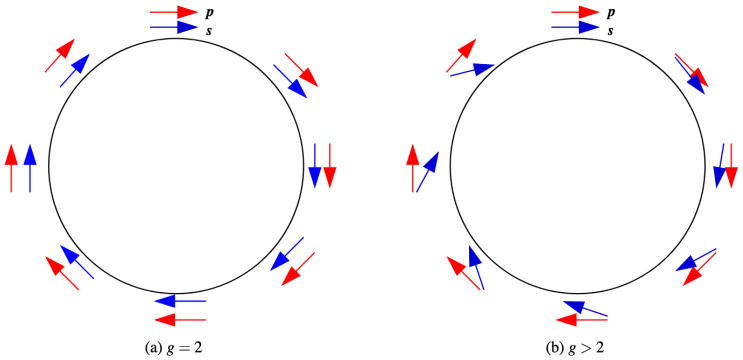


Figure 1.3: Muon spin and momentum vectors for a muon in cyclotron motion. If $g = 2$, the muon spin and momentum remain parallel during travel. If $g > 2$, the spin direction precesses around the momentum direction at ω_a.

ω_a in order to extract the anomaly directly. This will be explained in greater detail in Chapter 4.

Chapter 2

Muon $g-2$ in the Standard Model

The Standard Model of particle physics classifies the particles that constitute the building blocks of matter, as well as describing three of the four known fundamental forces. Developed in the early 1970s, it has successfully explained almost all experimental results and precisely predicted a wide variety of phenomena, including the well-known Higgs boson. By withstanding the scrutiny of many experiments, the Standard Model has been established as one of physics' most powerful theories.

In the Standard Model (SM), the three forces which mediate interactions between particles are the electromagnetic force, weak nuclear force, and strong nuclear force. These are described by quantum electrodynamics, electroweak theory, and quantum chromodynamics, respectively. The Standard Model calculation for a_μ includes three main parts, with contributions from these three theories.

$$a_\mu^{SM} = a_\mu^{QED} + a_\mu^{EW} + a_\mu^{had}$$

To understand the theoretical calculation of the anomalous magnetic moment, we essentially look at all the ways in which the muon can interact with a magnetic field. In terms of Feynman diagrams, this corresponds to any diagram with a muon coming in, a muon coming out, and an external photon line.

Around 2017, the Muon $g-2$ Theory Initiative was formed with the goal of coming to a consensus on the Standard Model a_μ value against which new experimental results should be compared. Most of the discussion that follows is informed by the work of the Theory Initiative, summarized in Ref. [3].

2.1 Quantum Electrodynamics Contribution

The quantum electrodynamics (QED) contribution to a_μ is the largest and most well understood portion of the theoretical calculation. Contributions from QED include Feynman diagrams containing leptons and photons only. Further, the smallness of the fine-structure constant α allows each higher-order term to be calculated by using perturbation theory. Because of the renormalizability of QED, all orders of a_μ are finite and calculable using Feynman diagram techniques.

$$a_\mu^{QED} = \sum_{n=1}^{\infty} A^{(2n)} (\frac{\alpha}{\pi})^n \tag{2.1}$$

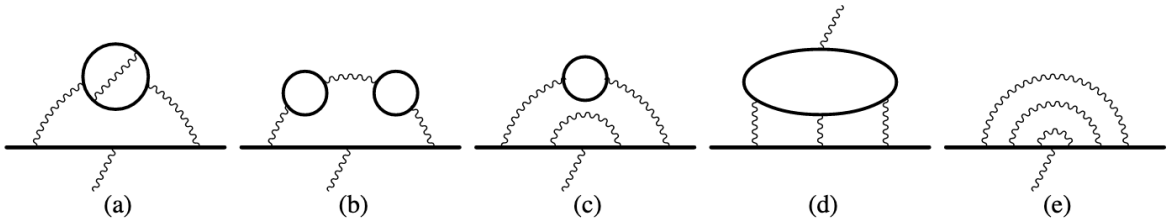


Figure 2.1: Sixth-order single-flavor diagrams. There are 72 diagrams in total; here they are divided in five groups of gauge-invariance. Solid lines represent leptons and wavy lines represent photons. Figure reproduced from Reference [4].

Since $\alpha/\pi \ll 1$, the contribution to a_μ gets increasingly smaller with each order after n=1. With a_μ^{QED} converging in this manner, a calculation to the desired precision becomes feasible.

In addition to distinguishing terms by number of loops, terms can also be distinguished by mass-dependence. That is, diagrams containing only single-flavor loops are mass-independent, while diagrams containing more than one flavor are mass-dependent. Mass-independent contributions, such as the Schwinger term, are universal for all lepton flavors (e, μ, τ) and known up to the tenth order of perturbation theory [3]. Some terms are known in closed analytic form while others are determined numerically. Examples of single flavor diagrams are shown in Figure 2.1, illustrating that even with just one flavor, there are copious diagrams to contend with.

Mass-dependent contributions can also be calculated analytically or numerically, and are known to tenth order. For the analytic calculation, there are two types of asymptotic expansion parameters, either $m_\mu/m_e > 1$ or $m_\mu/m_\tau < 1$. As mass ratios used for the calculation are experimentally determined [5, 6], they carry some uncertainty and limit the precision of a_μ^{QED}.

$$m_\mu/m_e = 206.7682827(47)$$

$$m_\mu/m_\tau = 5.94635(40) \times 10^{-2}$$

In addition to the lepton mass ratios, the fine-structure constant enters the calculation with some uncertainty. Currently, the best value of α comes from the Cesium atom-interferometry experiment [7].

$$\alpha^{-1}(Cs) = 137.035999046(27).$$

The fine-structure constant can also be determined through the extremely precise measurement of the electron anomaly, a_e [8].

$$\alpha^{-1}(a_e) = 137.0359991496(13)(14)(330)$$

The discrepancy between these two values is 2.4σ. Nevertheless, because $\alpha(a_e)$ is highly correlated to a_μ, the value α(Cs) is preferable in the final estimation of a_μ^{QED}. Recall that all mass independent terms are the same for a_e^{QED} and a_μ^{QED}.

As of 2018, all terms up to the eighth order have been calculated and independently verified by several groups using different methods. Estimates have been made up to tenth order, but the level of verification is not as robust as contributions up to eighth order. All together, the theoretical estimate for the muon

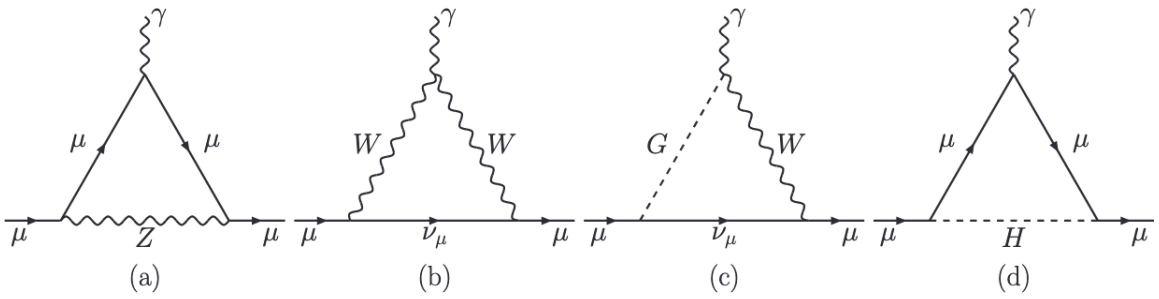


Figure 2.2: Sample diagrams for the one-loop EW contribution to a_μ. Diagrams (a) and (b) are neutral and charged currents, respectively. Goldstone bosons can enter the diagrams as in (c). The highly suppressed Higgs contribution is represented in (d). Figure reproduced from Reference [3].

anomaly due to QED is

$$a_\mu^{QED} = 116584718.931(7)(17)(6)(100)(23)[104] \times 10^{-11}$$

The uncertainties are due to the τ-lepton mass, the eighth-order QED, the tenth-order QED, the estimate of the twelfth-order QED, the fine-structure constant α, and the sum in quadrature of all of these. Apart from the respective input for α and the lepton masses, this final value is based on the latest QED calculations from Reference [9].

2.2 Electroweak Contribution

The electroweak (EW) contributions to a_μ are characterized by their inclusion of $W^\pm$, Z^0 or Higgs bosons and have been calculated up to three-loop order. Due to the large masses of these bosons, the electroweak contributions are strongly suppressed. Nevertheless, the precision on the measurement of a_μ is currently high enough to be sensitive to the EW sector.

One-loop contributions are expressed in diagrams with $W^\pm$ or Z^0 exchange, examples are shown in Figure 2.2. The coupling of the Higgs boson to the muon is small, so only the W and Z processes contribute significantly to leading order.

Analytically, the one-loop contribution can be written

$$a_\mu^{EW(1)} = \frac{G_F}{\sqrt{2}} \frac{m_\mu^2}{8\pi^2} [\frac{5}{3} + \frac{1}{3}(1 - 4s_W^2)^2] = 194.79(1) \times 10^{-11} \tag{2.2}$$

Where G_F is the Fermi constant and $s_W^2 = (1 - m_W^2/m_Z^2)$ is the on-shell weak mixing angle. Noting that the Fermi constant is proportional to $1/m_W^2$, it becomes evident that the one-loop contribution is suppressed by $(m_\mu/m_W)^2$ and hence the relative size of the EW contribution compated to the QED contribution is small.

Two-loop Feynman diagrams can contain the additional complication of a extra photon or hadronic loops. In recent years, the two-loop precision has been improved by measurements of the Higgs mass at the LHC. Unlike QED, where increasingly higher orders are significantly suppressed, second-order EW diagrams can

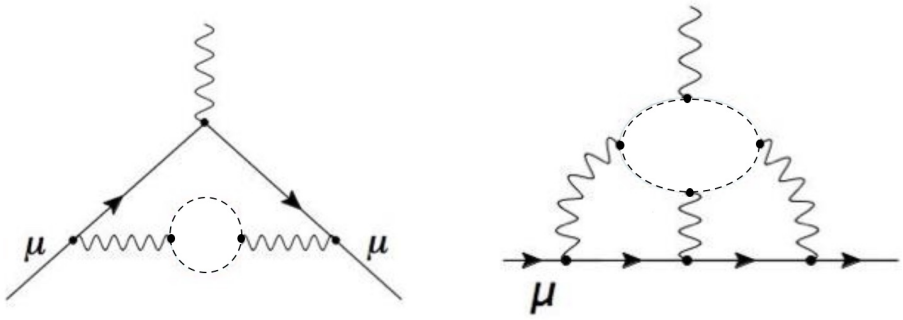


Figure 2.3: Feynman diagrams for hadronic vacuum polarization (left) and hadronic light-by-light scattering (right). Figure adapted from Reference [11].

carry closed fermion loops enhanced by a factor of $\log(m_Z/m_f)$ which makes these diagrams non-negligible compared to one-loop order. The perturbative approach does not work for all of the two-loop contributions, so other techniques must be used and some diagrams are left out of the calculation.

Taking into account everything at one-loop, all bosonic two-loop, four fermioninc two-loop, and leading order three-loop contributions gives an estimate of

$$a_\mu^{EW} = 153.6(1.0) \times 10^{-11}$$

The uncertainty cited here comes from the hadronic uncertainty in the two-loop diagrams, which is the dominant source of uncertainty for the EW contribution [10].

2.3 Hadronic Contribution

The overall uncertainty on the Standard Model value remains dominated by the strong-interaction contributions, which can be divided into two main categories: hadronic vacuum polarization (HVP) and hadronic light-by-light scattering (HLbL).

The processes that make up the HVP contribution to a_μ are those Feynman diagrams involving quarks but without $W^\pm$, Z^0, and Higgs bosons. Like the electromagnetic interaction, the strong interaction also has a coupling constant α_s and similarly the contribution to the anomaly can be expressed as a perturbative expansion in α_s. However, at low energies, α_s becomes larger than one and the series diverges, rendering the perturbative approach generally unreliable. Instead, calculations are performed with lattice QCD and data-driven approaches.

In the data-driven approach, a relation between hadronic loops and photon self-energy is exploited. The leading order contribution consists of a virtual hadron loop within a virtual photon loop. At next-to-leading order, an additional virtual photon, virtual quark or lepton loop is present. Through a dispersion relation, such contributions can be evaluated in terms of the total cross section of e^+e^- to hadrons. These data-driven results are limited by the uncertainty from experimental data though the accuracy is currently below the percent level.

Contribution to a_μ	Prediction ($\times 10^{-11}$)	Reference
QED	116 584 718.931(104)	[8]
EW	153.6(1.0)	[13]
HVP	6845(40)	[12]
HLBL	92(18)	[3]
Total	**11 659 181.0(4.3)**	

Table 2.1: Current theoretical predictions for a_μ contributions. The QED contribution is the largest part of the theory's prediction, but the hadronic terms dominate the theory's uncertainty. [14, 15, 16]

Lattice QCD operates by simulating the theory on a finite lattice in Euclidean spacetime and recovering the continuous result by taking the lattice spacing to zero and the volume to infinity. Although this technique, in principle, can achieve arbitrary precision by adjusting lattice spacing and volume, the method is extremely computing intensive. Using the data-driven results which currently provide the best precision, the leading order and next-to-leading order contributions are currently predicted to be [12]

$$a_\mu^{HVP,LO} = 693.1(4.0) \times 10^{-10}$$

$$a_\mu^{HVP,NLO} = -9.83(7) \times 10^{-10}$$

While an estimate for next-to-next-to-leading order also exists, its contribution is smaller than the uncertainty on the leading order contribution.

The a_μ contribution from hadronic light-by-light scattering is given by Feynman diagrams where four virtual photons couple to a hadronic loops. Similarly to HVP, the estimate of hadronic light-by-light scattering can be determined with dispersive approaches or lattice methods. HLbL scattering is, however, more complicated than HVP, because the LbL contributions enter through the four-point function of the LbL scattering amplitude, rather than a two-point function as in the case of vacuum polarization. At the same time, the HLbL contribution to a_μ is suppressed by an extra power of the fine-structure constant α compared to HVP and is consequently about two orders of magnitude smaller. This reduces the imperative to determine it to the same level of precision as the HVP contribution.

Though the uncertainty on the dispersive determination is smaller, the agreement between dispersive and lattice values justifies considering a weighted average for the final result. As such, the current estimates for HLbL are

$$a_\mu^{HLbL,LO} = 90(17) \times 10^{-10}$$

$$a_\mu^{HLbL,LO+NLO} = 92(18) \times 10^{-10}$$

Table 2.1 contains a summary of the Standard Model contributions discussed in these preceding sections.

2.4 Possibilities for Physics Beyond the Standard Model

Despite immense experimental success, the Standard Model of particle physics is known to be incomplete. Among other things, the Standard Model provides no explanation for neutrino oscillations or the expansion of the universe, both of which have been observed by experiment. The Standard Model leaves out gravity

and cannot yet explain why it is significantly weaker than other observed interactions. A common approach to remedy these deficiencies has been to build models which add new particles into the Standard Model. The main goal of such experiments as the Large Hadron Collider at CERN has been to detect these hypothetical particles. In the absence of any direct evidence of new particles, experiments can search for ways in which the existence of these particles can perturb other various observables, including a_μ. For example, the current discrepancy between theory and experiment in a_μ,

$$\Delta a_\mu = a_\mu^{exp} - a_\mu^{SM} = 279(76) \times 10^{-11}$$

can result from radiative corrections of an undiscovered particle [17]. The Fermilab experiment is motivated by the fact that the previous Muon $g-2$ experiment at Brookhaven found a value for a_μ that deviates from the Standard Model calculation by 3.7σ. Assuming the Brookhaven experiment holds and the theoretical calculation was done correctly, this result suggests that the Standard Model is incomplete or incorrect. In order to take seriously the possibility of physics beyond the Standard Model, this deviation must be confirmed by independent efforts. If the central values of the theoretical result and the experimental result for a_μ remain separated by at least 3σ after E989 publishes its final paper, a plethora of new physics theories will be proposed to explain the discrepancy. A few of the most promising or notable possibilities will be discussed below.

2.4.1 Complementarity of Muon g-2 to Collider Searches for New Physics

During Run 1 of the LHC, many new processes were observed, perhaps most notably the existence of a Higgs-like boson. However, no new physics has come from either Run 1 or Run 2, which leave many open questions unanswered, especially questions surrounding the nature of dark matter or the origin of flavor/grand unification. Unravelling the existence and the properties of any physics beyond the Standard Model thus requires experimental information complementary to the LHC. Muon $g-2$ is one of such complementary efforts, along with searches for charged lepton flavor violation, electric dipole moments, and rare decays. In fact, the muon magnetic moment has a special role because it is sensitive to a large class of models related and unrelated to electroweak symmetry breaking and because it combines several properties in a unique way: it is a flavor- and CP-conserving, chirality-flipping and loop-induced quantity. In contrast, many high-energy collider observables at the LHC are chirality-conserving, and many other low-energy precision observables are CP-or flavour-violating. These unique properties make a_μ an important quantity to be tested with high precision.

2.4.2 Varieties of New Physics

Two particularly promising classes of models which could naturally explain a deviation as large as Δa_μ are dark sector models and SUSY models. Dark sector models involve very light new particles with very weak interactions. They are constrained by other low-energy observables, such as $g-2$ of the electron, but there is a natural window in parameter space, where they can accommodate large contributions to a_μ. These models are not strongly constrained by LHC data. The situation is very different for SUSY models. SUSY searches are a central part of the LHC experiments which have not revealed any evidence for SUSY particles, so SUSY models are already strongly constrained by current data.

The LHC is sensitive to virtually all proposed weak-scale extensions of the Standard Model, ranging from supersymmetry, extra dimensions and technicolor to little Higgs models, unparticle physics, hidden sector

models and others. However, even if the existence of physics beyond the Standard Model is established, it will be far from easy for the LHC alone to identify which of these or not-yet-thought-of alternatives is at play. Typically LHC data will be consistent with several alternative models.

On the other hand, a situation where the LHC finds no physics beyond the Standard Model but the measurement of a_μ establishes a deviation, might be a signal for dark sector models such as the secluded U(1) model [18], with new very weakly interacting light particles which are hard to identify at the LHC.

Also, if new physics is realized in the form of a non-renormalizable theory, a_μ might not be fully computable but depend on the ultraviolet cutoff. Randall-Sundrum or universal extra dimension models are examples of this situation. In such a case, the a_μ measurement will not only help to constrain model parameters but it will also help to get information on the ultraviolet completion of the theory.

The anomalous magnetic moment of the muon is sensitive to contributions from a wide range of physics beyond the Standard Model. It will continue to place stringent restrictions on all of the models, both present and yet to be considered. If physics beyond the Standard Model is discovered at the LHC or other experiments, a_μ will constitute an indispensable tool to discriminate between very different types of new physics, especially since it is highly sensitive to parameters which are difficult to measure at the LHC. If no new phenomena are found elsewhere, then it represents one of the few ways to probe physics beyond the Standard Model. In either case, it will play an essential and complementary role in the quest to understand physics beyond the Standard Model at the TeV scale.

Chapter 3

History of Muon g-2 Experiments

The experimental measurement of $g-2$ has a long history extending back to the 1950s at CERN. Around this time, it was thought that the muon should have an extra interaction that would distinguish it from the electron and explain its higher mass. Whatever the source, the new field should have its own quantum fluctuations, and therefore give rise to an extra contribution to the anomalous moment. The first $g-2$ experiment was expected to test for the existence of such fields. When parity violation was discovered in 1957, it was found that highly polarized muon beams produced decay electrons with an angular distribution that could indicate the muon spin direction as a function of time. A wide variety of muon precession and spin-resonance experiments would be carried out in the following years. Cyclotrons at CERN and Berkeley housed the first experiments, until the muon storage ring was developed in the 1960s. At the time of these experiments, both theoretical calculations and experimental measurements had large errors, so these CERN measurements validated the theory. There was no a_μ discrepancy at the end of CERN III.

After the CERN experiments wrapped up, advances in the Standard Model calculation slowed to the point that physicists could not justify repeating the experiment with improved precision. The measurement wasn't made again for almost 20 years, when it was performed at Brookhaven National Lab.

While the three CERN experiments all found results for a_μ that were consistent with theoretical expectations at the time, only QED and hadronic contributions had been observed. The last CERN $g-2$ experiment published its final results in 1979, around the same time that electroweak theory became an established part of the Standard Model. Eventually, this development provided new motivation to repeat the $g-2$ experiment with higher precision in order to observe the electroweak contribution, as well as possible new physics contributions. The first plans for the following muon $g-2$ experiment began to come together at Brookhaven in the mid 1980s. Design elements from the final CERN experiment, such as electrostatic

Experiment	$a_\mu \times 10^{-10}$	Reference
CERN I	11 450 000(22000)	[19]
CERN II	11 661 600(3100)	[20]
CERN III	11 659 240(850)	[21]
BNL	11 659 208.0(6.3)	[22]

Table 3.1: A summary of previous measurements of a_μ done at CERN and Brookhaven National Laboratory.

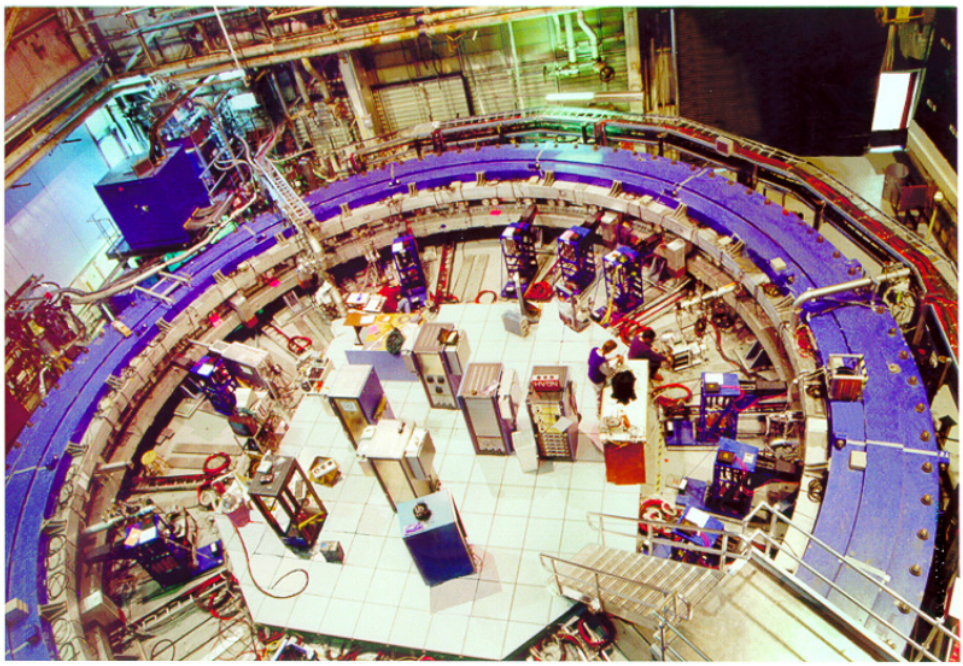


Figure 3.1: A photograph of the muon storage ring in the experimental hall at Brookhaven National Lab.

focusing and a special muon momentum at which the electric field contribution to ω_a would cancel, became essential in the Brookhaven experiment. These components, along with several significant improvements, including the inflector, fast muon kicker, NMR trolley, and superconducting storage ring magnet, remain part of the Fermilab Muon $g-2$ design as well.

Brookhaven's Muon $g-2$ experiment (E821) ran from 1997-2001 with reduced systematics and higher statistics than the CERN experiments, which gave the measurement sensitivity to EW and HLbL contributions. At the end of the Brookhaven experiment, a tension between theory and experiment was observed that has persisted over the intervening years. To resolve this tension, an experiment would need to produce more statistics to drive down the errors. Brookhaven's muon source, however, could not produce the required luminosity, so plans were made to move the experiment to Fermilab, where a higher-intensity muon source could be produced from the the decomissioned and repurposed Tevatron.

The next generation of muon $g-2$ experiments, Fermilab E989 and J-PARC E34, take different approaches and will have different systematics. The experiment at J-PARC will use a very cold, highly polarized, high intensity muon beam, at 320 MeV. By using ultra-cold muons, with almost no transverse dispersion, the muons can be stored for the duration of their lifetime without requiring a focusing field. Therefore, one is not forced to use the special momentum required in E989 to cancel out the electric field contribution to ω_a. The muon beam will be injected into the 3 T storage field using spiral vertical injection. With a storage ring diameter of 66 cm, the cyclotron period will be a short 7.4 ns compared to the 149 ns cyclotron period of E989. Positrons from muon decays carrying the ω_a signal will spiral in the field and be tracked using an array of radial vanes made up of silicon detectors.

By contrast, Fermilab E989, which began running in 2018, measures $g-2$ similarly to its predecessor, Brookhaven E821, by injecting polarized muons into a storage ring and measuring the precession frequency via the energy of decay electrons. At the time of this writing, the first result from E989 has been published



Figure 3.2: The Muon $g-2$ storage ring arrived at Fermilab in the summer of 2013, after completing a journey by land and sea from Long Island, NY, where Brookhaven National Lab is located.

[1]. Three other papers were published along with the result, which give detailed accounts of the anomalous spin precession measurement, magnetic field measurement, and beam dynamics in Run 1 [23, 24, 25]. The Run 1 analysis found $a_\mu = 116592040(54) \times 10^{-11}(0.46 \text{ ppm})$, which is 3.3σ greater than the Standard Model prediction and in agreement with the previous E821 measurement. Combining the E989 Run 1 measurement with all previous measurements from E821 results in $a_\mu = 116592061(41)10^{-11}(0.35\text{ppm})$, carrying a 4.2σ deviation from the Standard Model prediction, shown in Figure 3.3.

The following chapter contains the full details of the principles which enable the Fermilab experiment.

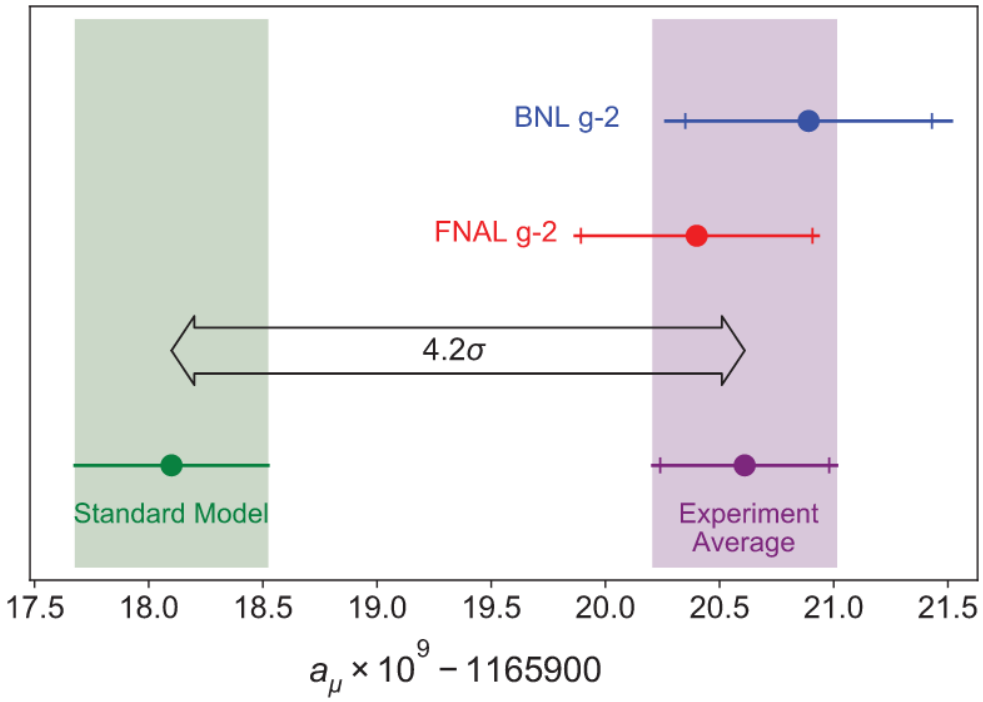


Figure 3.3: The experimental values of a_μ from E821, E989 Run 1, and the combined average. The inner tick marks indicate the statistical contribution to the total uncertainties. The Standard Model value comes from the Muon g-2 Theory Initiative [3].

Chapter 4

The E989 Muon g-2 Experiment

The strategy of E989 depends on making two distinct measurements which are combined to determine $g-2$. Those two measurements are the anomalous spin precession frequency of the muon, ω_a, and the magnetic field strength experienced by the muon, ω_p. This chapter will present the overall principles of the experiment. Chapters 5 will provide an in-depth account of the ω_a measurement and Chapter 8 will present a preliminary ω_a analysis.

4.1 $g-2$ Measurement Principle

Although the goal of E989 is to determine the magnetic moment of the muon, we actually do not measure the magnetic moment directly, but rather the interaction between the magnetic dipole and an external magnetic field. As discussed in Chapter 1, a charged particle in an external magnetic field will experience both cyclotron motion and spin precession. When the frequencies of the cyclotron motion and spin precession are different, as in the case of the muon, an anomalous precession frequency, ω_a, results. This frequency is directly proportional to $g-2$, as shown in Equation 1.14. However, ω_a is not adequate on its own to determine $g-2$.

$$a_\mu \equiv \frac{g-2}{2} = -\frac{m\omega_a}{eB} \tag{4.1}$$

The magnetic field, muon mass, and muon charge must also be determined to high precision. The magnetic field measurement is done with proton NMR, as it is the only measurement technique with the required sensitivity. Measured this way, the lab-frame magnetic field is expressed in terms of the free proton angular precession frequency, ω_p,

$$B = \frac{\hbar\omega_p}{2\mu_p} \tag{4.2}$$

Expressing B in terms of ω_p, the muon anomaly becomes

$$a_\mu = \frac{2\omega_a m_\mu \mu_p}{\hbar e \omega_p}$$

Substituting $e = \frac{4m_e\mu_e}{\hbar g_e}$ gives an expression for a_μ in terms of quantities measured precisely in other experiments.

$$a_\mu = \frac{g_e}{2}\frac{\omega_a}{\bar{\omega_p}}\frac{m_\mu}{m_e}\frac{\mu_p}{\mu_e} \tag{4.3}$$

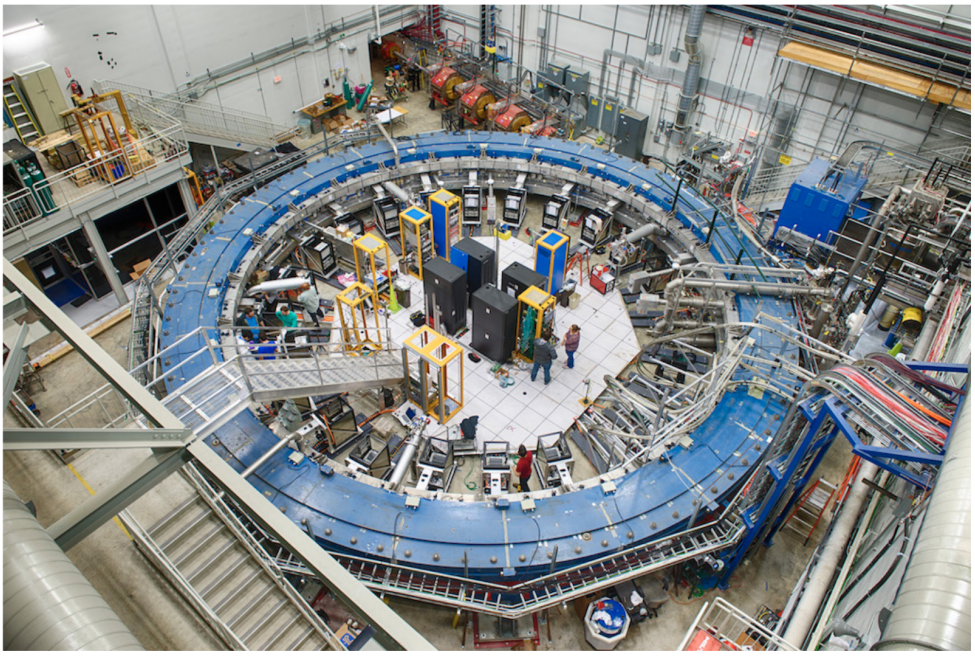


Figure 4.1: Overhead view of the E989 storage ring at Fermilab.

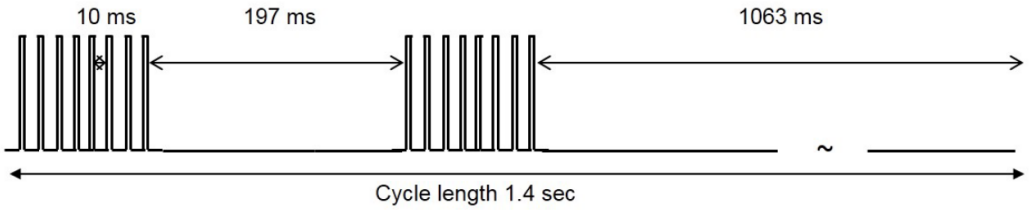


Figure 4.2: Timing structure of beam sent to the Muon $g-2$ storage ring.

As a reminder, g_e is the electron g-factor, m_μ/m_e is the ratio of the muon mass to the electron mass, μ_p/μ_e is the ratio of the proton magnetic moment to the electron magnetic moment. The Fermilab experiment will measure ω_a and $\bar{\omega_p}$, where $\bar{\omega_p}$ is the muon distribution weighted spatial average of ω_p.

Of course, it should be noted that with a beam of precessing muons, a coherent signal for the anomalous spin precession frequency will only be observed if the muons are polarized at injection time. The following sections give more details into how a beam of polarized muons are created, and how the anomalous spin precession frequency is captured in decay positron data.

4.2 Muon Production

Muons are injected into the storage ring with a specific time structure, illustrated in Figure 4.2, designed to deliver optimal flux to the detectors for measuring ω_a. Production of bunched muons begins with bunched protons that are accelerated to 8 Gev in Fermilab's linac and booster synchotron. The proton bunch then enters the much larger recycler synchotron where it is formed into a series of shorter (120 ns) bunches. Sixteen

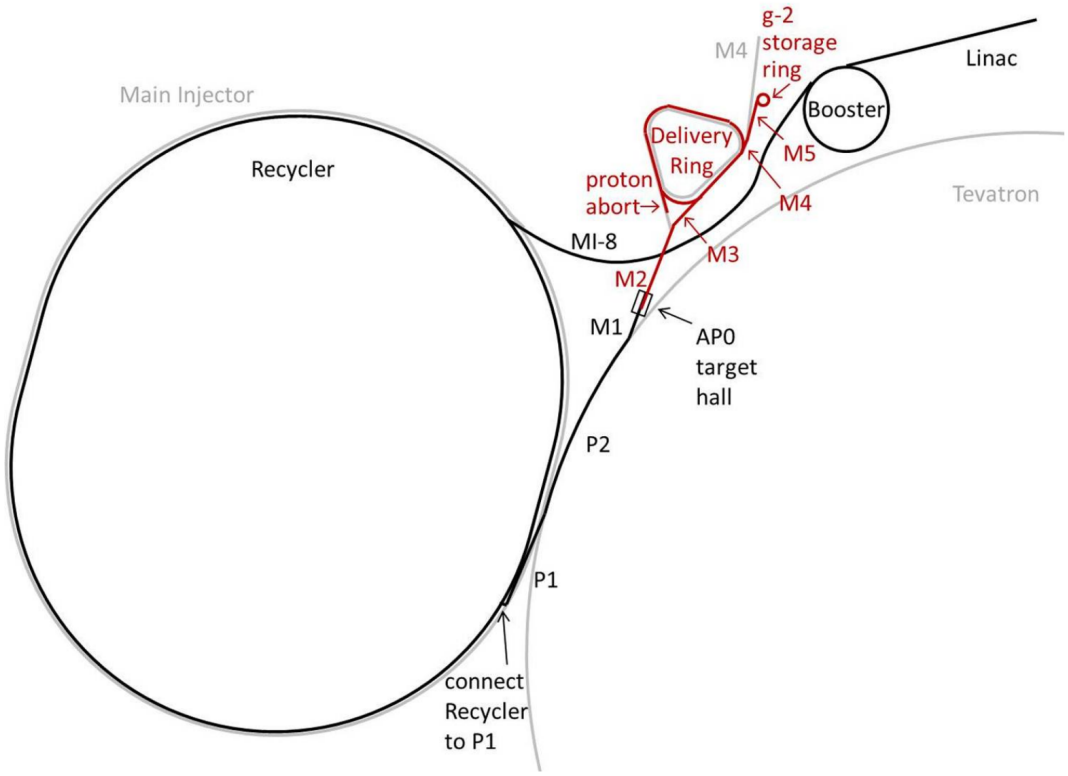


Figure 4.3: The path to the muon storage ring begins with protons, which are accelerated in the Linac and Booster, are re-bunched in the Recycler, ending up at the AP0 target hall. The resulting pion beam then travels through the M2 and M3 lines, around the Delivery Ring, and then through the M4 and M5 lines to the muon storage ring. Figure reproduced from Ref. [27]

proton bunches make a cycle, where each cycle has a duration of 1.4 s and each proton bunch contains 10^{12} protons. One by one, the proton bunches are sent to collide with a high-Z target. As a result, charged pions emerge from the proton-nucleus interactions between the beam and the target.

Pions with an energy of 3.11 GeV/c $\pm$ 10% are captured and moved through a beam line of focusing and defocusing elements, designed to capture muons from the weak decay:

$$\pi^+ \rightarrow \mu^+ + \nu_\mu$$

This decay mode is the primary mode with a branching fraction greater than 99.98% [26].

Harnessing the parity-violating nature of the weak interaction in combination with momentum selection results in a highly polarized muon beam. In the pion's rest frame, the muon and neutrino must be emitted with equal and opposite momenta in order to conserve linear momentum. With the pion having zero spin, this forces the muon to have the same handedness as the neutrino in order to conserve angular momentum. As a consequence, in the lab frame, the muon momentum direction and spin become correlated. In the case of positive muons, such as those used in E989, spin and momentum are anti-parallel. The highest energy decay muons are produced with their momenta and spin along the boost axis in the rest frame, which means they are polarized along the pion momentum in the lab frame. By capturing only the highest energy decay muons, a 95% polarized muon beam is achieved.

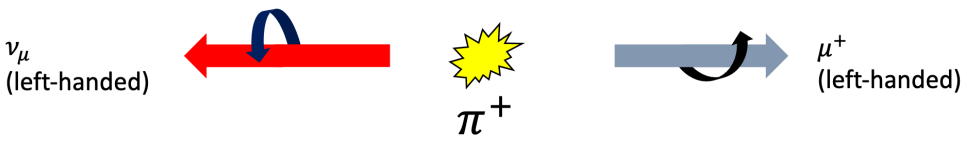


Figure 4.4: Parity violating two-body weak decay of pion. Selecting 3.094 GeV/c muons from 3.11 GeV/c pion decays yields a muon beam with a net polarization of about 95%. Figure reproduced from Reference [30].

By the time the beam reaches the end of the line, approximately 80% of the pions have decayed into muons. In addition to pions, there will also be some proton and deuteron contamination that must be separated out before the beam is injected into the storage ring. This is done by circulating the beam in the delivery ring for a few turns. By the time particles get to the delivery ring, they have 3.094 GeV/c. Due to the muon's light mass compared to the unwanted particles, muons will travel faster and get ahead of the other particles as they fly around the delivery ring. When the beam has circulated four times, the protons will be 100 m behind the muons. Taking the temporal width of the beam bunches into account, the gap between the muon beam and proton beam will be 200 ns after four turns. Contaminating pions will decay away as they have a shorter lifetime than muons.

However, at this point, the beam is now contaminated by positrons from the muon decay. This beam then traverses the final stretch of beamline before being injected in the storage ring by way of an inflector magnet, which cancels the storage ring fringe field at the point of injection. Synchrotron radiation, though negligible for muons, causes the loss of all beam positrons within $4\mu s$ of injection [28]. The final delivered muons have a momentum spread of 3.094 GeV/c $\pm$2% and a temporal spread of 120 ns [29]. This momentum, known as the "magic" momentum, is chosen so that the electric field contribution to the anomalous spin precession will cancel, simplifying the analysis. More details about the magic momentum are provided in Section 4.5.

4.3 Muon Storage

Muons from the final stretch of beamline finally arrive at the $g-2$ storage ring. To enter the storage ring, muons pass through an aperture where a superconducting inflector magnet cancels the 1.45 T storage ring field over a 1.7 m path. The exit of the inflector is not aligned with the center of the storage region, however, so the beam must be shifted onto the proper orbit in order to store. As the beam leaves the inflector, a kicker magnet fires with a pulse ideally less than the cyclotron period, so that each particle is only kicked once. The kick shifts the orbit by 77 mm.

Regardless of the inflector or kicker, muons in the ring are not perfectly perpendicular to the magnetic field. Consequently, the Lorentz force due to the magnetic field will act on parallel components of the momentum and drive particle loss. To prevent massive losses, electrostatic quadrupole plates are installed inside the ring to provide vertical focusing. Figure 4.6 shows the field lines of the electrostatic quadrupole fields. The storage ring and the electrostatic quadrupoles together provide focusing fields in both the vertical and radial directions.

Quadrupoles are also used during injection to perform scraping, which is the process of charging the quads asymmetrically to force out particles at the edge of storable phase space. Particles on the edge can also strike one of the copper collimators, causing them to fall out of orbit. Scraping lasts for about 7μs after

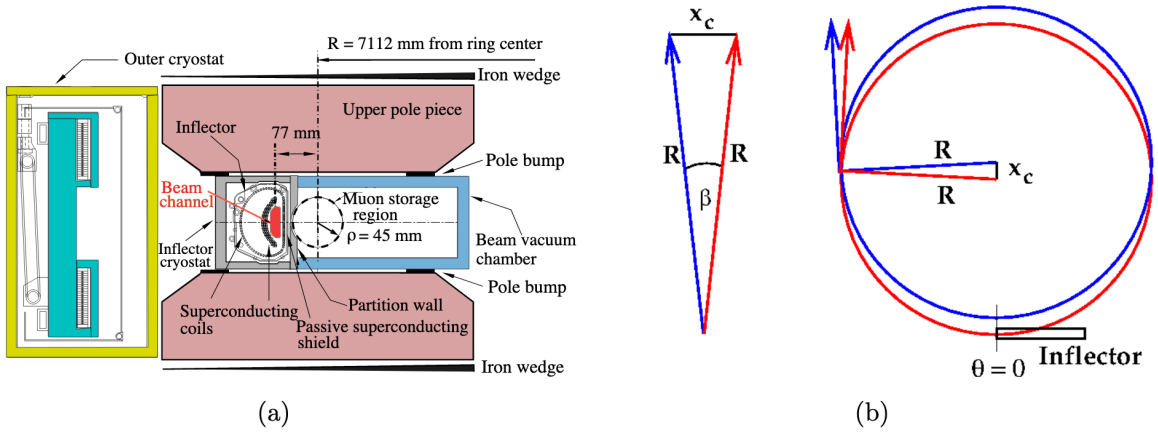


Figure 4.5: (a) The inflector exit showing the incident beam center 77 mm from the center of the storage region. The incident muon beam channel is highlighted in red. (b) The geometry of the necessary kick. The incident beam is the red circle, and the kick effectively moves the red circle over to the blue one. [27]

injection, beyond which the quads are charged to their nominal voltages. By 30μs into the fill, the muon beam is centered on the correct orbit.

Stored muons travel an average of several hundred turns around the ring before they decay. The storage ring is composed of superconducting coils and over 700 tons of iron yoke which create the 1.45 T dipole magnetic field seen by the muons. Between the poles of the magnet, there are vacuum chambers that enclose the quadrupole plates, tracking detectors, and numerous other equipment. As they traverse the ring at the magic momentum of 3.09 GeV/c and with a cyclotron period of 149.2 ns, the muons decay by the weak interaction into a positron and two neutrinos.

$$\mu^+ \rightarrow e^+ + \nu_e + \bar{\nu_\mu}$$

The resultant positron does not have enough momentum to stay in orbit and is pulled by the magnetic field towards the center of the ring. Once the positron leaves the ring, it may enter one of the 24 calorimeters. The calorimeter measures the energy deposited by the positron and the associated time. Counting decay positrons versus time is the core of the anomalous spin precession measurement. More details about the ω_a measurement from calorimeter data are given in Section 4.6. With this data of positron counts from the calorimeter, the rate at which the muon spin precesses about the momentum, ω_a, is determined. This rate is given by [22]

$$\vec{\omega_a} = -\frac{q}{m}[a_\mu \vec{B} - (a_\mu - \frac{1}{\gamma^2 - 1})\frac{\vec{\beta} \times \vec{E}}{c}] \tag{4.4}$$

As shown in Chapter 1, ω_a depends linearly on the applied magnetic field. Unlike the example given in Chapter 1, however, an electric field is also present in addition to the magnetic field. The expression for ω_a above demands a precision measurement of the electric field experienced by the muons. Luckily, there is a momentum, $p = mc/\sqrt{a_\mu} = 3.09$ GeV/c, at which the electric field contribution cancels in the first order. This is the momentum referred to as the magic momentum in Sec 4.2, and is the target momentum for the muon ensemble in the experiment. At the magic momentum, $\gamma = 29.3$.

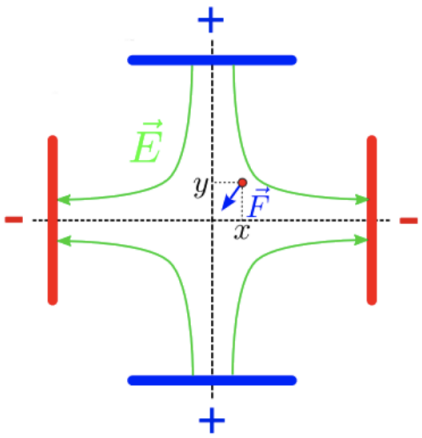


Figure 4.6: Electric quadrupole field, providing a vertical restoring to particles that travel between the plates.

4.4 Muon Beam Dynamics

The behavior of the beam in the storage ring directly affects the measurement of both ω_a and ω_p. The basic model used for fitting the time spectrum of positron events in the calorimeter assumes that all muons are on perfectly circular orbits with identical momenta and uniform azimuthal distribution. Since these stringent requirements cannot exist in a real experiment, a thorough understanding of the various beam dynamics effects is required to provide a correct model to positron data. The discussion that follows draws from References [27, 29, 31], where readers will find more details.

The storage ring accepts a range of momenta around the magic momentum of $\pm 0.5\%$. These muons pass through the magnetic field of the ring and the electric field of electrostatic quadrupoles as they travel around the ring. If field conditions are ideal, the electric and magnetic fields are given by the following equations in cylindrical coordinates,

$$\vec{E} = k(\rho - R_0)\hat{\rho} - ky\hat{y} \tag{4.5}$$

$$\vec{B} = B_0\hat{y} \tag{4.6}$$

where k is a scaling factor for the field strength and R_0 is the center of the electrostatic quadrupole field.

In the case of the electric field, this requires electrostatic quadrupoles to be perfectly aligned and everywhere in azimuth. For the magnetic field, this simply requires a uniform field with vertical component only. Both these requirements are not met in E989. Electrostatic quadrupoles only cover 43% of the ring's azimuth and were installed by hand, making perfect alignment nearly impossible. The magnetic field, while highly uniform, has higher-order multipoles which contribute small non-vertical components to the field. Regardless, the fields in Equations 4.5 and 4.6 are fair approximations for reality. The differential equations of motion for this system are:

$$\ddot{y} = -\frac{eky}{m\gamma} \tag{4.7}$$

$$\rho\ddot{\theta} = -\dot{\rho}(\frac{eB_0}{m\gamma} + 2\dot{\theta}) \tag{4.8}$$

$$\ddot{\rho} = \dot{\theta}\rho(\dot{\theta} + \frac{eB_0}{m\gamma}) + \frac{ek(\rho - R_0)}{m\gamma} \tag{4.9}$$

Under these circumstances, a muon stored at the center of the storage region ($y = 0$, $\rho = R_0$) will not oscillate in any transverse direction and will move around the ring with cyclotron frequency

$$\ddot{\theta} = \omega_c = -\frac{eB_0}{m\gamma}$$

Since this motion only has an azimuthal compoment, we can write $\rho\ddot{\theta} = v$. From this equation for ω_c, we get momentum $p_0 = \gamma mv = eR_0B_0$. The storage ring is designed with the right R_0 and B_0 to result in an accessible p_0 of 3.094 GeV/c.

Next, we can explore the motion of a muon that is not on the perfect orbit. This muon will have some vertical and radial motion. The purpose of the quadrupole field is to provide a vertical restoring force while the combination of the quadrupole field and the magnetic field provide radial focusing. Vertical motion will be determined by equation $\ddot{y}$ which has solutions of a simple harmonic oscillator. In terms of the cyclotron frequency, Equation 4.7 becomes

$$\ddot{y} = -\frac{kR_0}{vB_0}y\omega_c^2 = -ny\omega_c^2 \tag{4.10}$$

where $n = \frac{kR_0}{vB_0}$ is a quantity known as the field index which determines, among other things, the angular acceptance of the ring. This equation indicates that vertical perturbations from the center of the storage region will result in simple harmonic motion with angular frequency $\omega_y = \sqrt{n}\omega_c$. These oscillations are referred to as vertical betatron oscillations.

To understand radial perturbations from the ideal orbit, we can consider a small deviation from $\rho = R_0$.

$$\rho = R_0 + x \tag{4.11}$$

Since the storage ring aperture is about 45 mm in radius and R_0 is about 7112 mm, perturbations in ρ are less than one percent. Thus, higher orders of the perturbations in x can be neglected. Inserting the solution for ρ from Equation 4.11 into the equations of motion (Equations 4.7-4.9) and ignoring higher order terms results in

$$\ddot{x} = (\frac{ek}{m\gamma} - \omega_c^2)x = -(1-n)\omega_c^2 x \tag{4.12}$$

According to this equation, small perturbations from the ideal orbit result in simple harmonic motion in the radial direction with angular frequency $\omega_x = \sqrt{1-n}\omega_c$. These oscillations are referred to as horizontal betatron oscillations. We can see from this expression for ω_x that the field index can be no greater than 1. In E989 the value for n is generally between 0.1 and 0.15.

The preceding discussion tells us what happens to muons at the correct momentum but slightly off orbit. If muons also deviate in momentum, the equilibrium radii for these muons will also change. The ideal orbit at the center of the quadrupole potential is only accessible to muons at the magic momentum p_m. Muons at other momenta will have equilibrium orbits other than $R_0 = 7112$ mm. The equilibrium radius for a muon with $p \neq p_m$ will be the radius where the muon undergoes uniform circular motion. This can be determined by finding the radius where centripetal acceleration is constant. In general the centripetal force due to these particular electric and magnetic fields on a muon with no vertical perturbation takes the form

$$\vec{F} = e(vB_0 + k(\rho - R_0))\hat{\rho} \tag{4.13}$$

In the case of $\rho = R_0 + x$ we get a centripetal acceleration of

$$\frac{v^2}{R_0 + x} = \frac{e}{m\gamma}(vB_0 + kx) \tag{4.14}$$

The equilibrium radius as a function of the momentum deviation is

$$x_{eq} \approx \frac{R_0}{1-n}(\frac{\Delta p}{p_0}) \tag{4.15}$$

This equation shows that higher momentum muons are stored at higher radii while lower momentum muons are stored at lower radii. The field index also plays a role in how much muons diverge. A larger field index will force off-momentum muons further away from the center of the storage region.

Momentum deviation also changes the cyclotron frequency which, in turn, changes the horizontal and vertical betatron oscillations. In general the cyclotron frequency is $\omega_c = v/R$. In the case of off-momentum muons, R becomes $R + x$. The velocity, on the other hand, can be left as is because the highly relativistic speeds will not change significantly with changing momentum. Therefore, the cyclotron frequency for these off-momentum muons becomes

$$\omega_{c'} = \omega_c(1 - \frac{\Delta p/p_0}{1-n}) \tag{4.16}$$

Similarly to magic momentum muons, other muons will also oscillate about their equilibrium orbits with betatron frequencies close to those of magic momentum muons. For magic momentum muons, these frequencies are given by

$$\omega_x = \sqrt{1-n}\omega_c \tag{4.17}$$

$$\omega_y = \sqrt{n}\omega_c \tag{4.18}$$

In the factors $\sqrt{1-n}$ and $\sqrt{n}$ are the horizontal and vertical tunes but for off-momentum muons the tunes include the addition of a linear term called the chromaticity. Calculation of the x and y chromaticities involves an analysis beyond the ideal model used thus far. However, without deriving the exact expression for the off-momentum tunes, we can see from the linear relationship between $\omega_{x,y}$ and ω_c that the deviation in betatron frequencies is the same order of magntitude as the deviation in momentum.

In terms of what frequencies are actually observed, we must consider that fact that detectors around the ring measure the beam in discrete places, capturing slices of beam that depend on azimuth. As it turns out, the horizontal beam oscillation frequency ω_x is larger than half the cyclotron frequency, so there is an aliasing effect. The signal that is actually observed in the detectors of the experiment is called coherent betatron oscillation (CBO) and is related to ω_x by

$$\omega_{CBO} = \omega_c - \omega_x. \tag{4.19}$$

In the case of vertical beam oscillations, ω_y is fast enough as to get averaged out in data. However, detectors are sensitive to the oscillation of the vertical width of the beam which is aliased and related to ω_y by

$$\omega_{VW} = \omega_c - 2\omega_y. \tag{4.20}$$

Treatment of coherent betatron oscillations and vertical waist signals in the data are discussed in detail in Chapter 8. The main takeaway from this section should be that under near-ideal circumstances, muons

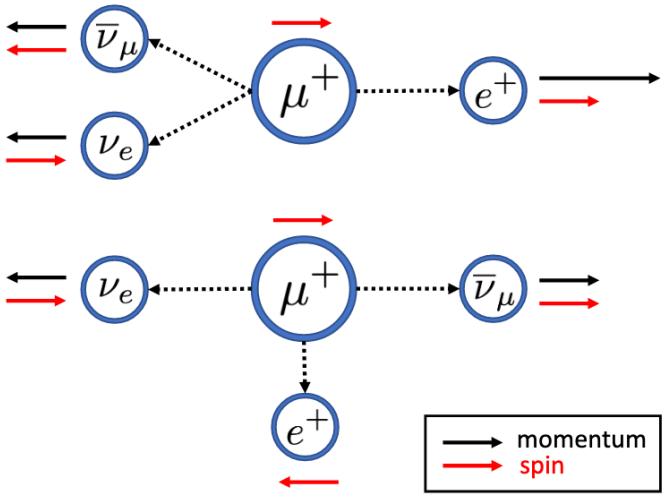


Figure 4.7: Two ends of the positron energy spectrum are illustrated here in the muon rest frame. The drawing on top shows the muon decay when positron energy is maximal and the drawing on the bottom shows muon decay when positron energy is minimal. Figure reproduced from Reference [32].

will undergo simple harmonic motion in both horizontal and vertical dimensions. The frequencies of these oscillations will be determined by the field index, n, which results from the particular configuration of the quadrupole system and the observed frequencies are aliased by the sampling rate of the detectors.

4.5 Muon Decay

Muons stored in the ring have a time-dilated lifetime of 64.4 μs. By the end of the 700 μs measuring period known as a fill, nearly all muons have decayed through the three-body decay channel

$$\mu^+ \rightarrow e^+ + \nu_e + \bar{\nu_\mu}$$

with a branching fraction close to 100% [26]. Like , muon decay also proceeds through the weak interaction and violates parity. The correlation between the decay positron momentum and muon spin is the consequence of parity violation. Without parity violation, this correlation would not exist because a parity transformation would flip the sign of the momentum vector but not the spin. As will be discussed in the next section, measuring the positron's energy, which is correlated to the parent muon's spin direction, provides a way of determining ω_a.

4.6 Anomalous Spin Precession Measurement

The anomalous spin precession frequency, ω_a, is the rate at which the spin is rotating relative to the momentum direction. Yet, in measuring this frequency, no angles are measured. Instead, we use the fact that the energy of the decay positron is directly related to the angle between the muon spin and muon momentum. As this angle changes with frequency ω_a, so does the energy of the decay positron with the same frequency. Assuming the muon beam is polarized at injection, the spin precession of all the muons

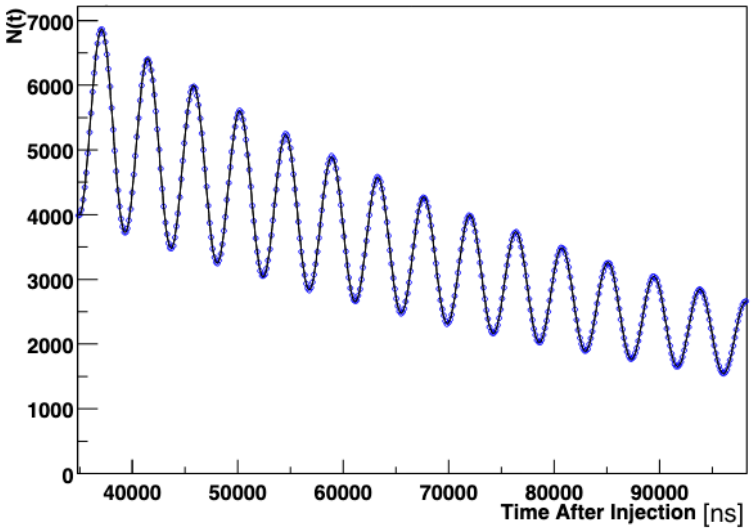


Figure 4.8: An example of the time histogram that results from counting positron energy clusters in the calorimeters over time. An obvious oscillation is visible in the signal, corresponding to ω_a. A fit (overlaid in black) is performed to extract the exact value of ω_a.

in the ensemble will coincide and will be reflected in a positron energy spectrum that oscillates with time. Generally speaking, this oscillation is observed by counting energy clusters identified as positrons from muon decay in the calorimeters and fitting the resulting time histogram. An example histogram can be seen in Fig. 4.8.

To understand exactly how this correlation manifests in the ω_a measurement, first consider the differential decay distribution. Assuming the decay positron energy is sufficiently large compared to its rest mass, the differntial decay distribution in the muon rest frame takes a form

$$\frac{d^2P}{dEdcos\alpha} = N(E)(1 + A(E)cos(\alpha)) \tag{4.21}$$

In particular, α is the angle between the muon spin and the positron momentum. The number distribution N(E) and the decay asymmetry A(E) are plotted in Fig 4.9. The asymmetry distribution expresses the strength of the correlation between muon spin and positron energy; a higher asymmetry signifies a stronger correlation.

Still, to get an equation which matches experimental observation, the muon decay distribution must be transformed into the lab frame. The lab frame energy of the positron has a strong dependence on its emission angle. As the emission angle is correlated with the muon spin direction, the energy distribution in the lab frame depends on the angle between the muon spin and the muon momentum. For example, when the muon spin and momentum are aligned, positrons are more likely to be emitted parallel to the muon momentum and are therefore more likely to be observed with higher energies in the lab frame. This results in an energy distribution in the lab frame of the form [33]

$$\frac{dP}{dE} = N(E)(1 + A(E)cos(\theta)) \tag{4.22}$$

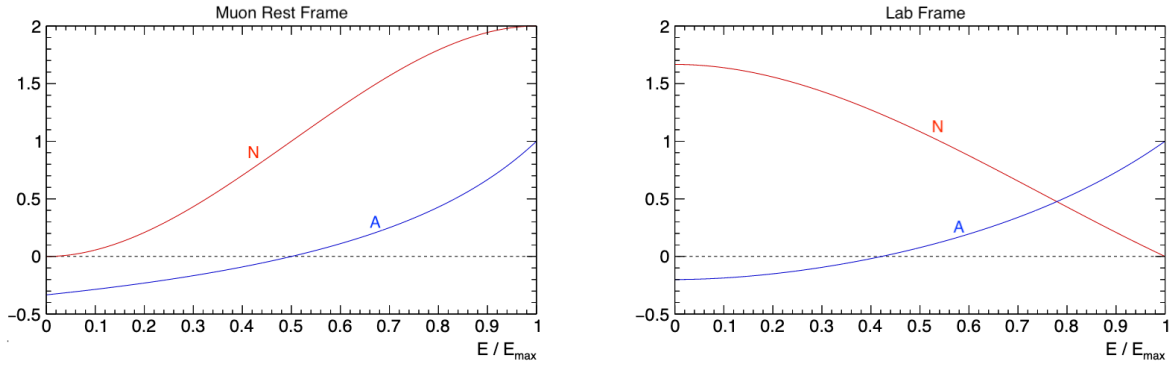


Figure 4.9: These plots show the dependence of number of decay electrons per unit energy, N, and the value of the asymmetry, A, as a function of electron energy. E_{max} in the muon's rest frame is 53 MeV and E_{max} in the lab frame is 3.1 GeV.

Here, θ is the angle between the muon spin and the muon momentum in the lab frame. The rate of change in θ is the anomalous spin precession frequency. As a result, the energy distribution in the lab frame has a period of $2\pi/\omega_a$. By replacing θ with $\omega_a t - \phi$, the result is a positron decay distribution from which ω_a can be extracted by measuring the period of the energy modulation. After making this substitution, the result is the following positron number distribution

$$N(t, E) = N_0(E)e^{-t/\tau}(1 + A(E)cos(\omega_a t + \phi)) \tag{4.23}$$

Fitting the time spectrum of the positrons in the calorimeter to this function is how ω_a is determined. Several additional effects must be taken into account to ensure an adequate fit; these effects will be discussed in Chapter 5.

Even though the correlation between positron energy and muon spin is the essence of the measurement, Muon $g-2$ is basically a counting experiment. Energy data is used to reconstruct positron events and to boost analyzing power, but the analysis can be done without it so long as a non-zero energy threshold is applied to the data. This works because the probability that a muon will decay to a high-energy positron depends on the angle between its spin and momentum, so the number of detected positrons over a non-zero energy threshold will oscillate at ω_a. Figure 4.10 illustrates the necessity of the energy threshold. Without an energy threshold, the anomalous spin precession signal would wash out as spectra in the lower energy bins interfere destructively with the spectra in the high energy bins.

Different weighting schemes take the positron energy into account, and this information is also crucial for understanding a variety of systematics. For the simplest weighting ($w = 1$), the statistical precison on ω_a is given by [34]

$$\frac{\sigma_{\omega_a}}{\omega_a} = \frac{\sqrt{2}}{\sqrt{N_p}A\gamma\tau_\mu\omega_a} \tag{4.24}$$

where N_p is the number of positrons in the histogram. The target statistical precision for E989 is 100 ppb. Reconfiguring Equation 4.24, we can determine the number of positrons needed to meet this goal, assuming A=0.37, τ_μ=2.2 μs, γ=29.3, and ω_a=1.44 MHz. With those values as input, 160 billion positrons are required.

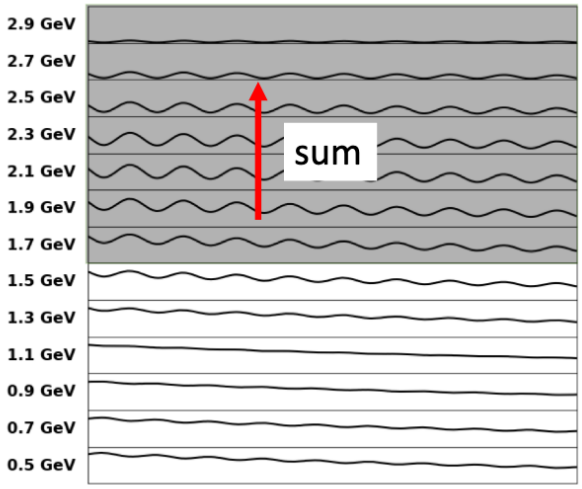


Figure 4.10: Calorimeter signals shown in various energy windows. The strength of the correlation between muon spin and positron energy is not uniform across all energies. Only positrons with an energy above a threshold that maximizes the correlation enter the histogram. Figure reproducded from Reference [29].

4.7 Magnetic Field Measurement

Creating a highly uniform magnetic field and measuring it precisely are crucial to the $g-2$ measurement. As shown in Chapter 1, the magnetic field directly impacts the muon spin precession frequency and the cyclotron frequency. Additionally, as shown in Section 4.4, the magnetic field influences the beam dynamics of the stored muons.

The ideal field is entirely vertical at 1.45 T but, within a finite space, this is not possible. In reality, higher-order multipoles, see Figure 4.11, perturb the dipole field. These additional contributions to the field create a storage region where not all muons see the same field, requiring a precision measurement not only as a function of azimuth but also as a function of radial and vertical position. For Run 1, the azimuthally averaged field nonuniformities were on the order of 1 ppm [35].

Pulsed nuclear magnetic resonance (NMR) is the technique used throughout the magnetic field measurement. As discussed in Chapter 1, a particle with a magnetic moment will precess about an external magnetic field. With an ensemble of precessing particles, a current will be induced that provides information about the external field. A radio frequency pulse rotates the net magnetization of a sample of protons relative to the external field. NMR harnesses the Larmor precession of protons by allowing the sample to precess about the external field until the magnetization returns to equilibrium by aligning with the external field. The precession of the protons will induce a current in coils within the probe. A Fourier transform of the signal provides ω_p.

The magnetic field is measured and monitored with proton NMR probes from three different subsystems. A trolley, carrying an array of NMR probes, drives around the ring, within the storage region, between fills when no muons are present. Additionally, 378 fixed NMR probes are embedded in the outer surface of the vacuum chambers, close to the storage region without being in the storage region. These probes can take measurements at all times, and specifically are meant to monitor and drifts in the field between trolley measurements. Finally, several absolute calibration probes are employed to correct for systematic effects in

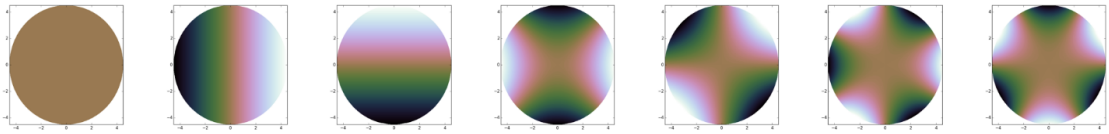


Figure 4.11: The first seven multipoles in the field expansion. Each multipole shows up as a possible symmetry of the field over the 2D azimuthal slice of the storage region. The magnetic field is thus characterized in terms of multipoles where the dipole should dominate and average to 1.45 T. Figure reproduced from Reference [36].

the trolley and fixed probe systems.

Field measurements from these different subsystems combine to produce a field map as a function of time and position, which provides ω_p. The average field experienced by the muons, $\bar{\omega_p}$, is the quantity that is actually required for a_μ, however. This quantity is determined by convoluting the field ω_p with the muon distribution, $M(\vec{r}, t)$. Data from straw tracking detectors is used to derived the muon distribution.

Chapter 5

Anomalous Spin Precession Measurement

This chapter will present an account of the anomalous spin precession measurement from positron dection through to the analysis and give an overview of the various systematic effects associated with the analysis. Chapter 8 will show the results of the analysis for several Run 2 data.

5.1 Positron Detection

This section is a review of the hardware and software components that collect and reconstruct the positron data.

5.1.1 Calorimeters

Evenly spaced around the inner radius of the storage ring are 24 electromagnetic calorimeters. Their purpose is to measure the arrival time and energy of positrons from muon decay. The calorimeter must have essentially 100% efficiency in resolving electromagnetic showers with a time separation of greater than 5 ns, and a greater than 66% success rate at providing spatial resolution. These requirements are intended to reduce systematics due to pileup, where two or more positrons enter a single crystal close together in time, leading them to be reconstructed as a single particle with energy equal to the sum of the energy from the two incident particles. In addition to the resolution requirements, the calorimeter gain must be stable over a 200 μs time period during the muon fill, a time frame which represents sufficiently many $g-2$ periods.

Each calorimeter is composed of a 9 by 6 array of $2.5 \times 2.5 \times 14\,\mathrm{cm}^3$ lead fluoride crystals, with each crystal wrapped in a single layer of black, non-reflective paper on the four long sides. Lead fluoride was chosen for having several desirable properties; it is a dense material with a high index of refraction and is transparent to optical light. Lead flouride's high index of refraction slows the propagation of light to a speed slower than the speed of charged particles in the material. This behavior results in an electromagnetic "sonic boom" known as Cherenkov radiation. The main advantage of building a calorimeter from a Cherenkov material is that Cherenkov radiation is fast. As opposed to a scintillating material, there is no delay between the production of Cherekov light and the movement of charged particles through the crystal. Given the 14 cm crystal lengths, the relevant time scale for Cherenkov light production is on the order of 1 ns. Allowing

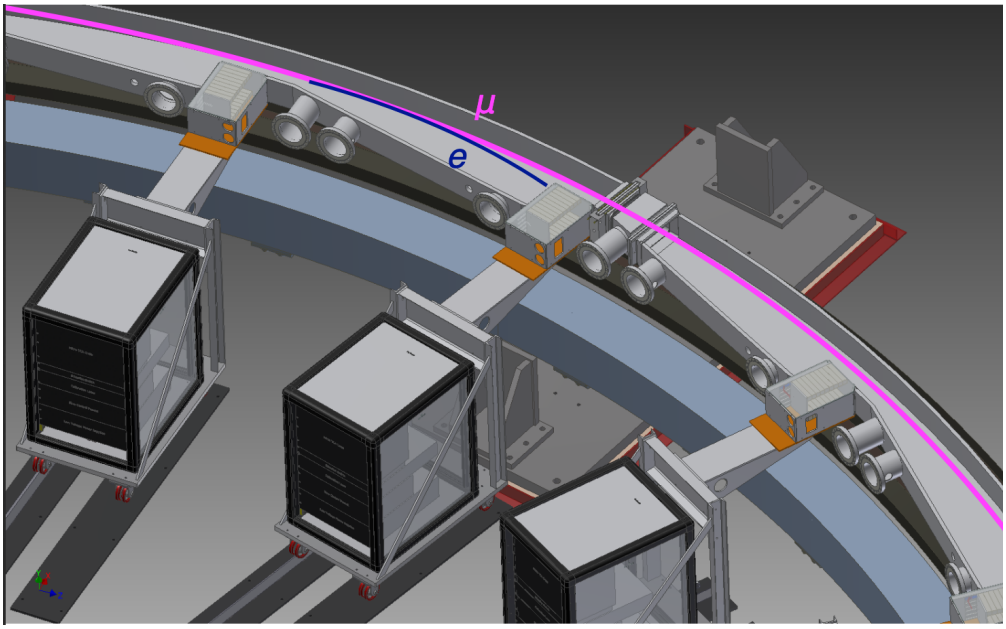


Figure 5.1: Model showing the position of the calorimeters relative to the vacuum chambers, courtesy of Jarek Kaspar. Calorimeters are mounted on carts that slide into place next to the ring.

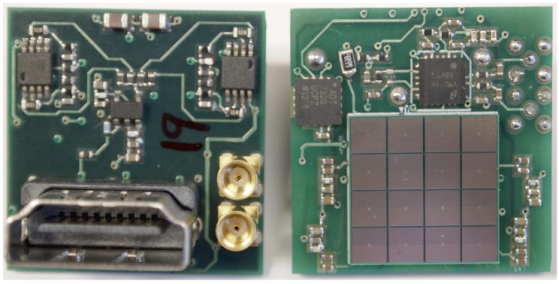


Figure 5.2: The photo on the right shows an early prototype of the 16-channel SiPM soldered on the amplifier board. Shown on the left is the other side of the board with HDMI connector and signal out connectors.[38]

for the possibility of photon reflections within a crystal before being detected, one should expect all the associated light to be collected within several nanoseconds of a positron impact. The short time between impact and detection results in a finer pulse time resolution and aids in reducing pileup pulses.

Each calorimeter fits into a scallop on a vacuum chamber, as in Figure 5.1. Given this limited space, it's advantageous to use a dense material in which positrons can deposit all their energy in a compact area. For lead flouride, 14 cm corresponds to approximately 15 radiation lengths. Additionally, the crystals have transverse dimensions larger than the lead flouride Moliere radius, leading to energy depositions from positrons that are typically contained almost entirely within one or two crystals [37]. This narrow cone of energy deposition from positrons also aids in reducing pileup. Even if pulses overlap in time, it is possible to spatially separate them due to the calorimeter segmentation.

5.1.2 Silicon Photomultipliers

Attached to the back face of each crystal is a $12 \times 12\,\mathrm{mm}^2$ monolithic 16-channel silicon photomultiplier (SiPM) with 3584 pixels per channel[39]. SIPMs are composed of an array of avalanche photodiodes which leverage the photoelectric effect to convert incident light to an electric current. SIPMs are sensitive enough to detect pulses as small as a single photon and as large as thousands of photons while also operating within regions of high magnetic field strength. Additionally, SiPMs are efficient at detecting photons near ultraviolent wavelengths, which is the relevant wavelength for Cherenkov radiation.

Most (74%) of the photons created by a positron's movement through the calorimeter crystals arrive at the SiPM within roughly 0.5 ns of each other. The remaining photons may undergo total internal reflection but still arrive at the SiPM within 10 ns of positron impact. As each photon strikes a pixel, it induces a characteristic electrical response. Recovery time for a pixel is about 10 ns. However, there are many more pixels than photons at any given moment so saturation effects are not observed.

5.1.3 Laser calibration system

The gain of the calorimeter system must be stable to within 0.1% over a muon fill, in order to reduce systematic uncertainty to the target level. Since SiPMs are temperature sensitive, the SiPM gains must be monitored and corrected over the course of the experiment such that calorimeter measurements are consistent across runs. To meet these requirements, a laser calibration system is employed which can provide laser pulses to all 1296 SiPMs in the ring. The intensity of the light sent to the SiPMs can be modified by using a collection of neutral density filters set to different known values. Additionally, the laser system provides a pulse at the beginning of every muon fill, called the sync pulse, that is used for timing alignment between channels.

To achieve the desired precision, detectors must be accurately calibrated and stable on both short and long time scales. Gain fluctuations must be suppressed at the sub ppm level over the course of a muon fill, in which the positron rate drops roughly four orders of magnitude. Gain is expected to be more stable over longer time scales, like those of a run (several months).

The laser calibration system begins with 6 lasers which each provide laser light to 4 calorimeters by a series of splitters and quartz fiber cables. The light is monitored first after leaving the laser by a Source Monitor (SM) and later by a Local Monitor (LM), once it arrives at its destination. There are several calibration routines meant to address different types of gain effects and time scales.

Short term double pulse (STDP) corrections are meant to address the phenomena of gain sag in a SiPM due to a preceding signal. That is, if two pulses occur close in time, the second pulse will suffer from the finite recovery time of the SiPM pixels. The laser calibration system fires two pulses at the same SiPM with 0 ns separation [40]. Dedicated studies extract the energy and temperature dependence of the STDP effect and provide the experiment with scaling factors to correct short-term gain drift.

The In-Fill gain correction equalizes gains within a muon fill. Pulses are deployed to calorimeter crystals as in the STDP protocol, but with pulse separation on the order of microseconds rather than nanoseconds. Local monitors are used to determine the gain function for the in-fill correction. In Run 1, it was discovered that the Source Monitors suffered from internal gain sag of about 0.2% at early times due to the sync pulse at the beginning of the fill. This effect has been mitigated in subsequent runs by adding 80 μs of time between the sync pulse and the first In-Fill laser pulse, giving the monitors time to recover.

The Out-of-Fill (OOF) gain correction mitigates temperature effects and equalizes different SiPMs in the

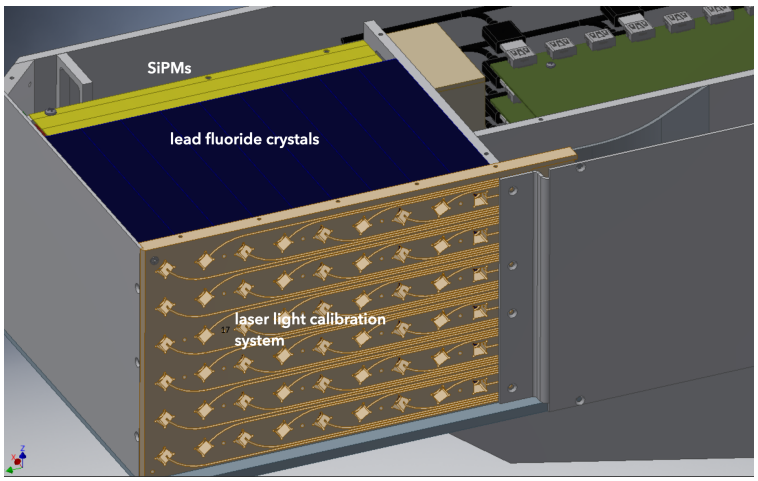


Figure 5.3: CAD model of a calorimeter in it's housing, illustrating the location of laser fibers and SIPMs on the front and back faces of all crystals, respectively. Courtesy of Jarek Kaspar.

same calorimeter. In Run 2C, the OOF correction ranged from 0.6-0.9 oscillating with daily temperature changes. Improved cooling of the hall is believed to be responsible for more stable OOF gains observed in Run 3.

5.1.4 Waveform Digitizers

Each SiPM converts the Cherenkov light created inside the crystal to an analog waveform. More specifically, it converts optical to electrical, generating an output that is voltage versus time, where the voltage is directly proportional to the number of photons. Those signals are then digitized in order for the data acquisition system (DAQ) to process them for online analysis and storage on disk for offline analysis. The read-out electronics have to meet the calorimeter resolution requirements for time and energy. The overall pile-up requirement for the experiment (separation down to 5 ns) requires a digitization sampling rate of at least 500 MSPS. Given that a higher digitization rate would ensure the requirement was always met and allow for better signal fidelity, a 800 MSPS sampling rate was chosen.

Each channel on a waveform digitizer has an ADC and its associated field programmable gate array (FPGA) to control the acquisition logic. The ADC chip consists of two interleaved ADCs operating at half the sampling rate with a common track and hold front-end that operates at the full sampling rate. Each channel has a 1 Gbit memory that can buffer 120 muon fills.

For each calorimeter, there is a corresponding electronics crate containing 12 waveform digitizers. Each waveform digitizer has 5 channels, such that a crate of 60 channels provides 1 channel per SiPM with a few channels left over. The waveform digitizer design complies with the Advanced Mezzanine Card (AMC) and micro-Telecommunications Computing Architecture (μTCA) standards. The design also includes a custom board called AMC13 which provides the primary experimental interface to the waveform digitizer. It supplies the 40 MHz master experimental clock, trigger and control signals via the CERN Timing, Trigger, and Control (TTC) protocol. It also provides parallel data transfer between the 12 waveform digitizers housed in the μTCA crate and the DAQ computer via a 10 Gbit/s optical link.

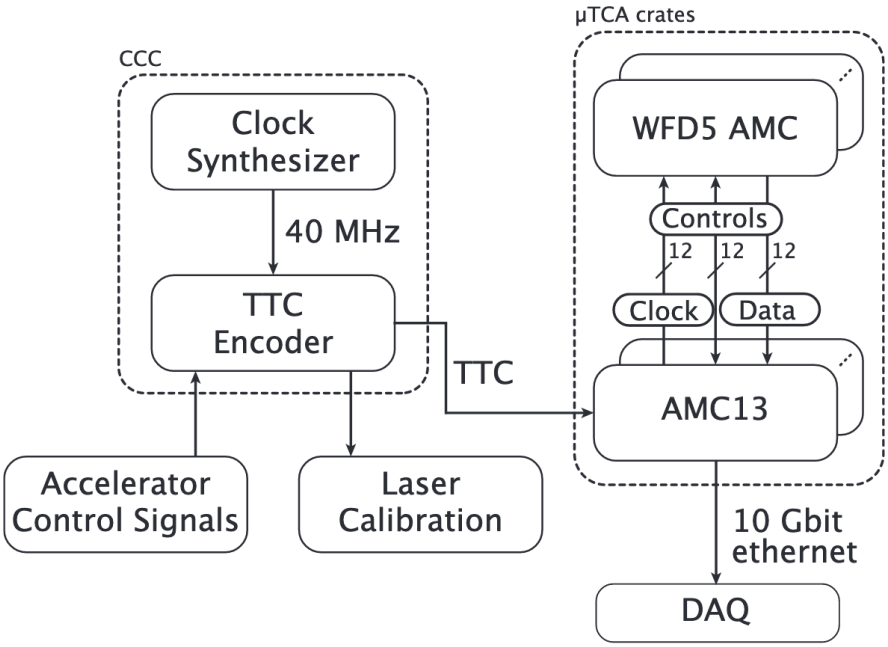


Figure 5.4: The interface between the Clock and Controls crate and a single μTCA calorimeter crate. In the experiment, there are 24 TTC connections between the CCC and each calorimeter crate. [39]

5.1.5 Clock and Calorimeter Backend Electronics

The Clock and Controls Center (CCC) takes the master 40 MHz clock and a beam-correlated signal as input and encodes both using the synchronous TTC protocol. The clock system upstream of the CCC provides two highly reliable clock signals to the experiment in the form of a 60 MHz signal used for the field measurement, and a blinded 40 MHz sine wave sent to the CCC for distribution to the calorimeter digitzers. The system is disciplined by Global Positioning System (GPS) timing received by two antennas, which are mounted to the roof of the experimental hall. These antennas transmit 1 pulse-per-second signals over two independent cables to two separate receivers in the computer room. One antenna and receiver is used to drive the primary clock, and the other antenna is used to drive the monitoring clock. Both clocks contain internal rubidium oscillators, which ensure short-period stability, while the GPS signal ensures long-period stability. Both the primary and monitoring clocks provide 10 MHz output signals.

The primary 10 MHz clock signal is used as a timebase for generating the two previously mentioned clock signals for the field and precession frequency measurements. In addition, the primary 10 MHz clock is used to generate a third clock frequency, a blinded 30 MHz frequency used only for monitoring purposes. The 40 MHz and 30 MHz clocks are mixed and filtered to provide a monitoring signal at about 10 MHz that has direct sensitivity to changes in the 40 MHz frequency without revealing its value [41].

Clock Blinding

In an experiment where a particular outcome carries so much significance, such as E989, analyzers must be careful not to let conscious or unconscious bias impact their analyses. One way of addressing bias is by making it impossible for analyzers to know the exact actual value they are extracting by shifting, or blinding,

some input by a tiny amount. Since we are extracting a frequency in E989, the blinded quantity is time.

Blinding occurs at two separate levels in the ω_a measurement–first at the hardware level and then at the software level. Hardware level blinding is implemented in the clock system by adjusting the master 40 MHz clock signal to include a small offset within ± 25 ppm. The exact value of the shift is known only by two FNAL personnel who are not otherwise involved with the g-2 experiment. The secret clock frequency is only corrected once all the collaboration has reached a consensus among all ω_a analyses. For Run 1 data, unblinding occured after months of verification and consistency checks between different analyses groups and the unblinded results was published shortly thereafter. For subsequent runs, the hardware blinding will be reset to a new shift.

The second type of blinding occurs at the analysis level and will be discussed in chapter 7.

5.1.6 Data Acquisition

The data acquisition system (DAQ) has been designed to utilize Graphical Processing Units (GPUs) to extract the necessary decay positron information from digitized muon fills. The design consists of 26 GPUs housed by pairs in 13 front-end computers. Each front-end computer processes data from two calorimeters, with a dedicated GPU for each of the calorimeters.

Muons fills are injected into the storage ring at an average rate of 11.4 Hz, with each 700 μs fill separated by 10 ms. During each fill, approximately 16,000 muons are stored. Resulting decay positrons are detected by calorimeter, as described above, and the full 700 μs waveform is stored for each of the 1296 calorimeter channels. For this fill configuration, the DAQ must handle a time-averaged rate of raw ADC samples of 18.6 GB/s [42].

The DAQ is constructed using a layered array of commodity, networked processors. The frontend layer reads out data from the digitizers, unpacks and processes the data, and sends it to the backend layers that are used for assembly of event fragments and writing the data files to disk. A slow control layer is used for the setting and monitoring of high voltages, temperatures, and other slowly varying parameters. An online diagnostic analysis layer monitors the integrity of raw data by reconstructing and analyzing small samples of the raw data in real time, which is distinct from the full offline analysis that uses stored-to-disk data. The DAQ software is based on the MIDAS data acquisition software developed at PSI and TRIUMF. Thus, data is written to disk as MIDAS files, which are later converted to a human readable format.

The GPU kernel functions are designed to perform two different algorithms on each waveform, which produce two independent output streams to be analyzed for measurements of the precession frequency. The two algorithms are called the T-method and Q-method. For the T-method, positron events in each calorimeter are individually identified during the reconstruction process in order to obtain a spectrum of time and energy. This requires the DAQ to enforce an energy threshold for all pulses, then add a set number of postsamples and presamples to each pulse and combine any overlapping pulses to form single larger islands. An array of island data is then passed out of the GPU and back to the computer memory. All events above the threshold are included, and the anomalous precession frequency is determined from a fit to a histogram, as explained in Section 4.6. This was the analysis method used in the Brookhaven experiment and is the method that forms the basis of the the analysis presented in this thesis. The Q-method, on the other hand, does not identify individual positron events, but instead integrates the detector current as a proxy for the event energy. In practice this is performed by histogramming the full pedestal-subtracted waveforms on a fill-by-fill basis, and fitting that sum to extract the frequency.

5.2 Data Reconstruction

Before any analysis can be done, raw calorimeter output must be transformed into data that represents the time and energy of incident positrons. The algorithm by which the positron's physical quantities are extracted from the waveform digitizers' traces is known as reconstruction. The E989 collaboration has created two distinct reconstruction paths that take waveforms to positron events, known colloquially as ReconWest and ReconEast. Both reconstruction approaches use the T-Method as their foundation. That is, both paths aim to reconstruct individual positron events in the calorimeter from the ADC traces. The analysis here uses ReconEast data.

Both approaches follow the same general principles. Electromagnetic showers result in a characteristic pulse shape for each crystal-SiPM pair in the ring, linearly scaling with the incident positron's energy. This key feature allows for each SiPM's pulse to be modeled by a template pulse shape that scales in amplitude and translates in time. As a result, a reconstruction can be built around fitting each recorded pulse to its SiPM's template along with a constant pedestal. The peak of the resulting fitted pulse correspond to the reconstructed time of the positron event and the amplitude of the fitted pulse gives the energy deposition. Templates are created by collecting a large number of pulses for each crystal, then normalizing and aligning these pulses to create a characteristic pulse shape. This process is discussed in more detail in Chapter 6. Both reconstruction algorithms use the same pulse templates. In the ReconWest approach, traces from each crystal are fit separately, without taking into account any nearby activity. On the other hand, ReconEast takes a global approach, fitting multiple traces simultaneously. An overview of the algorithm is given in the following paragraph, but extensive details can be found in Reference [43].

As stated previously, ReconEast uses a global approach to fitting. Template amplitudes and peak times are coupled together based on a model of the electromagnetic shower, which depends on the positron's impact position and impact angle. An event processed by the reconstruction consists of an island per crystal in a calorimeter. Islands are signal traces delivered by the DAQ that result from chopping the continuous output of the waveform digitizers in reasonable pieces. When there is a signal in any of the crystals in a calorimeter, an island is created from the traces of all the crystals in the calorimeter at the time of the signal, with the addition of some pre- and post-samples. The ReconEast algorithm approaches each island with the initial hypothesis of only one positron showered in the calorimeter. Initial estimates are made for all fit parameters–pedestal for each crystal, positron impact position, positron impact angle, positron energy, and time of impact. A χ^2 minimization fit finds optimal parameters under the one positron hypothesis. Fit residuals are then analyzed for all traces in the island to determine if another positron should be added to the hypothesis. After this fitting process is completed for all islands in the fill, the final step is to refine the results by fitting them all together. The motivation for this step, sometimes referred to as a chain fit, is to mitigate the effects of island chopping on the pulse fits. For example, supposing that the tail of a pulse on one island extends into the subsequent island, the fit would be improved by considering both islands together.

5.3 Analysis Methods

In order to attain a value for the anomalous magnetic moment of the muon, E989 must measure two different quantities, ω_a and ω_p. Information about the magnetic field experienced by the beam of muons is contained in ω_p, while ω_a measures the rate at which the spin of muons in a storage ring precess about their momentum.

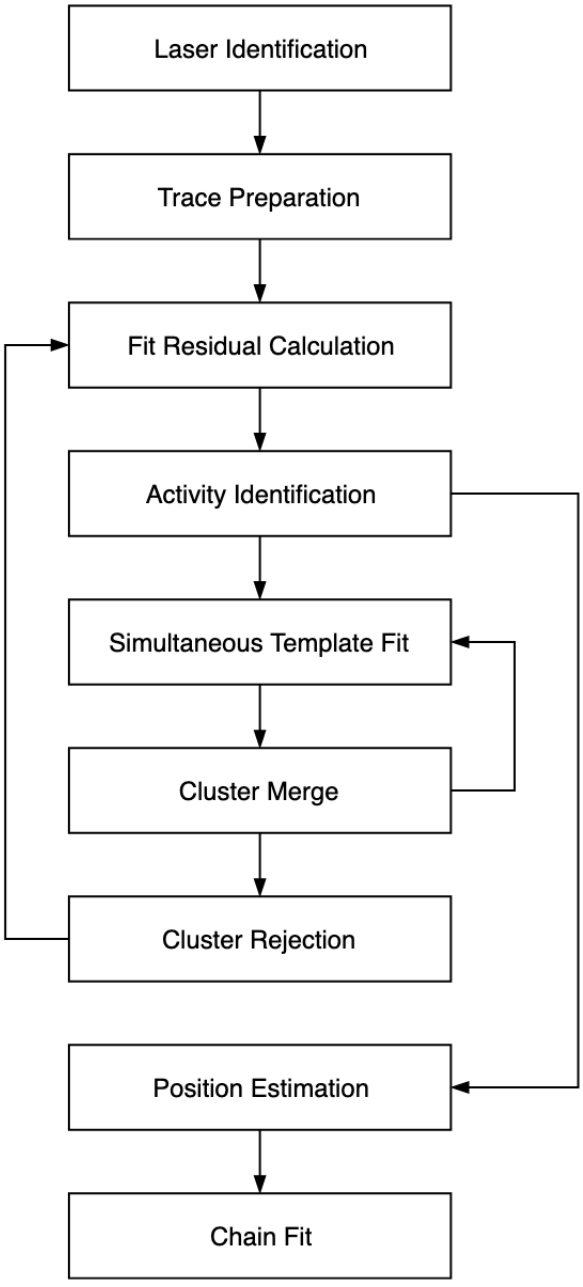


Figure 5.5: A flow diagram of the key steps in the ReconEast pulse fitting algorithm. The main part of the algorithm is the loop between Fit Residual Calculation and Cluster Rejection where clusters in the island are identified and fit one-by-one in approximately decreasing energy. Figure reproduced from Reference [43].

As previously mentioned, this thesis is concerned with a measurement of ω_a.

There are several ways of extracting ω_a and each method uses time and energy information to find the rate at which the spin precesses about the muon momentum. Provided here is a brief overview of the main methods used by analyzers in E989:

- T-Method: This method was used in E821 and continues to be the primary method for E989, due to its conceptual simplicity. A T-Method analysis requires positron events in the calorimeter to be individually identified, sorted and fit to obtain time and energy. An events vs. time-in-fill histogram is built from all events with reconstructed energy above a threshold. In the simplest version of the T-Method, all events in the histogram are given equal weight ($w = 1$). Then ω_a is obtained from fitting the histogram to the correct model function, based on Equation 4.21.

- Energy-weighted T-method: This method is identical to the T-Method with the exception of the weighting scheme. Events are weighted by their energy. This has the effect of increasing the statistical power of the data, since higher energy positrons imply a stronger correlation between momentum and spin direction of the parent muon.

- Asymmetry-weighed T-method: This method is identical to the T-Method with the exception of the weighting scheme. Events are weighted by their asymmetry which is a function of energy. Similar to the energy-weighted method, the asymmetry-weighted method harnesses the relationship between energy and polarization to increase the statistical power of the data. In the absence of detector effects, this method results in the smallest uncertainty on ω_a.

- Ratio Method: The Ratio Method creates a linear combination of T-Method histograms in order to eliminate the muon lifetime component of the distribution (see Equation 4.21), so that what remains is a simple cosine. The advantage of this method is that it essentially divides out time-sensitive effects, so systematic effects such as pileup and gain instability have less impact on the fit results.

- Q-Method: The Q-Method approaches ω_a extraction differently than the other methods which are all based on the same paradigm of counting positron events over a threshold. In the Q-Method, there is no threshold, and the analysis uses raw data rather than reconstructed pulses. As a result, systematic effects are manifested and treated quite differently. The main advantage of the Q-Method is a reduced susceptibility to pileup errors and the main disadvantage is a loss of statistical power.

None of these techniques are radically better than the others. Some optimize statistical precision, while others provide reduced sensitivity to bothersome systematic effects. Using a variety of complementary methods to analyze the data gives the collaboration more confidence in the measurement. It is also worth mentioning that one may attempt to analyze the data in a way that replicates the statistics and systematics of the E821 data set, in order to make some comparisons between the two experiments which are meant to operate on identical principles but with E989 having increased resolution and suppression of several systematic errors. Specifically, carrying out a "E821-style" analysis on E989 data would consist of reducing the time and spatial resolution of the calorimeter data, as well as increasing the energy threshold on clusters which enter the histogram.

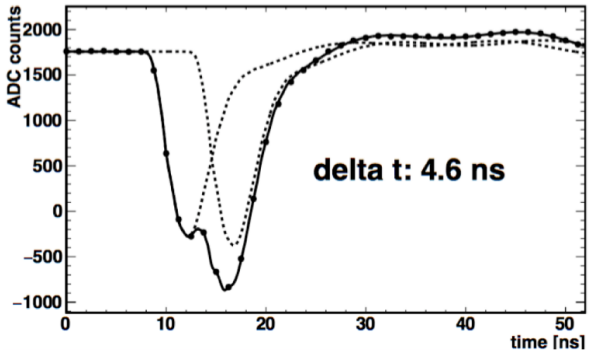


Figure 5.6: An example of pileup in a prototype calorimeter during an early test beam experiment [44]. Two pulses close in time (separated by 4.6 ns) are reconstructed as a single pulse with incorrect amplitude and hit time. The solid line shows the fit result while the dotted lines show the actual pulses which were mistakenly reconstructed as one.

5.4 Systematic Effects

There are two general classes of systematics in the ω_a measurement. The first category contains effects related to detector performance and the second category contains effects caused by beam dynamics. Specifically, pileup and gain effects come from the calorimeter, while muon losses and betatron oscillations result from the particular beam motion in the ring. The rest of this chapter will cover the main systematic effects which are important to consider in any ω_a analysis. Detailed descriptions of how the associated uncertainties are calculated for this analysis will be provided in Chapter 8.

5.4.1 Pileup

Pileup occurs when two or more positrons hit the calorimeter close enough in space and time such that they cannot be resolved as individual positron hits. An example is shown in Figure 5.6, where two pulses with similar amplitude are assigned a higher amplitude and a peak time that does not correspond to either of the constituent pulses. For the reconstruction algorithm used in this analysis, the time separation below which pulses can no longer be resolved at 100% efficiency is 3 ns. Pileup is an inevitable consequence of this inability to resolve all pulses separated by minuscule amounts of time. As a result, a subset of the data contains incorrectly reconstructed clusters with the wrong energy and time. Of course, the better the pulse separation of the reconstruction algorithm, the less pileup will be present in the data. Pileup is much less of a problem in E989 than E821, as pulse separation has improved with increased timing and spatial resolution. The most obvious signature of pileup in the data can been seen in the energy distribution, as shown in Figure 5.7. As it is impossible for a muon beam with average energy 3.1 GeV to produce decay positrons with energy greater than 3.1 GeV, so those events above 3.1 GeV must come from clusters that combine energy depositions from several positrons. Technically, a signal above 3.1 GeV can also come from noise but the calorimeter and electronics in E989 exhibit minimal noise. The rate of double pileup, referring to pileup between two positrons, is highest, while the rate of triple pileup is much lower. Higher orders of pileup are in principle possible but rarely observed. Other configurations can produce pileup, such as a positron plus a lost muon, or a positron plus electromagnetic shower leakage from another calorimeter. These types of events are less common and generally negligible. For the sake of simplicity, from this point forward, *pileup*

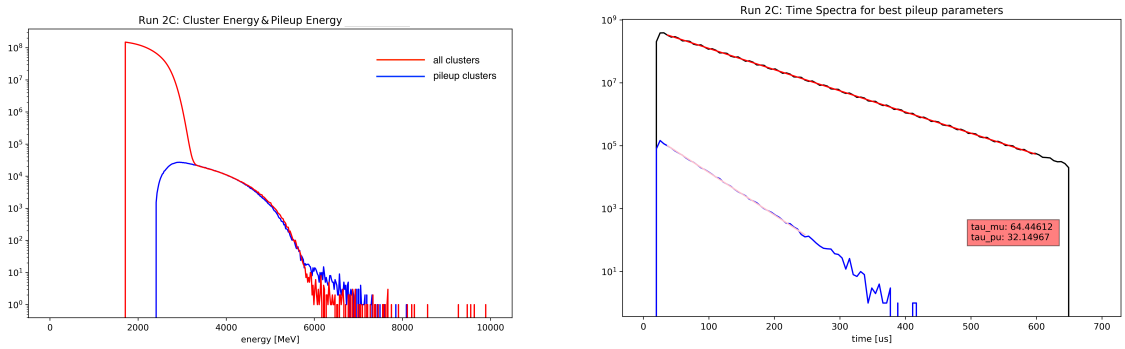


Figure 5.7: On the left, the energy distributions for all reconstructed clusters (red) and pileup clusters (blue). On the right, the time distributions for all clusters (black) and pileup clusters (blue). The time histograms are rebinned to remove any oscillations so an easy exponential fit can be performed to show the different lifetimes of the two distributions.

will be used to refer to pileup from two positrons only.

The rate of pileup is proportional to the square of the overall hit rate. These distortions in the time and energy spectra could easily be accounted for if they were constant throughout the fill. However, the time-dependence of pileup introduces a term into the time spectrum that decays with half the muon lifetime, preventing a precise fit to the fit function which decays with the muon lifetime. Further, pileup events have a different phase than non-pileup events. Consider the difference in time-of-flight between high and low energy decay positrons. High energy positrons have a less curved trajectory as they fall out of orbit compared to low energy positrons. As a consequence, high energy positrons generally will spend more time traveling to the calorimeter. This longer time-of-flight corresponds to a different phase between high and low energy positrons. As such, the pileup rate has its own phase ϕ_{pu} strongly correlated to ω_a and the nominal phase ϕ_0. If pileup is not removed from the data, this effect causes it to directly bias the extraction of ω_a.

A reduction in pileup can be achieved by designing a detector with as low a dead time as possible. For the E989 calorimeter system, the dead time is less than 5 ns. However, increased beam injection and storage results in a higher positron rate at the calorimeter which will increase the pileup rate. The E989 pileup error budget is 40 ppb.

In the absence of a detector with a dead time of zero, pileup must be accounted for some other way. The general technique consists of constructing a replica of the pileup distribution from the data and then subtracting it from the data before fitting. There are several ways of constructing pileup, though the method used in this analysis is called the "shadow method." The shadow method is concerned with double pileup only and assumes that the probability that a positron event has an underlying pileup event is equivalent to the probability of finding an event in the external time window. This motivates the decision to look for pulses close to each other as a proxy for pileup. More precisely, for each pulse (E_1, t_1) within an island, we look in a time window some time offset from that pulse for another pulse (E_2, t_2). The time window is called the shadow window and the time offset from the first pulse is the gap time. For each shadow pulse that is found, the energy and times of the initial pulse and the shadow pulse are entered into the doublet spectrum, subject to the following relations,

$$\begin{aligned} E_D &= C(E_1 + E_2) \\ t_D &= t_1 + \frac{t_G}{2} \end{aligned} \tag{5.1}$$

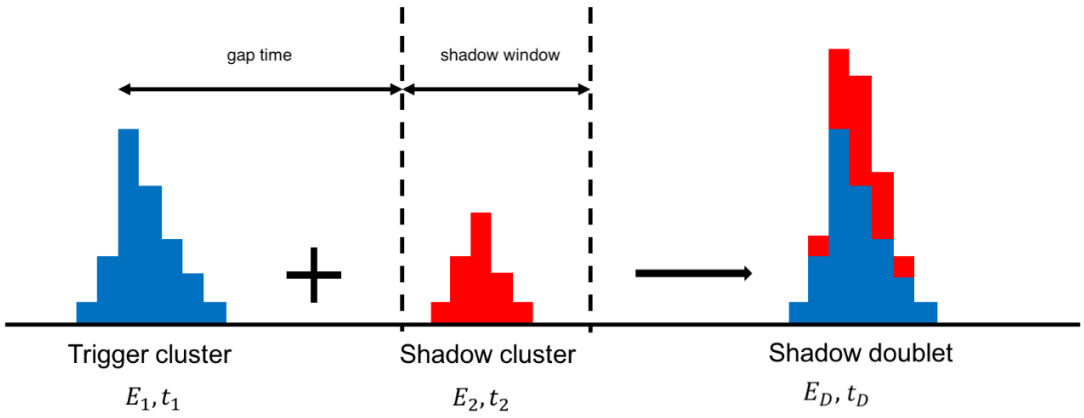


Figure 5.8: Illustration of the shadow method. A doublet is constructed from a trigger singlet and a shadow singlet. The gaptime and shadow window width are optimized to match the pileup distribution observed in data.

where t_G is the gaptime, E_D is the energy of the doublet, t_D is the time of the doublet, and C is a calibration constant. If the shadow window is too large, too much pileup with be constructed. A good estimate for the size of the shadow window is the dead time of the pulse fitter, though a scan over shadow windows of different sizes should be done to find the shadow window that optimizes the pileup construction. After looking at all the pulses in a fill, the final pileup spectrum is created by subtracting the singlet spectra $S_1 + S_2$ from the doublet spectrum D.

$$PU = D - S_1 - S_2$$

In this way, only the pileup remains and the individual singlets that constitute the doublet spectrum are not counted twice in the pileup distribution.

5.4.2 Gain Changes

Gain refers to the conversion between the physical energy deposited in a detector and the output signal. In the calorimeters of E989, Cherenkov photons are converted to MeV with the help of the laser calibration system. Ideally, gain is a fixed factor that depends only on the hardware configuration. However, gain can drift as a result of external influences. Temperature and hit rate are the main causes of gain changes in E989. Temperature effects occur over long time scales while hit rate changes rapidly over the course of a single fill. This fast gain change can cause a systematic bias in the ω_a extraction.

Gain changes on the order of a fill can effectively change the energy threshold over the course of a fill. A time-dependent energy threshold results in time-dependent asymmetry, phase, and amplitude. Just like with pileup, a phase shift will bias the observed precession frequency and the fit function will return incorrect values for the various parameters. The E989 uncertainty budget for changing detector gains is 20 ppb.

Gain is monitored and corrected mainly through the use of the laser calibration system, described in Section 5.1, which fires laser light into each crystal in every calorimeter crystal before and during each fill. The laser gain correction scheme operates at three time scales, short-term, in-fill, and out-of-fill. The function describing the relationship between laser energy and measured laser pulse energy is given

by $E = E_0(1 - ae^{-t/\tau_g})$ where E is the measured energy, E_0 is the laser energy, and a and τ_g are constants determined by the laser calibration system [45]. Corrections to positron data then use this relation between deposited and measured energy as the gain correction. This correction is applied to the crystals at the reconstruction level of data production.

5.4.3 Muon Losses

For many reasons, it is inevitable that muons will fall out of the storage ring before they decay–these muons are referred to as lost muons. For example, nonuniformities in the magnetic field can result in betatron oscillations which swing the beam horizontally leading muons to leave the storage region, collide with an object, and scatter out of the beam.

As the ω_a measurement depends on the assumption that all injected muons have the same polarization, it is imperative to determine the degree to which muon losses result in a time dependence of the stored muon's phase. For example, muons that tend to be lost might be those muons produced before pion momentum selection, or muons produced along the injection beamline. In either case, these muons would have a different polarization than muons produced along the M2 and M3 beam lines. If these muons have a higher loss probability than the rest, the different phase will bias the average phase as these muons leave the storage ring, creating a time-dependent phase. This is related to an effect called differential decay, which will be discussed at the end of this chapter. The extent to which lost muons have a different phase than other muons is the subject of extensive beamline simulations and study [46]. Another effect which pertains to the ω_a analysis is the distortion of signals in the calorimeter from lost muons. Unlike the potential phase effect, this does not bias ω_a, though it does make fitting the time histograms more difficult.

In order to account for these distortions, the fit function is modified to reflect the decrease in counts from muons that leave the ring before decaying. A lost muon spectrum is constructed by looking for clusters in the calorimeter data with several key characteristics that distinguish them from positron clusters. First, muons are minimum ionizing particles (MIPs), so we look for energy clusters between 50-200 MeV. Second, lost muons should strike multiple calorimeters in sequence as a result of their MIP nature. With a known time of flight between calos of approximately 6 ns, we can look for coincidences between two or three calos. By counting these occurrences, we get a muon loss rate as a function of time that can be subtracted from the positron time spectrum. Of course, not all lost muons will be detected in the calorimeters but this procedure provides a rate that can be multiplied by a proportionality constant related to the detection efficiency, which is left to float in the fit.

5.4.4 Coherent Betatron Oscillations

The muon beam undergoes coherent betatron oscillation (CBO), as described in Section 4.4, which causes the beam to vary its radial position as it travels around the ring. Detector acceptance depends on the radial coordinate of the muon when it decays. As the beam shifts out, less high energy positrons hit the end of calorimeter, resulting in a lower rate. As the beam swings towards the calorimeter, more high energy positrons hit the calorimeter, resulting in a higher rate. Thus, coherent radial motion of the stored beam can produce an amplitude modulation in the observed positron time spectrum. It is most easily observed in the residuals of the standard 5-parameter fit function (Equation 4.23).

As the beam spreads in the storage ring, the betatron oscillations lose their coherence with a lifetime that is on the order of 90-130 μs. Analysis methods, such as the Ratio Method, which are less sensitive to

time-dependent effects are less impacted by CBO. It is also possible to remove a substantial amount of CBO from the data simply by adding together the data from all calorimeters though some amount of CBO will still remain. For this reason, analyzers generally add terms to their fit function that model the CBO. Straw tracking detectors, which observe the beam motion, are useful for corroborating the CBO model used in the ω_a fit. This addresses the asymmetry and phase modulation and results in a better fit.

The same considerations hold for vertical betatron oscillations, which decay away faster and have a smaller amplitude than horizontal betatron oscillations.

5.4.5 Pitch and Electric Field Corrections

In an ideal case, wherein the muon momentum is perpendicular to the magnetic field and the electric field is zero, we have an expression for ω_a that looks like

$$\omega_a = \frac{e}{m} a_\mu B \tag{5.2}$$

However, despite our best efforts to keep the muon beam centered and perpendicular to the magnetic field, what occurs in the experiment is not the ideal case. Due to betatron oscillations, quadrupole plate misalignments, and the momentum spread of the beam, the equation for ω_a actually takes the following form [27]:

$$\omega_a = \frac{e}{m}[a_\mu B - a_\mu \frac{\gamma}{\gamma+1}(\beta \cdot B)\beta - (a_\mu - \frac{1}{\gamma^2-1})\frac{\beta \times E}{c}] \tag{5.3}$$

Here we see that if the momentum was perpendicular to the magnetic field, the term $(\beta \cdot B)$ would vanish and if the electric field experienced by the muons is zero then the term $(\beta \times E)$ would vanish. Another way to get rid of this term involves setting γ such that $(a_\mu - \frac{1}{\gamma^2-1})$ goes to zero. Conveniently, the value for $\gamma = 29.3$ needed to do this is physically accessible and defines the momentum we use for the experiment, $p = 3.094$ GeV/C, known as the magic momentum. However, the beam has a nonzero momentum width, meaning this term does not cancel for every muon in the beam.

The case in which $(\beta \cdot B) \neq 0$ requires a correction referred to as the pitch correction because the pitch angle of the muon varies due to vertical betatron motion. The case in which the electric field term does not go to zero because of the muon momentum spread requires a correction referred to as the electric field correction. The combined E989 error budget for the electric field and pitch corrections is 30 ppb. We will consider each correction separately first, before considering how they combine. The derivations of the pitch and electric field corrections that follow assume ideal $\vec{E}$ and $\vec{B}$ fields, as given in Equations 4.5 and 4.6.

Suppose all muons are injected at the magic momentum but perturbations in the vertical angle are allowed to occur. This will allow the $(\beta \times E)$ term in equation 7.2 to vanish but vertical betatron oscillations will result in $(\beta \cdot B) \neq 0$. The expression for ω_a becomes

$$\omega_a = \frac{e}{m}[a_\mu B - a_\mu \frac{\gamma}{\gamma+1}(\beta \cdot B)\beta] \tag{5.4}$$

Muons in the storage ring will pitch up and down as they go around in azimuth with pitch angle given by

$$\psi = \psi_0 cos(\omega_y t) \tag{5.5}$$

where ψ_0 is the oscillation amplitude and ω_y is the vertical betatron frequency. When the pitch angle is

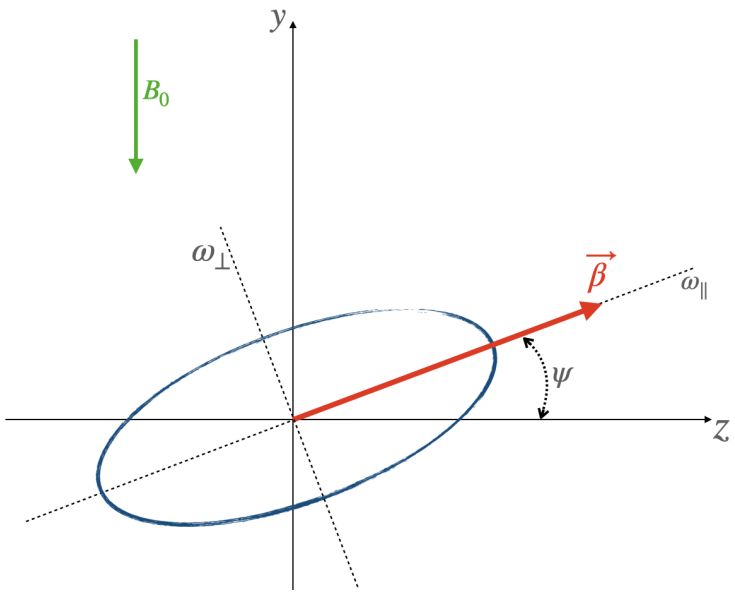


Figure 5.9: Due to vertical betatron oscillations the pitch angle ψ between β and the z-axis varies. The spin angle is determined in the plane indicated by the blue oval and the dashed lines represent the parallel and perpendicular motions of the beam.

non-zero, $\vec{\beta}$ now has two components, one parallel to the magnetic field (y-direction) and one perpendicular to the magnetic field (z-direction). In terms of the pitch angle, $\vec{\beta}$ becomes

$$\vec{\beta} = \beta_y \hat{y} + \beta_z \hat{z} = \beta cos(\psi)\hat{y} + \beta sin(\psi)\hat{z} \tag{5.6}$$

Using the small-angle approximations $cos\psi \approx 1$ and $sin\psi \approx \psi$, $\vec{\beta}$ reduces to

$$\vec{\beta} = \beta\hat{y} + \beta\psi\hat{z} \tag{5.7}$$

Plugging this into Equation 5.4, and assuming a purely vertical field, $\vec{B} = B_0\hat{y}$, we get expressions for vertical and azimuthal components of ω_a

$$\omega_{a,y} = \omega_a[1 - \frac{\gamma - 1}{\gamma}\psi^2] \tag{5.8}$$

$$\omega_{a,z} = \omega_a[\frac{\gamma - 1}{\gamma}\psi] \tag{5.9}$$

Since the direction of ω_a is defined by the direction of β this causes the direction of ω_a to oscillate at the pitch frequency. The relevant component of the precession frequency is the component perpendicular to the momentum since this component carries information about the angle between the muon momentum and muon spin. The pitch frequency is more than an order of magnitude greater than ω_a, so the effect of parallel ω_a components on the observed precession frequency can be expected to average out to zero [47]. Therefore it is fair to approximate the observed precession frequency as the perpendicular component, shown in Equation 5.10. This perpendicular component can be determined with the help of the small-angle

approximations $cos\psi \approx 1 - \frac{\psi^2}{2}$ and $sin\psi \approx \psi$

$$\omega_{a\perp} = \omega_{a,y}cos(\psi) - \omega_{a,z}sin(\psi) \approx a_\mu \frac{eB_0}{m}(1 - \frac{\psi^2}{2}) \tag{5.10}$$

Averaging over the muon ensemble and again using small-angle approximations (the pitch angle is on the order of milliradians), the pitch correction can be shown to be

$$C_p = \frac{\Delta\omega_a}{\omega_a} = -\frac{<\psi^2>}{2} \tag{5.11}$$

The pitch angles cannot be measured in the ring but they can be written in terms of the vertical betatron amplitudes. Using the relation $\psi \approx v_y/\omega_c R_0$, the pitch correction is expressed in terms of vertical position, v_y, which can be directly measured with the straw tracker system.

Now suppose all muons are injected with no pitch angle, i.e. perpendicular to the magnetic field. Then $\vec{\beta} \cdot \vec{B} = 0$. Also suppose the muon momentum diverges a bit from the magic momentum. Then in Equation 5.3 the second term will vanish but the $\vec{\beta} \times \vec{E}$ term will remain. With β completely along the azimuthal direction, the only non-zero terms from $\vec{\beta} \times \vec{E}$ are $B_z E_r$ in the vertical direction and $B_z E_y$ in the radial direction. The leading term in the expression for ω_a is in the vertical direction (due to the purely vertical B-field). Since $B_z E_r$ is parallel to the leading term in ω_a , it is the dominant component and $B_z E_y$ can be considered negligible. The expression for ω_a then becomes

$$\omega_a = -a_\mu \frac{eB_0}{m}[1 - \beta\frac{E_r}{cB_0}(1 - \frac{1}{a_\mu\beta^2\gamma^2})] \tag{5.12}$$

It is appropriate to expand γ about the magic momentum p_m and treat β as unchanging over this range of γ. Then, using $p = p_m + \Delta p$, the fractional difference in ω_a is

$$C_E = \frac{\Delta\omega_a}{\omega_a} = -2\frac{\beta E_r}{cB_0}\frac{\Delta p}{p_m} \tag{5.13}$$

The effect of the radial electric field reduces the observed frequency of ω_a. When averaged over a spin precession period, the electric field correction can also be written in terms of equilibrium radius x_{eq} with respect to the center of the quadrupole potential R_0 [29].

$$\frac{\Delta\omega_a}{\omega_a} = \frac{-2\beta^2 n(1-n)}{R_0} < x_{eq}^2 > \tag{5.14}$$

Calorimeter data can be used to determine $< x_{eq}^2 >$, leading to a measurement for the electric field correction.

Equations 5.11 and 5.13 show that the radial electric field and the vertical pitching motion lower the observed precession frequency from the ideal case $\omega_a = (e/m)a_\mu B$. Therefore these corrections should increase the observed frequency in order to obtain an unbiased measurement of the anomaly.

5.4.6 Fast Rotation

Fast rotation refers to the cyclotron motion in the ring, which has a revolution frequency of 6.706 MHz for muons propagating at the ideal radius with the magic momentum. Muons initially enter the ring with a temporal width of about 120ns, but as the beam evolves in time, its momentum spread makes it debunch and approach uniformity in azimuth. As a reminder, muons with different momenta will orbit at different

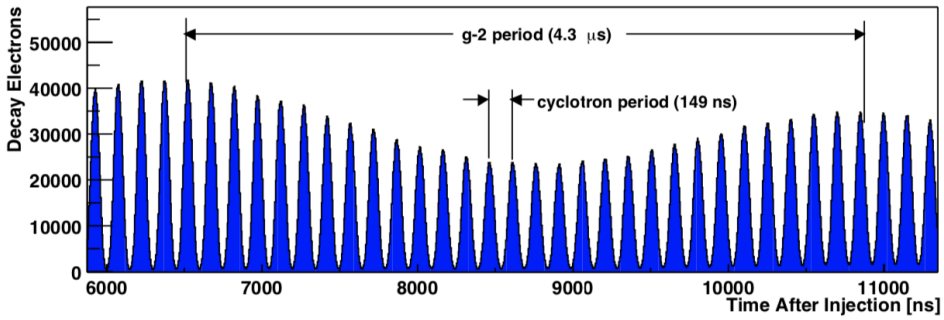


Figure 5.10: If the binning is too fine, calorimeter data will oscillate at the cyclotron frequency under the $g-2$ frequency until the beam debunches. Figure reproduced from Reference [2]

.

radii (see Equation 4.15), while traveling at the same speed. Muons at higer radii will take a longer time to get around the ring and fall behind the muons at lower radii. Beam debunching typically takes 2400 turns to complete [48].

The presence of the fast rotation signal in the data does not bias ω_a but it does add a frequency to the data which complicates extraction of ω_a. The simplest solution is to bin out the fast rotation by binning the positron time spectra in periods of the cyclotron frequency. Each hit time is also randomized by $\pm T_c/2$, where T_c is the cyclotron period. This procedure completely remove the fast rotation so it can be ignored in the ω_a fits.

5.4.7 Differential Decay

As described before, the muon beam has a momentum spread around the magic momentum. Among other effects, this also results in a range of muon decay lifetimes in the lab frame. The observed lifetime is $\gamma\tau_\mu$ with γ proportional to momentum. Therefore, lower momentum muons will decay earlier and higher momentum muons will decay later. Over the course of a fill, the average beam momentum will increase, subsequently increasing the average storage radius. This shift causes positron drift times to increase over the course of a fill, which changes the phase in the precession signal. As a result of the momentum spread, phase becomes a function of time in fill. As with other early-to-late effects, this differential decay behavior can bias the ω_a measurement.

To leading order, the stored beam's average momentum increases linearly in time. Given a 0.15% spread in momentum at injection, the average beam momentum will shift by about 100 keV/c over the course of a fill [29]. This shift is small compared to the average momentum of 3.09 GeV/c but still non-negligible considering the ambitious systematic uncertainty budget of E989. Estimating the size of this bias can be done by measuring the phase-momentum correlation and the rate at which the average momentum is changing over a fill [25],

$$\Delta\omega_a = \frac{d\phi_a}{dt} = \frac{d\phi_a}{d<\delta>}\frac{d<\delta>}{dt} \tag{5.15}$$

where $\delta = (p - p_m)/p_m$. The first term in the product is the phase-momentum correlation and is extracted from a study of muon losses [49]. The g-2 storage ring accepts a small slice of the wide range of momenta that arrive from the delivery ring. The field setting determines which portion of the incoming distribution is selected. Therefore, by varying the field setting, different momentum ranges can be studied. By extracting

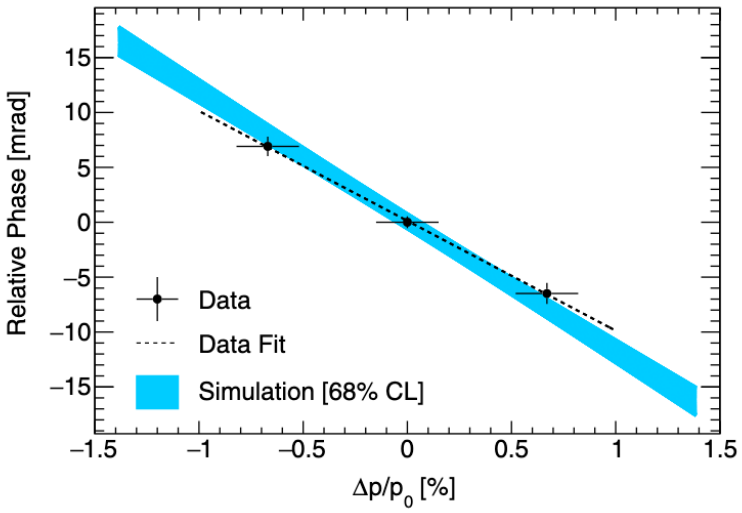


Figure 5.11: Comparison of phase-momentum correlation between end-to-end simulation and data showing good agreement. The three data points are obtained by fits to muon precession frequency data at nominal, reduced, and increased central magnetic field values. Figure reproduced from Reference [25].

the average phase for each field setting, and consequently each momentum, a phase-momentum correlation can be constructed.

The second term in Equation 5.15 can be determined from an analysis of the fast rotation signal. Fourier analysis extracts the x_{eq} distribution, then the relation

$$\delta = (1 - n)\frac{x_e q}{R_0} \tag{5.16}$$

is applied to get the muon decay distribution. By numerical integration and differentiation, $d\delta/dt$ can be calculated. Combining $d\delta/dt$ with the phase-momentum correlation provides the shift in ω_a from differential decay. Preliminary estimates for the systematic uncertainty due to differential decay in Run 1 data are shown in Reference [50].

Chapter 6

SLAC Test Beam Experiment

The development of the calorimeter system involved years of study and development, including several test beam experiments, meant to evaluate the performance of the system. This chapter reviews a 2016 test beam experiment of the whole calorimeter system. The next chapter presents a detailed study of the read-out electronics of the calorimeter SiPMs. Together, these tests demonstrate that the calorimeter system meets the technical requirements for E989.

A single calorimeter station includes the following subsystems: an array of 54 PbF_2 Cherenkov crystals read out by large-area SiPMs, bias and slow-control electronics, a suite of 800 MSPS waveform digitizers, a clock and control distribution network, a gain calibration and monitoring system, and a GPU-based frontend read out through a MIDAS data acquisition environment. The entire system performance was evaluated using 2.5-5 GeV electrons at the End Station Test Beam at SLAC. Energy response and resolution, energy-scale stability, timing resolution, and spatial uniformity were measured and found to meet technical requirements.

6.1 Technical Requirement of the Calorimeter System

In this section, the technical requirements of the calorimeter system at the time of the 2016 SLAC test beam experiement are given, which includes not only the PbF2 calorimeter itself, but downstream components

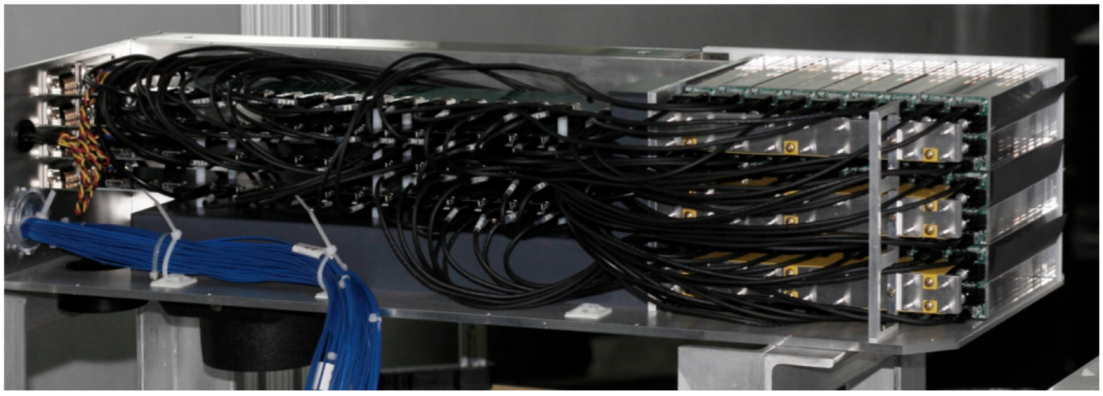


Figure 6.1: The inside of the production calorimeter tested at SLAC in June 2016.

such as SiPMS, waveform digitizers, and DAQ. The calorimeter system must continuously record data throughout the 700μs muon fill after each accelerator trigger. For a fill, each calorimeter station produces about 800 MB/s of raw digitized samples, which is filtered by the DAQ so that only regions of the trace above threshold are saved. The leading ω_a systematic uncertainties associated with the calorimeter are multi-particle pileup and gain stability. Both are exacerbated by the instantaneous rate that can exceed 10 MHz just after injection, but then drops by a factor of about 50,000 over the course of a fill. Because of muon beam cleaning and debunching requirements, the typical start-time of a fit for ω_a is 30μs after injection. A combination of lessons learned from E821 and various Geant4 simulations establishes several necessary performance parameters. These, along with practical considerations, motivate the following list of system requirements [39]:

- The energy resolution at 2 GeV should be better than 5%.
- The calorimeter gain must recover by 30μs following the intense flash at injection.
- The calorimeter gain must remain stable during the 30-700μs measurement period.
- The laser calibration system must be able to correct for residual gain instabilities to better than 4 x 10^{-4} during the measurement period.
- The time resolution of a reconstructed shower should be better than 100 ps for positrons with energy greater than 1.8 GeV.
- The time stability of the system must be better than 7 ps throughout any fill, to ensure less than a 10 ppb shift to ω_a.
- The calorimeter must be able to resolve two electromagnetic showers with impact time separations greater than 5 ns with 100% efficiency.
- The calorimeter must fulfill the geometrical space limitation by fitting into the scallop of the vacuum chamber.
- The calorimeter, readout, and cabling that reside adjacent to a highly uniform magnetic field must function in the field and, importantly, must not perturb the field uniformity.

6.2 Experimental Setup

The experimental setup during the test beam is shown in Figure 6.2. The calorimeter was located about 50 cm downstream of the beamline exit window. After traveling from the end of the vacuum pipe, the electron beam size on the front face of the calorimeter was 0.5 $\times$ 1.0 cm^2. The mean transverse position was stable throughout the measurement period. The calorimeter, waveform digitizers, bias control, low-voltage, and frontend computer were located inside the beam tunnel. The laser and monitoring system was located just outside of the tunnel, and the DAQ backend and analysis machines were located in the control room several floors above the tunnel. This setup is representative of the distributed setup now installed in E989.

The SLAC beamline provides a well-collimated beam of electrons at a user-defined intensity, with a typical beam-pulse frequency of 5 Hz. In each precisely timed pulse, a Poisson-distributed number of electrons arrive. During the normal mode of operation, the single-electron beam event was optimized at a probability of 37%. Energies from 2.5 to 5 GeV were used in evaluating the performance of the calorimeter system. Once the

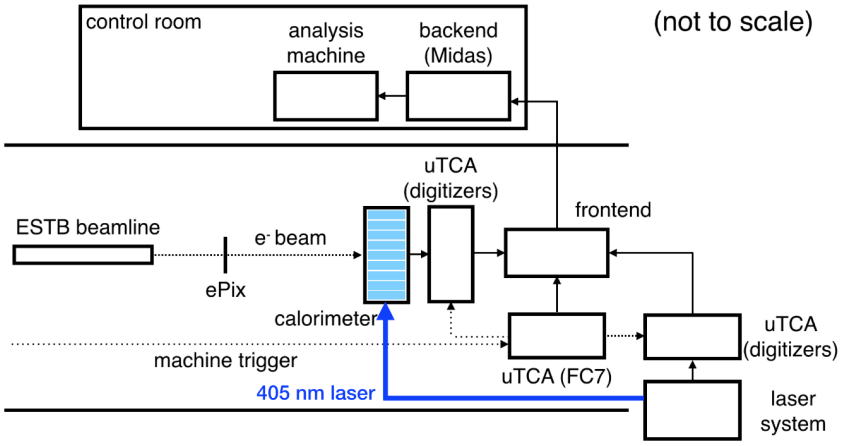


Figure 6.2: Overview of the experimental setup at SLAC. Electron beam from the ESTB beamline is moving from the left toright before hitting the front face of the calorimeter. The SiPM pulses resulting from electromagnetic showers, or from laserpulses, are digitized and then processed by the frontend and backend machines to be ready for data analysis. Figure reproduced from Reference [39].

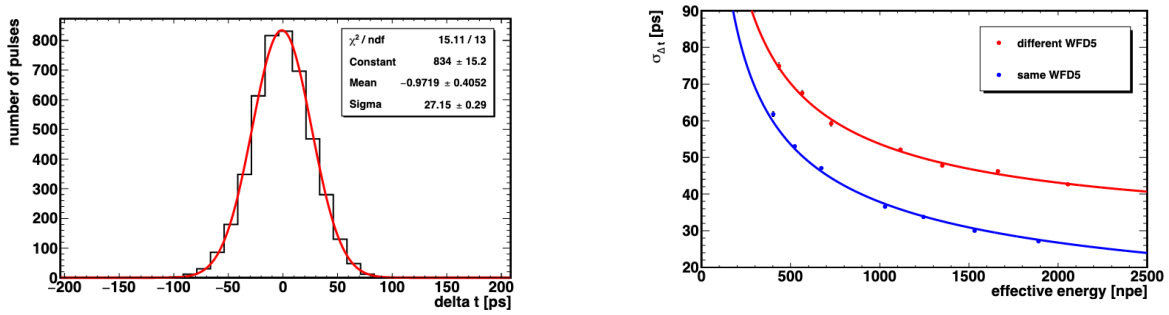
beam energy was established, the rate was stable and the energy constant to better than 1%. Due to the fact that some hours of setup were required to choose new beam energies, the study of linearity by sweeping beam energies was somewhat limited. With these considerations, it was prudent to fix 3 GeV as the nominal energy for the bulk of the data taking, which corresponds to the endpoint energy of the decay positron in the E989 experiment. Approximately 3 μs prior to the arrival of the beam, a machine trigger was received from the SLAC accelerator team. This trigger was then fed into the FC7 to be encoded together with the 40 MHz clock. The FC7 then sent TTC signals to the AMC13 in its μTCA crate and also to the μTCA crates of calorimeter and laser systems, which initiated digitization of the waveform digitizers in both crates. The FC7 also sent a NIM signal to a Laser Control Board which triggered the laser head in a pre-configured laser firing pattern following a 1 μs delay.

6.3 Performance

6.3.1 Timing Resolution

The timing measurement of the calorimeters is driven by three factors: the transit time of the SiPM and backend electronics, the statistical fluctuation of photons triggering SiPM pixels, and the light propagation time through the crystal.

The timing resolution due to the behavior of the SiPM can be extracted using laser events that arrive at all SiPMs at about the same time. The time difference distribution between two waveform digitizer channels of the same laser event is shown in Figure 6.3a. The red line is a Gaussian fit to the distribution and the standard deviation is 27 ps for this particular set of waveform digitizer channels. The energy dependence of this timing resolution is studied for two different pairs: crystals read out by the same, or different, waveform digitizers. The standard deviation of the time difference distribution is plotted against energy in Figure 6.3b. The difference in the timing resolution between blue and red lines is attributed to the timing jitter of the



(a) (b)

Figure 6.3: (a) The time difference distribution between two WFD5 channels for the same laser event. (b) Standard deviation of the time difference distribution versus effective energy for laser events read out by the same WFD5s (blue), or different WFD5s (red). Figures reproduced from Reference [39].

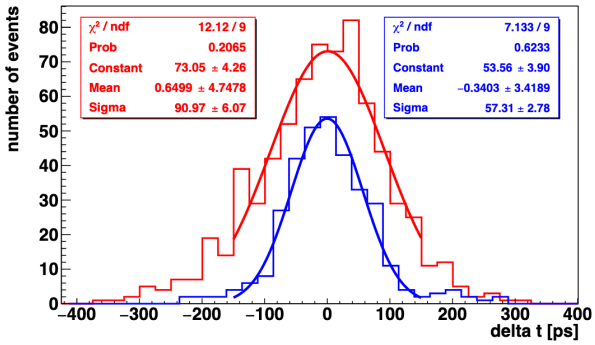


Figure 6.4: Distribution of the time difference between two channels from (blue) the same WFD5 and (red) different WFD5, for the same electron event. Figure reproduced from Reference [39].

800-MHz clock between two different WFD5s.

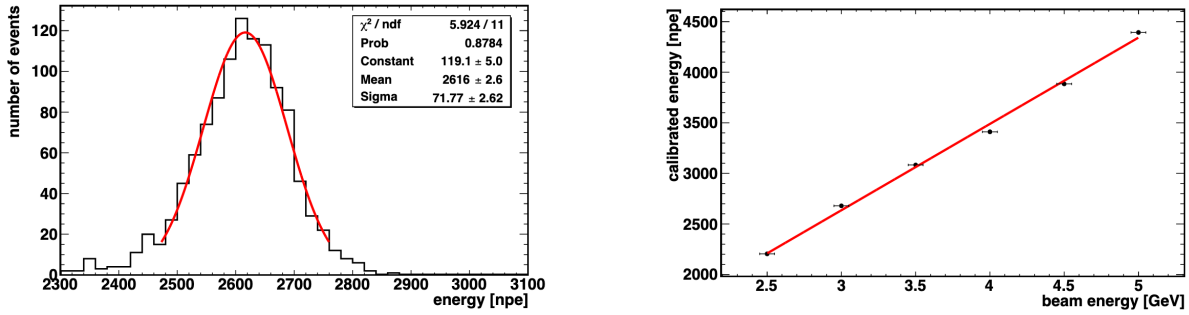
To extract the timing resolution of an electromagnetic shower, we studied the time difference between two calorimeter channels for electron events. The distribution of the time difference is shown in Figure 6.4, for two channels from the same WFD5 and different WFD5s. The single channel timing resolution for a 3 GeV electron event is about 40 ps. A systematic and precise way of quantifying this resolution is difficult due to the broad beam size and uncertainty in the beam hit position.

6.3.2 Energy Resolution

Figure 6.5a shows the energy distribution when a 3 GeV beam is centered at a particular crystal. The red line is a Gaussian fit within $\pm 2\sigma$ around the mean value. The fitted energy resolution here is 2.7%.

To extract the energy resolution and linearity functions, beam energies in the range 2.5 to 5 GeV were used. The reconstructed energy distribution for each beam energy was fitted to a Gaussian function to determine the mean and width. The linearity result is shown in Fig. 6.5b. The range extends well beyond the decay energy endpoint for the E989 experiment, which is at about 3.1 GeV.

Figure 6.6 shows the dependence of the energy resolution σ_E/E as a function of electron energy. The energy resolution at 2 GeV is 3.1%, surpassing the design target of 5%.



(a) (b)

Figure 6.5: (a) Measured cluster energy distribution for 3 GeV electrons aimed at a typical crystal. (b) Reconstructed and calibrated electron energies as a function of nominal beam energy. Figures reproduced from Reference [39].

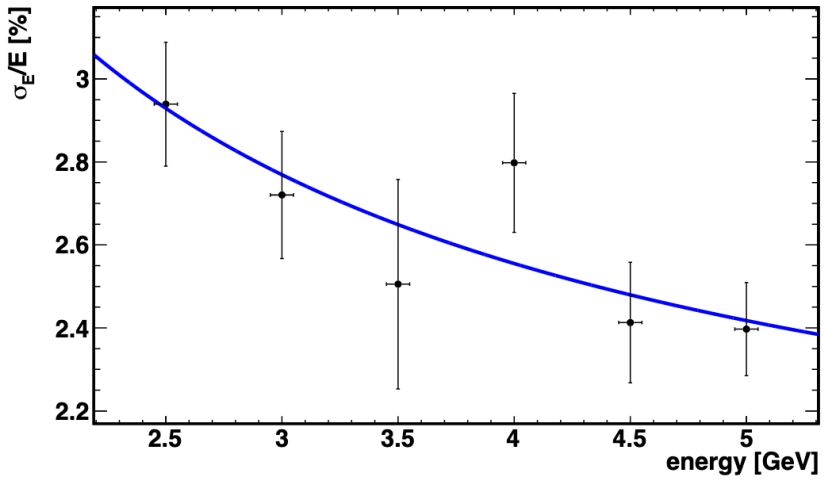


Figure 6.6: Energy resolution as a function of beam energy. Figure reproduced from Reference [39].

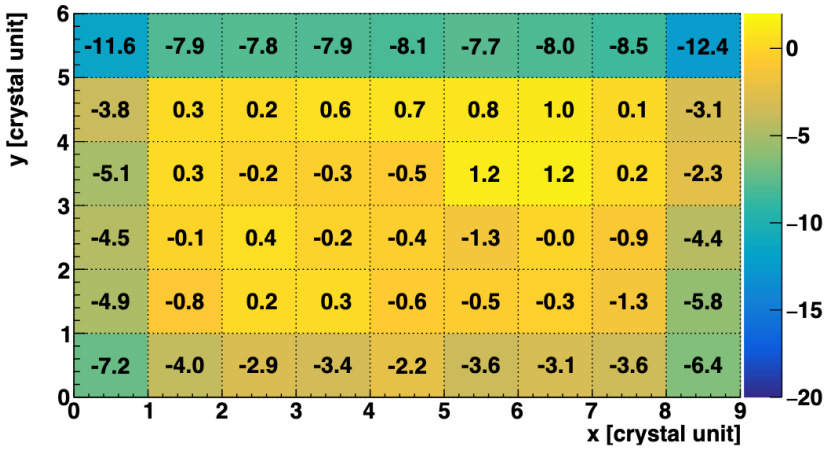


Figure 6.7: Spatial uniformity of the energy response of a cluster when the electron beam is impinging near the center of each calorimeter channel. The scale is in percent with respect to the average of non-corner channels. [39]

6.3.3 Spatial Uniformity

An important aspect of the calorimeter is the spatial uniformity of the response. This was studied by comparing the energy response of the calorimeter for various beam impact positions. Figure 6.7 shows the deviation from the mean reconstructed cluster energy in percent for each channel when the electron beam is impinging on the center of each channel. The homogeneity is better than 2% for non-corner channels. Lower reconstructed energies for corner channels, as well as the rows and columns along the outer edge, are expected due to the leakage of electromagnetic showers. The reconstructed cluster energy as a function of beam position is stable at the 2% level.

6.3.4 Conclusion of SLAC Beam Test

Overall, the calorimeter system was found to meet technical requirements during the beam test. The design was frozen at this point and the rest of the calorimeter system went into production. The next chapter presents some studies of the backend electronics of the calorimeter system which occured in situ at the Fermilab Muon Campus during the installation period prior to Run 1.

Chapter 7

Timing and Synchronization Tests

After the 2016 SLAC test beam, we performed a study to understand the intrinsic timing of the electronics populating the μTCA crates deployed to read-out the calorimeter SiPMs. The study included the timing difference between the five read-out channels on each of the waveform digitizers (WFD5) populating the 12 μTCA AMC slots and the timing difference between the WFD5 in the difference AMC slots. Additionally, we observed the impact of power cycling crates and resetting individual WFD5s on these timing differences. These tests are motivated by findings from the SLAC run data, where timing shifts between crystals were observed in sync pulse (laser) data. Although we can use the laser to synchronize crystals and thus correct for these offsets, a test of the stripped down system was required in order to understand the intrinsic timing differences of the essential electronics.

7.1 Calorimeter Chain Test

An overview of the setup is illustrated in Figure 7.1. From the encoder FC7 in the clock and controls crate (CCC), an external trigger is sent to a NIM pulser a few feet away. The pulser provides a roughly 25 ns wide square pulse which is fed into a high-pass filter (splitter) which outputs five identical pulses. Each of these pulses are given to a test driver that produces narrow pulses that more closely resemble what we see from the SiPMs. Finally, each of these five pulses are passed to one of the five channels of a single WFD5. Twelve WFD5 populate a μTCA crate, along with an AMC13 module which is responsible for packaging the digitzation data from each WFD5 and passing it along to the DAQ system via an optical data link. The setup allowed the primary pulse to be split into only five copies therefore making it impossible to test more than five channels at a time. The digitized pulses are processed by the remainder of the chain in the standardized way, becoming MIDAS banks which can be unpacked later in the *art* framework.

The offline analysis performs, among other processing, template fitting of the digitized pulses to extract the timing information. Therefore, it requires building a template for each WFD5 channel since the timing extraction is affected by the fidelity of the template to the digitized pulse and small variation in the electronics chain lead to slightly different templates. Thus, before collecting synchronous pulse data, we needed to collect asynchronous template data from which to build templates. This asynchronous data taking mode ensures that we collect pulses at all possible phases such that every slice of the pulse shape is digitized. To run asynchrounsly, the NIM pulser was set to trigger itself at 100kHz in order to collect many pulses which could be overlaid offline to build a template with a cubic spline. Alternatively, to run synchronously, the NIM

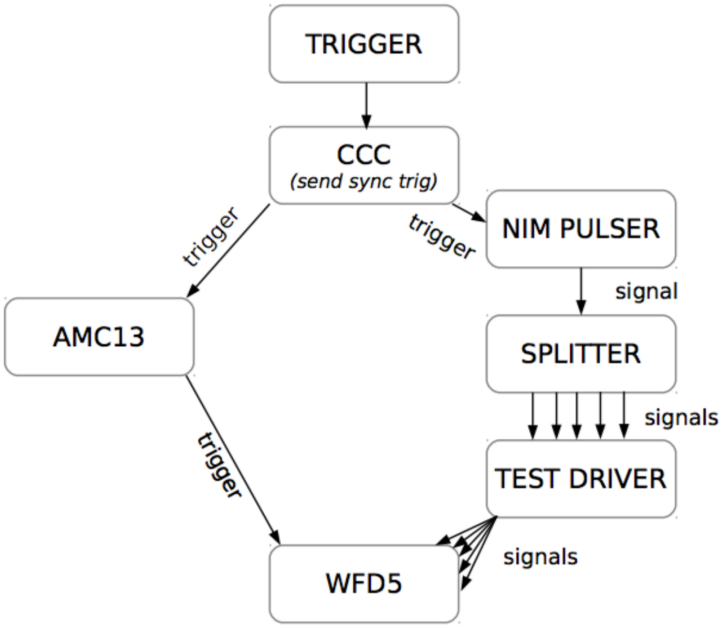


Figure 7.1: Overview of the test setup.

pulser was set to receive the trigger from the FC7 such that one pulse per trigger is received.

The offline analysis performs, among other processing, template fitting of the digitized pulses to extract the timing information. Therefore, it requires building a template for each WFD5 channel since the timing extraction is affected by the fidelity of the template to the digitized pulse and small variation in the electronics chain lead to slightly different templates. Thus, before collecting synchronous pulse data, we needed to collect asynchronous template data from which to build templates. This asynchronous data taking mode ensures that we collect pulses at all possible phases such that every slice of the pulse shape is digitized. To run asynchrounsly, the NIM pulser was set to trigger itself at 100kHz in order to collect many pulses which could be overlaid offline to build a template with a cubic spline. Alternatively, to run synchronously, the NIM pulser was set to receive the trigger from the FC7 such that one pulse per trigger is received. For both synchronous and asynchronous data, the MIDAS banks must be unpacked with *art*. Asynchronous data islands are chopped and unpacked, then a template for each channel is created. Once we have a template for each channel, we can unpack the synchronous data, with the appropriate templates as inputs. For each pulse, the fitter extracts a peak time and pulse energy. By comparing hit times in different channels on a trigger-by-trigger basis, we observe the intrinsic offsets between channels and the resolution of these differences.

Before sending pulses to all the digitizers, we characterized the upstream chains of our setup. Moving back from the digitizer, we have a pentapus cable which goes through five channels of the test driver, BNC connection to the splitter, and out to the pulser. To be sure none of these components were introducing large systematic errors into our data, we fed the five outputs of the test driver into a single WFD5 channel (slot 1 channel 0) one by one. Templates for each 'upstream chain' (i.e. the signal coming out of each test driver channel) were created using the same method used for the actual test data. Seven sets of data were taken over the course of a few days. At most, there was a systematic shift due to the upstream chains of

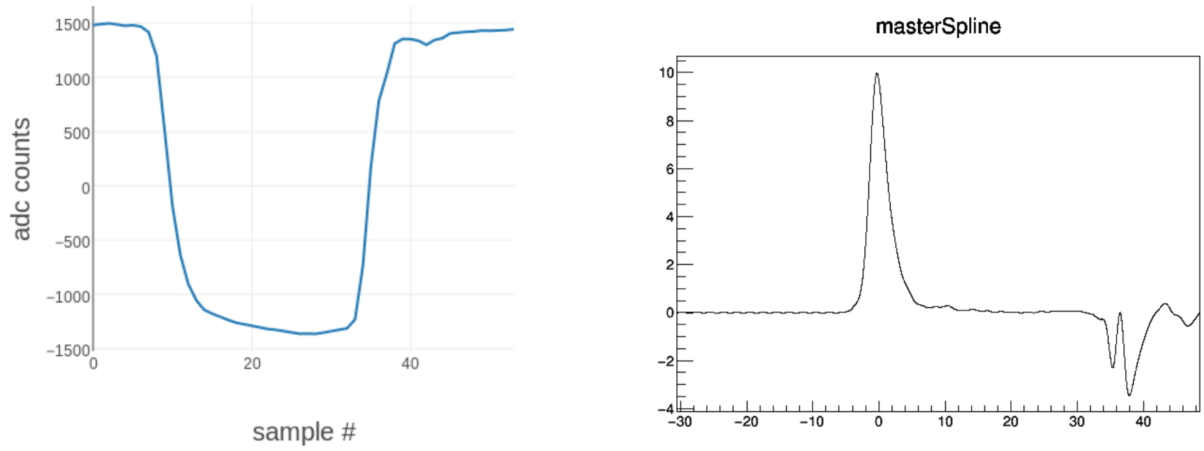


Figure 7.2: Left: The pulse provided by the NIM pulser, as seen by the DQM (data quality monitor). Right: When the splitter is added to the chain, the rising edge of the square pulse gives way to this narrow peak.

approximately 0.25 ns, although most tests showed a systematic shift of less than 0.08 ns.

As mentioned above, these tests were motivated by some behaviors observed at the SLAC test beam, namely a jump of 2 clock ticks[1] within a single channel that occasionally occured after a new trigger. This was determined to be a result of jitter between the 800 MHz digitizer and 40 MHz clock which sometimes causes the time to skip 2 clock ticks. We observed this behavior in our tests as well (Figure 7.3) and included a correction in the analyses. In addition to seeing clock jumps within a channel, we observed time jumps between channels in a digitizer of integer clock ticks. An example of this is shown in Figure 7.4, where all channel times are shown with respect to channel 0. In that plot, there are distinct horizontal lines made by the points of different channels, which jump up or down by about 1 clock tick. Once these were corrected for, it was easy to see the intrinsic timing differences between channels, which was the same across all digitizers. As we began these tests in March 2017, while installation was underway, the number of calorimeter crates available for these tests rapdily diminished over the course of month. Thus, these tests were only performed on crates 9, 26, and 24, although we have reason to believe that the timing behavior should be the same for all detector crates.

In addition to the standard tests across all 12 slots, we did a WFD5 "reset" test on slot 1. In this test, we reset the digitizer 5 times, taking 3 sets of pulse data each time. The purpose of this was to try and observe the behavior seen at SLAC, in which the digitizer jumps a clock tick after a reset. The results are summarized in Figure 7.5. It's not clear why this particular up-down pattern emerged in our results; we expected to see the jumps occur more randomly but the statistics here are far fewer than at SLAC.

Figure 7.7 presents the results of the final study conducted using the test calorimeter chain setup. By taking the time difference between channel 0 and channel $n = 1, 2, 3, 4$ on a trigger-by-trigger basis, we construct a histogram of time differences, as in Figures 7.6. Fitting with a Gaussian allows us to extract the standard deviation of the time differences which gives us the resolution between two channels. We found the resolution between two different channels in the same digitizer to be well below the requirement, as shown in Figure 7.7. We also observed the resolution between different channels in different digitizers to meet the needed specification.

[1] 1 clock tick = 1.25 nanoseconds

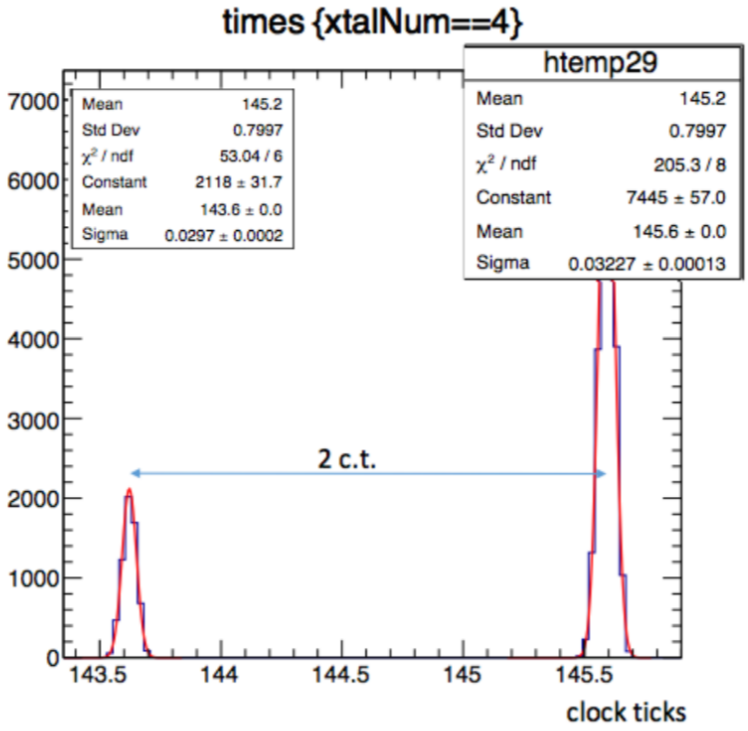


Figure 7.3: Histograms of pulse times in a single channel. Two distinct peaks illustrate the 2 clock tick (2.5 ns) jump of the digitizer which occurs occasionally. We correct by taking all the times in the smaller peak and shifting by 2 clock ticks.

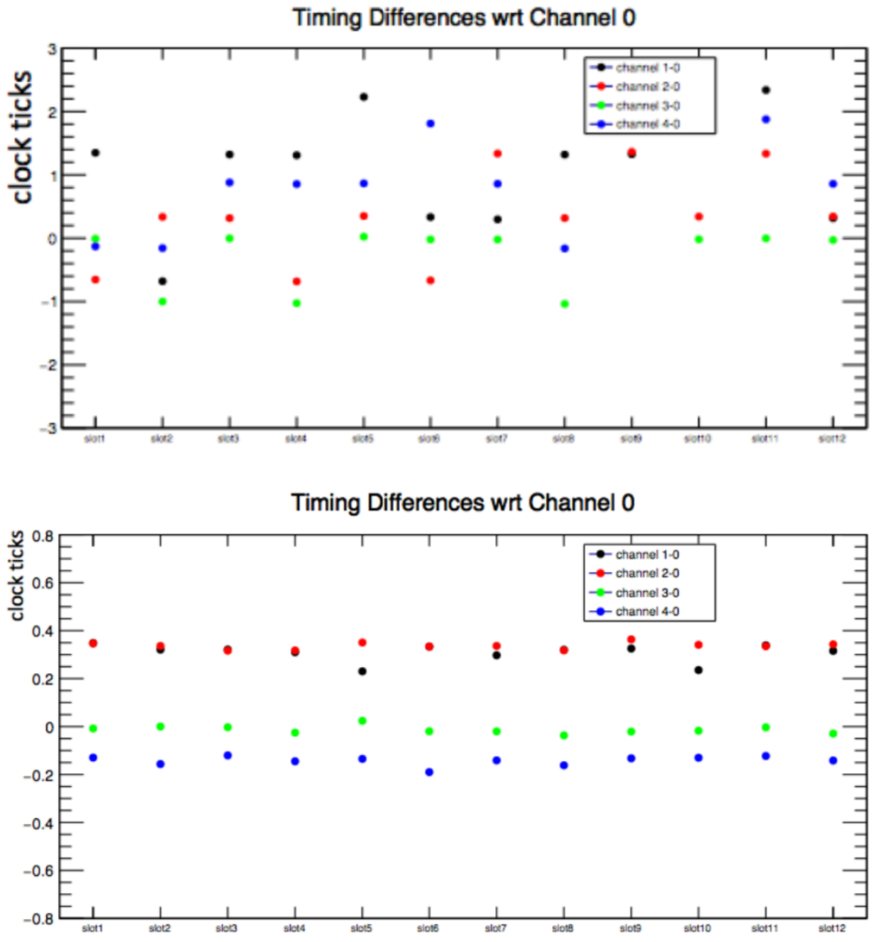


Figure 7.4: Crate 26. Top: Before corrections. Bottom: After corrections.

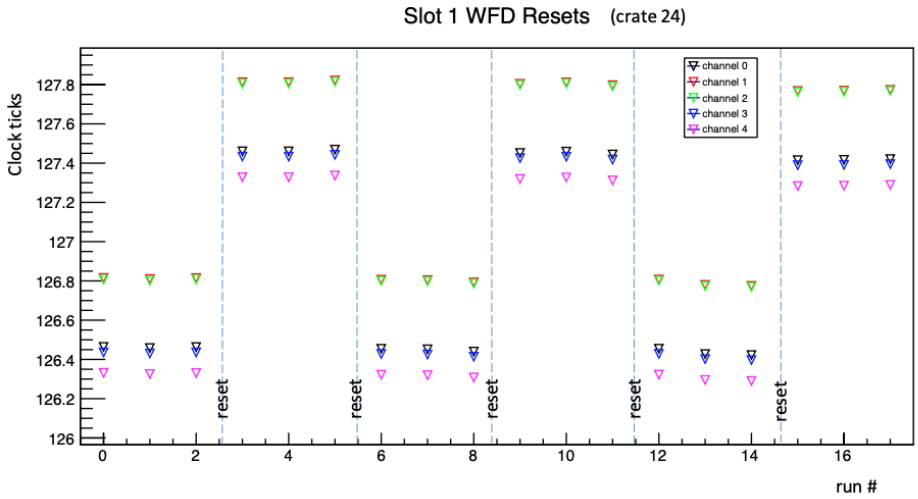


Figure 7.5: Resetting a single WFD5 five times, taking three sets of pulse data between each reset, resulting in 18 sets of data total. Relative timing differences between channels remain stable, though absolute pulse times appear to oscillate between two states separated by a clock tick. Data was taken in the crate for calorimeter 24.

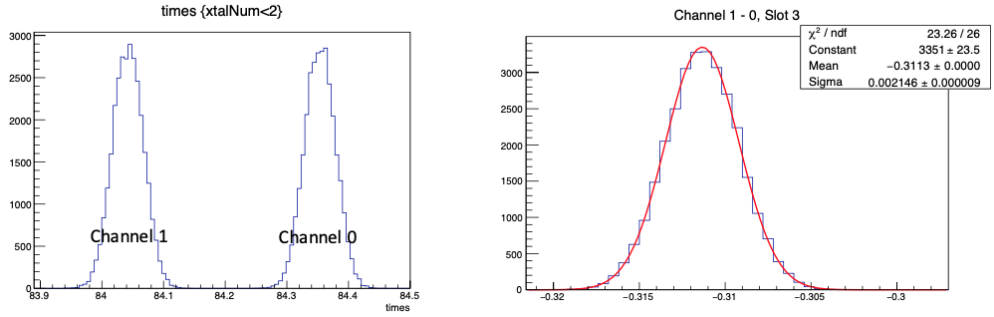


Figure 7.6: The timing resolution between channels is extracted by taking the time difference between two channels and fitting the histogram of these time differences to a Gaussian.

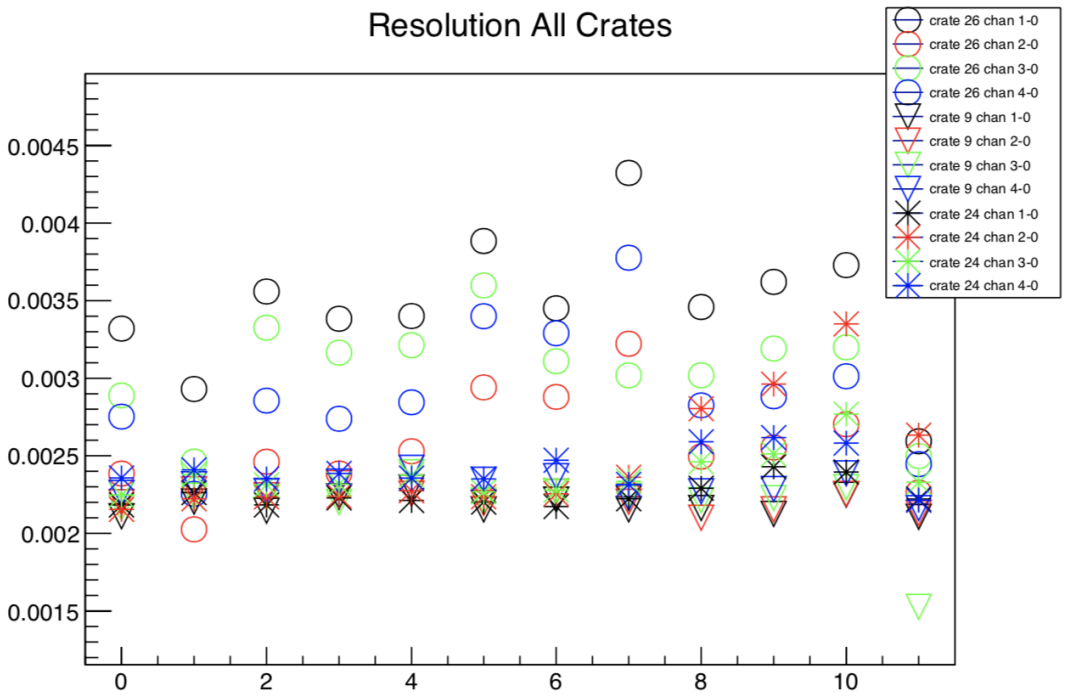


Figure 7.7: Summary of timing resolution between two channels for all 3 crates, associated with calorimeters 9, 24, and 26. Y-axis is clock ticks. X-axis is slot number. Timing resolution between channels is better than roughly 0.004 clock ticks = 5 picoseconds.

In summary, the timing and synchronization tests characterized timing behavior of components upstream of the waveform digitizers, aligned digitizer channels within a single digitizer to within 50 picoseconds, and observed timing jumps of 1 - 2 clock ticks due to reseting and power cycling various components. Overall, the behavior observed meets technical requirements for the calorimeter system and should not introduce any systematic effects into ω_a data.

Chapter 8

Anomalous Precession Frequency Analysis with Run 2 Data

E989 collected data for Run 2 between March and July 2019. In contrast to Run 1, which had variable kicker and quad settings throughout, Run 2 is considerably more stable. During Run 1, problems with some resistors in the quad system caused the CBO frequency to change over time and contributed to an unstable beam position. Since this problem was fixed for Run 2, the CBO frequency is now constant after scraping. Fewer muons were lost in Run 2, although several datasets show a lost muon spectra that differs in shape from expectation.

The datasets used in this analysis are referred to as 2C, 2D, 2E, and 2F. Several smaller datasets remain in Run 2 but were not included in this analysis due to data processing timelines. From looking at Figure 8.1, it is apparent that the datasets left out of this analysis are a small fraction of Run 2 and in fact, the datasets presented here yield an improved statistical precision over the Run 1 data. At the time of this writing, E989 is currently wrapping up data-taking on Run 4. Run 3 collected about 15 billion positrons above threshold and Run 4 is projected to surpass Run 3 by more than a factor of two.

The work presented in this chapter contains a preliminary analysis of calorimeter data using the Ratio Method. Section 8.4 summarizes the results of the R extraction, where R is the blinded ω_a parameter. Section 8.5 gives an overview of the systematic uncertainty assesment for the Run 2 ω_a measurement. The chapter ends with a consideration of the possibility of extracting R from a combined dataset, in Section 8.6. The following chapter will draw conclusions about the results presented here and desribe the next steps in the Run 2 ω_a analysis. As the analysis is incomplete, data remains fully blinded. A value for ω_a will not be revealed here, but at some future time when sufficient Run 2 analysis groups have completed their analyses and reached consensus on their work.

8.1 Analysis Overview

After calorimeter data is processed into positron clusters by the reconstruction, time and energy spectra histograms are filled. At this juncture, the procedure for organizing and analyzing the data becomes dependent on the individual or group performing the analysis. Additionally, software blindings are applied by individuals in their fitting code. This discourages analyzers from developing expectations about the value of R that they should measure, which could bias the analysis. The procedure used in this analysis is outlined

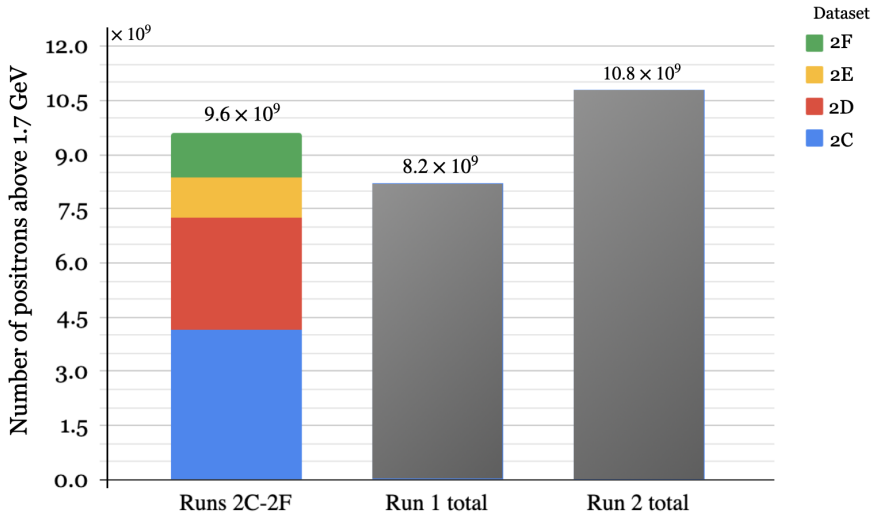


Figure 8.1: Number of positrons above 1.7 GeV in the datasets used in the analysis (2C, 2D, 2E, 2F), compared to the those in Run 1 and Run 2.

Run 2 Precession Frequency Analysis Datasets	
Dataset Name	Number of $e^+ > 1.7$ GeV
2C	4.16×10^9
2D	3.09×10^9
2E	1.11×10^9
2F	1.24×10^9

Table 8.1: All datasets in Run 2 were collected with the quad high voltage set to 18.3 kV and kicker voltages were 47.75 kV.

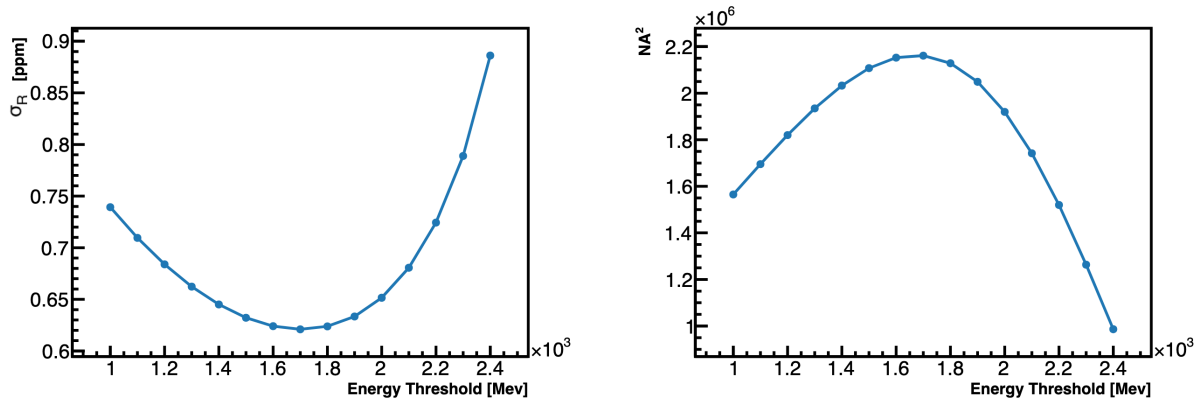


Figure 8.2: NA^2 and σ_R as a function of energy threshold in the T-Method for 2C data. The optimal energy threshold can be determined from both these quantities. For the basic T-Method, the statistical precision of ω_a is maximized when NA^2 is at a maximum [34]. Both assessments agree on an energy threshold of 1.7 GeV.

here. Alternative methods are described in detail in References [29, 51], among others.

The end products of the reconstruction are `ROOT` TTrees in which each event is a positron cluster. Data members of the TTree include the associated times, energies, and calorimeters numbers of each positron cluster. Additional information is also stored to conduct special studies; hit position, cluster size, run number, etc. These tuples are passed through an *art*[1] analysis module, where each cluster is entered into time and energy histograms, subject to cuts that optimize the ω_a fits.

The optimal energy threshold for the histogram is the one that minimizes the uncertainty on ω_a, shown in Figure 8.2. After determining this threshold from the data, the histogram is constructed by counting clusters with energies above that threshold as a function of time in the fill. To reduce the fast rotation signal from the histogram, the bin width is set to the average cyclotron period, also determined from the data. Since there is some width to the range of muon momenta that can be stored, a range of cyclotron frequencies will be present in the data. This means that binning by the average cyclotron period will not eliminate the fast rotation signal entirely, as shown in Figure 8.3. The cyclotron frequency, as well as other beam oscillation frequencies, are apparent in the FFT of the fit residuals. Though beam oscillations decay away over the course of a fill, their signal is apparent early on. To get rid of the residual signal due to cyclotron motion, a random time-offset between $-T_c/2$ and $+T_c/2$ is applied to all clusters during the histogramming stage to randomize the phase of the cyclotron motion. Combining data from all calorimeters into a single histogram also helps reduce the amplitude of beam dynamics signals in the data, as these effects are generally a function of azimuth and the beam dynamics signals from different calorimeters will interfere destructively with each other.

8.2 Ratio Method

The particular technique used in this analysis is called the Ratio Method, which has T-Method histograms as its basis. Instead of filling one T-Method histogram, the data is divided into four separate groups to fill

[1] *art* is a C++ event processing framework developed for Intensity Frontier experiments at Fermilab. *art* is used for simulation, reconstruction, and analysis in E989. More about *art* can be found in Reference [52].

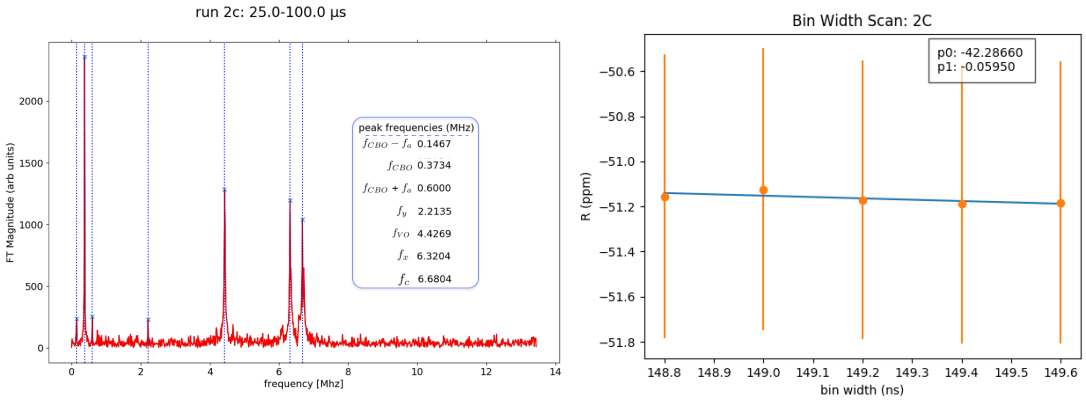


Figure 8.3: Left: FFT of the fit residuals of the 5-parameter fit to a finely binned T-Method histogram. When the bin width $<< T_c$ and no time randomization is applied, then the cyclotron frequency (6.68 MHz) is visible in the fit residuals. The peak frequencies listed on the plot correspond to the peaks marked by dotted blue lines. Smaller peaks correspond to various beat frequencies. Table 8.4 provides a description of the main frequencies seen in calorimeter data. Right: The sensitivity of R to bin width can be examined by scanning over various bin sizes. Here, the sensitivity is given by the slope of the fitted line, 60ppb/ns. The bin width chosen in the analysis comes from the fast rotation analysis which has an uncertainty less 0.1 ns. A conservative estimate for the systematic uncertainty due to binning would then be around 6 ppb.

four separate histograms. Creating four indendent ensembles of data through random assignment means the bins in the ratio are uncorrelated the the error calculation remains straighforward. The Ratio Method was conceived and implemented during E821 [53] as a way of abating slowly varying background effects. Recalling the principles of the ω_a measurement in Section 4.6, the observed positron spectrum can be represented by

$$N(t) = N_0 e^{t/\tau_\mu}(1 - Acos(\omega_a t + \phi_0)) \tag{8.1}$$

where N_0 is the overall normalization, A is the asymmetry, τ_μ is the boosted muon lifetime, and ϕ_0 is the initial phase. The Ratio histogram is constructed by splitting the data into four equal subsets (n_1, n_2, n_3, n_4) and then time-shifting two of them

$$n_1(t) = \frac{1}{4}N(t + T_a/2) \tag{8.2}$$

$$n_2(t) = \frac{1}{4}N(t - T_a/2 \tag{8.3}$$

$$n_3(t) = \frac{1}{4}N(t) \tag{8.4}$$

$$n_4(t) = \frac{1}{4}N(t) \tag{8.5}$$

where T_a is the anomalous precession period. In this analysis, T_a was set to 4.3655411 μs. Because the period of the real data is not known exactly (it is what we are measuring), there will be an uncertainty δ in the shift T_a, though the ω_a measurement turns out to be insensitive to the choice of T_a. The systematic error due to δ is calculated in Section 8.4.6. From these four histograms, the two time-shifted histograms

are combined into U(t) and the two unshifted histograms are combined into V(t).

$$U(t) = n_1(t) + n_2(t) \tag{8.6}$$

$$V(t) = n_3(t) + n_4(t) \tag{8.7}$$

The Ratio spectrum is constructed by dividing the difference of U(t) and V(t) by the sum of U(t) and V(t).

$$R(t) = \frac{U(t) - V(t)}{U(t) + V(t)} \tag{8.8}$$

As shown in Figure 8.5, the numerator is an exponentially decaying cosine, while the denominator is a simple exponential. By plugging Equation 8.1 into Equation 8.8, the model function for the time spectrum is transformed by the Ratio Method construction. The exponential term associated with muon decay gets divided out to first order and, in the absence of other effects, the spectrum is modelled by a single cosine.

$$R(t) \approx A \cdot cos(\omega_a t + \phi) \tag{8.9}$$

The outcome of ratio construction yields a histogram that looks like the one in Figure 8.6. Figures 8.4-8.5 present the intermediate spectra. For a more complete sketch of the algebra between Equation 8.8 and Equation 8.9, see Appendix A. As for the bin variances, consider first a T-Method histogram in which bin contents are large and bin counts are discrete events. These characteristics imply that the bins obey Poisson statistics, and therefore bin variances are taken to be the bin contents, as in

$$\sigma_i^2 = N_i. \tag{8.10}$$

For the Ratio histogram, which is composed of statistically independent T-Method spectra, standard error propagation leads to bin variances that are given by

$$\sigma_i^2 = \frac{1 - R_i^2}{U_i + V_i} \tag{8.11}$$

which is also derived in Appendix A.

The Ratio Method was developed as a complementary technique to the T-Method because it reduces slowly varying time-dependent effects, with comparable statistical precision to the unweighted T-Method. Though this analysis is primarily concerned with the Ratio Method, the T-Method will be referenced from time to time as it provides certain inputs and a point of comparison.

8.3 Correcting and Modeling the Data

8.3.1 Pileup Subtraction

Concurrent with the splitting of the data into the Ratio histograms is the pileup subtraction procedure. For each of the constituent Ratio histograms n_1, n_2, n_3, n_4, three additional pileup histograms are created. The rationale for the pileup construction method used in this analysis is described in Section 5.4. The method is carried out in a few steps during the histogramming routine. First, all the clusters in the same fill and calorimeter are gathered and ordered by time. Then, one-by-one the shadow window of each cluster is inspected. If there is a shadow cluster, a doublet D is constructed subject to Equation 5.1. The time and

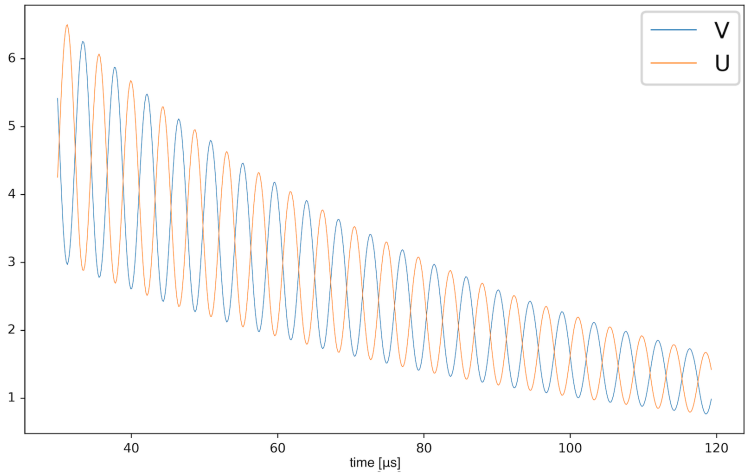


Figure 8.4: Histograms for U and V shown together to illustrate the time-shift between the two distributions. The y-axis represents counts in arbitrary units.

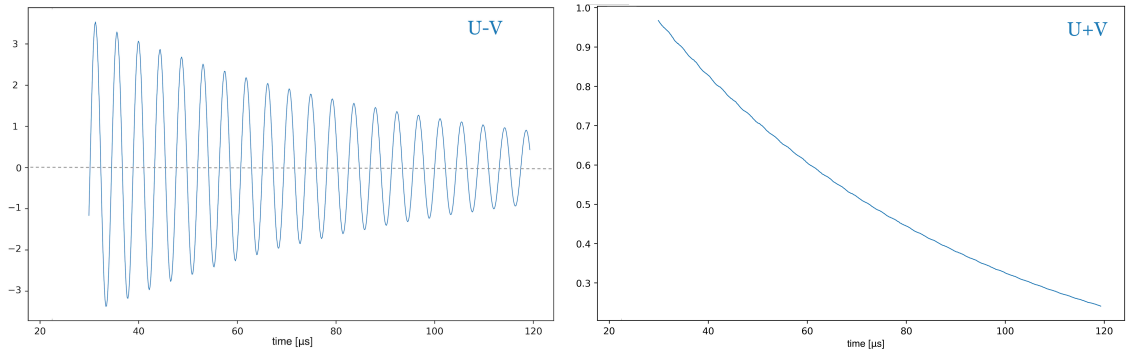


Figure 8.5: The top histogram is the difference (U-V) and is modeled by an exponentially decaying cosine. The bottom histogram is the sum (U+V) and is modeled by a decaying exponential. The ratio of these two histograms removes the exponential dependence and produces the final Ratio Method histogram. The y-axis represents counts in arbitrary units.

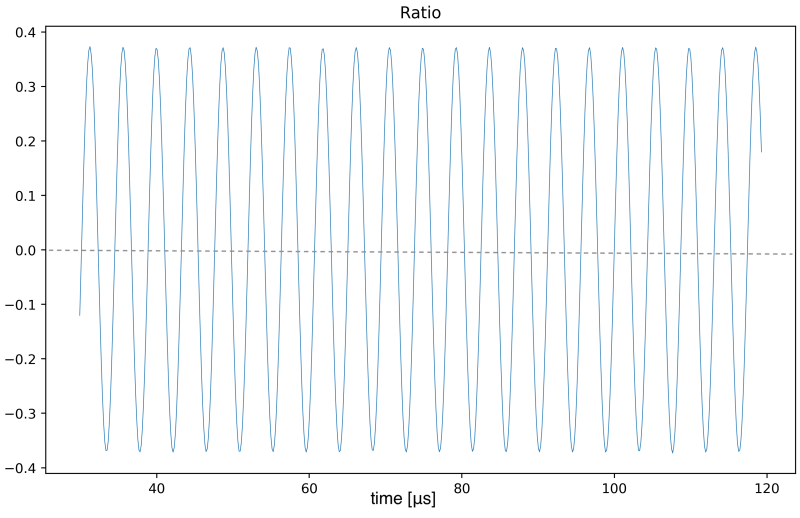


Figure 8.6: The final result of the Ratio construction is a histogram that is modeled by a simple cosine, to first order. The y-axis represents counts in arbitrary units.

Pileup Parameter		Value
shadow window	t_{SW}	20 ns
gaptime	t_G	0.53 ns
energy scaling	C	1.0
horizontal separation	DX	$\leq$ 3 crystals
vertical separation	DY	$\leq$ 3 crystals

Table 8.2: Default parameters used in the pileup construction. These parameters were found to optimize the constructed pileup in matching the pileup in the data.

energy of the singlets (trigger cluster S_1 and shadow cluster S_2) are recorded as well. Times for D, S_1, and S_2 spectra are randomized by $T_c/2$ to remove fast rotation. This results in a pileup spectrum $D - S_1 - S_2$ for each calorimeter in a fill. To return a pileup spectrum for the whole ring, these histograms are simply summed. Therefore, for a Ratio Method fit, 16 histograms must be constructed before combining them into the final ratio. The pileup subtracted time spectrum for the four histograms of the Ratio looks like: $n_i - (D_i - S_{1i} - S_{2i})$ for $i = 1, 2, 3, 4$. Since the pileup is statistically contructed and subtracted from the data, the bins in the corrected time histogram no longer obey Poisson statistics. Appendix B provides the calculation of the correct errors.

Several parameters define the pileup construction, including the width of the shadow window, the gap time between a trigger cluster and its shadow window, the spatial separation between trigger and shadow clusters, and an energy scaling parameter. A good match to the real pileup in the data requires optimization of these parameters. Knowledge of the fitter and the physics of pileup narrows down the range of ideal choices for these parameters. Well constructed pileup is marked by an energy spectrum that matches the energy spectrum of the total cluster data for energies greater than 3.1 Gev. Since the maximun energy of a single muon decay is 3.1 Gev, clusters with energy greater than 3.1 GeV are considered pileup. Additionally, constructed pileup should have a lifetime of 32.2 μs, half the muon lifetime. While the spatial separation parameter is predominantly determined by the reconstruction, other parameters are determined by a combination of effects, so a scan is performed to extract the best values. The pileup is constructed for each value in the parameter scan, holding other parameters fixed. This procedure provided the gaptime, shadow window width, and energy scaling used in this analysis. Figures 8.7-8.9 depict the results of the scans.

8.3.2 Fit Function

The fit function for the Ratio method is derived from the basic decay positron spectrum over an energy threshold (Equation 8.1), which serves as the basis for the T-Method. This function works reasonably well assuming perfect calorimeter acceptance, but this is not the situation in E989. Instead, calorimeter acceptance is modulated by the beam motion, discussed in Section 4.4, so the spectrum that shows up in the calorimeter also varies with the beam. This is not obvious from looking at the T-Method histogram by eye, but is clear from the residuals of the fit. The Fourier transform of the residuals shows peaks at expected beam oscillation frequencies as well as associated beat frequencies. Slowly varying effects, especially pileup and muons losses, show up in the FFT of the residuals as a peak at 0 MHz. Neglecting to model these effects in the fit function results in a high χ^2, indicating a poor fit. Though many beam dynamics signals are reduced

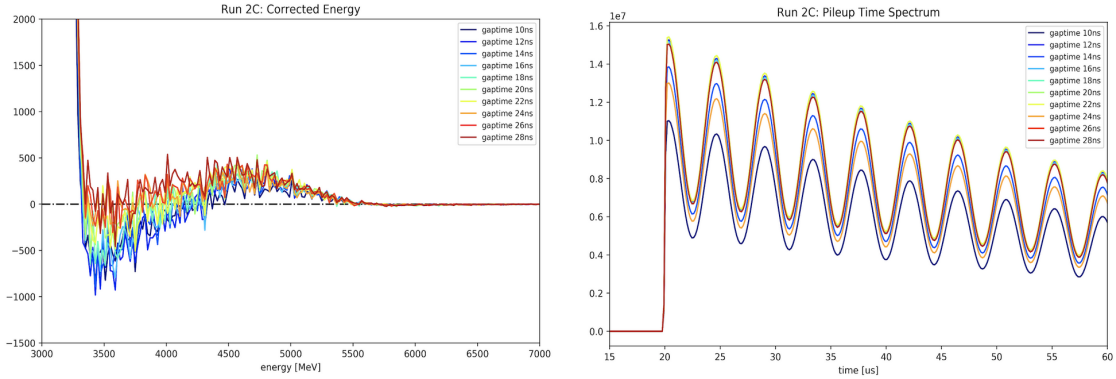


Figure 8.7: Scan over various gaptimes. Since only double pileup is constructed in this method, higher order pileup goes uncorrected and leaves behind a bump above 4GeV in the corrected energy spectrum. In the doublet range, the scan shows that a gaptime of 20ns results in the best energy correction for this dataset. The time spectra illustrate how pileup constructed differently carry different phases and amplitudes. In the energy histogram, counts are per 20 MeV and in the time histogram, counts are per 0.149 ns.

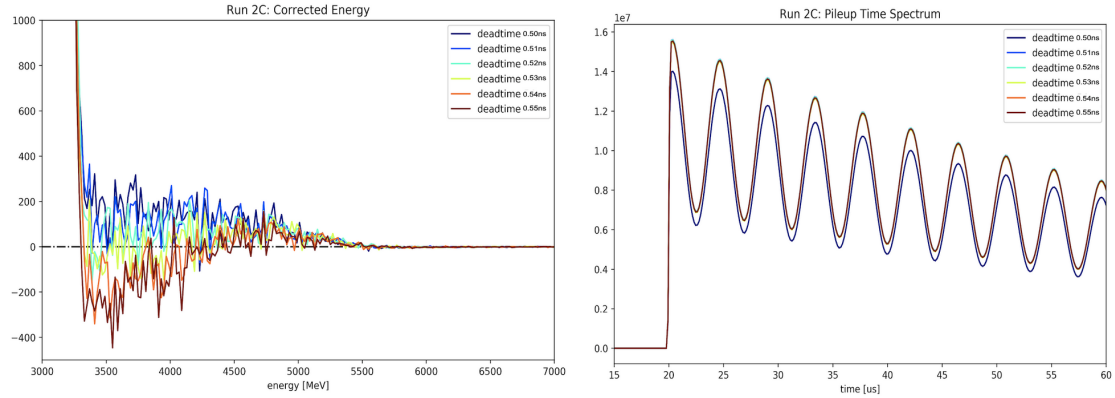


Figure 8.8: Scan over various shadow window widths, referred to in the legend as deadtime. In the doublet range, the scan shows that a deadtime of 0.53 ns results in the best energy correction for this dataset. In the energy histogram, counts are per 20 MeV and in the time histogram, counts are per 0.149 ns.

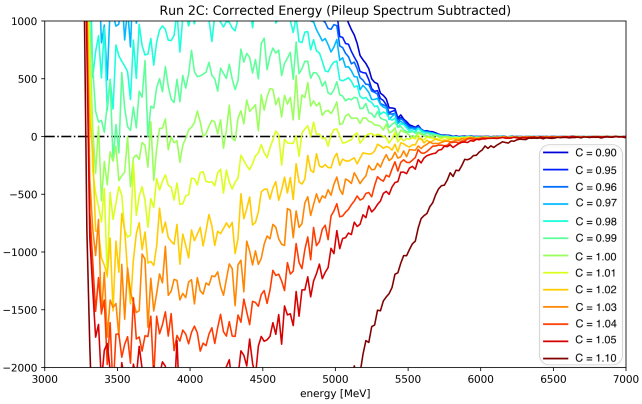


Figure 8.9: Scan over the energy scaling parameter, C. In the doublet range, the scan shows that C = 1 results in the best energy correction for this dataset. The vertical axis gives counts per 20 MeV.

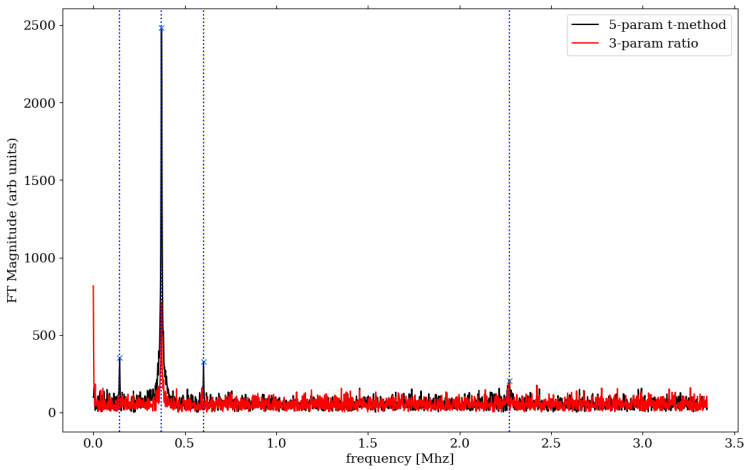


Figure 8.10: FFT of fit residuals for pileup-corrected 2C data, using the T-Method (black) and the Ratio Method (red). Equation 8.1 is used to fit the T-Method time spectrum and Equation 8.9 is used on the Ratio spectrum. Neither of these models includes CBO, which shows up as the most prominent frequency in both fit residuals. The Ratio construction, however, significantly reduces the size of the CBO in the data. Lost muons, and other slowly changing effects, show up as a peak at 0 MHz.

by the Ratio construction, they do not disappear entirely. Using the simple cosine model of Equation 8.9 yields a poor fit as well. Hence both T and Ratio methods require a upgrade to base fit function.

The function used in this analysis that describes the observed positron spectrum is

$$N(t) = N_0 \cdot N_x(t) \cdot N_y(t) \cdot \Lambda(t) \cdot e^{t/\tau_\mu} \cdot (1 + A_0 \cdot A_x(t) \cdot cos(\omega_a(R) \cdot t + \phi_0 \cdot \phi_x(t))) \tag{8.12}$$

where the fit parameter for ω_a is expressed in terms of a ppm level shift R on a reference frequency

$$\omega_a = 2\pi \cdot 0.2291 \text{ MHz} \cdot (1 + R \times 10^{-6}) \tag{8.13}$$

and the muon beam dynamics are modeled by the equations below, derived in Reference [51]

$$\begin{aligned} N_x(t) = 1 &+ e^{t/\tau_{CBO}} A_{Nx} cos(\omega_{CBO} t + \phi_{Nx}) \\ &+ e^{-2t/\tau_{CBO}} A_{2Nx} cos(2\omega_{CBO} t + \phi_{2Nx}) \end{aligned} \tag{8.14}$$

$$\begin{aligned} N_y(t) = 1 &+ e^{t/\tau_y} A_{Ny} cos(\omega_y t + \phi_{Ny}) \\ &+ e^{-2t/\tau_y} A_{2Ny} cos(2\omega_{VW} t + \phi_{2Ny}) \end{aligned} \tag{8.15}$$

$$A_x(t) = 1 + e^{t/\tau_{CBO}} A_{Ax} cos(\omega_{CBO} t + \phi_{Ax}) \tag{8.16}$$

$$\phi_x(t) = 1 + e^{t/\tau_{CBO}} A_{\phi x} cos(\omega_{CBO} t + \phi_{\phi x}) \tag{8.17}$$

This formulation is derived from the moments of the muons' spatial distribution in the storage region. Generally speaking, the first moment corresponds to the mean of the distribution while the second moment corresponds to the width. As discussed in Section 4.4, the electric and magnetic fields inside the ring cause the beam to oscillate horizontally and vertically with characteristic frequencies, ω_x and ω_y. Due to the non-

zero momentum spread of the beam, the muon ensemble will debunch, permitting oscillations to interfere destructively until the ensemble approaches an equilibrium state. Based on that understanding, the moments are assumed to take the form of an equilibrium constant plus a decaying periodic term.

The modulation of $N(t)$ due to beam oscillations is encapsulated in $N_x(t) \cdot N_y(t)$. Muon dynamics also cause oscillations of the positron energy and drift time which lead to modulations in the asymmetry and phase, respectively. These modulations are captured by $A_x(t)$ and $\phi_x(t)$. A description of the muon distribution can include an arbitrary number of moments, but the formulation presented here includes just enough terms to account for obvious frequencies in the fit residuals' FFT. Higher-order terms are negligible for the size of the dataset, or not discernible to the fitter.

The observed frequency related to horizontal beam oscillations is not ω_x but the aliased frequencies ω_{CBO} and $2\omega_{CBO}$. From tracker measurements, the CBO frequency is understood to arise from the oscillation of the muon' centroid, and therefore, associated with the first moment. In the case of vertical oscillations, the physical frequency ω_y is observed in calorimeter data as well as the aliased frequency, ω_{VW}. The vertical motion of the centroid is associated with ω_y while the width of the vertical oscillation is associated with ω_{VW}.

Changes in $N(t)$ due to muon losses are encapsulated in $\Lambda(t)$, given by [54]

$$\begin{aligned} \Lambda(t) &= 1 - K \cdot e^{t_0/\tau_\mu} \int_{t_0}^{t} L(t') \cdot e^{t'/\tau} dt' \\ &\equiv K \cdot e^{t_0/\tau_\mu} \mathcal{L}(t) \end{aligned} \tag{8.18}$$

where L(t) is the loss function constructed from triple coincidences in data. Triple coincidences refer to energy depositions in three adjacent calorimeters with a time separation of 4.5-7.5 ns and energy ∼170 MeV. Muons are expected to leave such signatures in the calorimeter data due to their minimum-ionizing nature. For each triple coincidence that is found, the time of first cluster is recorded for L(t). After finding all the triple coincidences in the data, L(t) provides the rate at which muons leave the ring as a function of time after injection. This procedure can be done with double coincidences as well, but triple coincidences are more robust against background. As with pileup, the cuts used to construct L(t) are based on knowledge of the underlying physics as well as beamline simulation. Scanning parameter space helps justify the choice of cuts used. Besides time-of-flight and energy cuts, we also consider energy fraction, that is, the relative amount of energy in the main crystal versus all the crystals in a cluster. Since muons are minimum-ionizing, they are expected to deposit almost all of their energy in a single crystal. Positrons on the other hand, will deposit energy with more spatial spread and have a lower energy fraction. Similarly, cluster size can also be used to refine the lost muon selection.

Due to the presence of material at particular azimuthal positions in the ring, such as kicker plates, collimators, quad plates, and tracking detectors, losses are not expected to be uniform around the ring. Beamline simulations and data analysis generally agree on the different rates of losses as a function of azimuth [55].

8.4 Fit Results

The model function for the time spectrum (before applying the Ratio) is given by Equation 8.10 with R blinded at the hardware and software levels. Both software and hardware blinding are consistent across the datasets in this analysis, meaning results should be comparable.

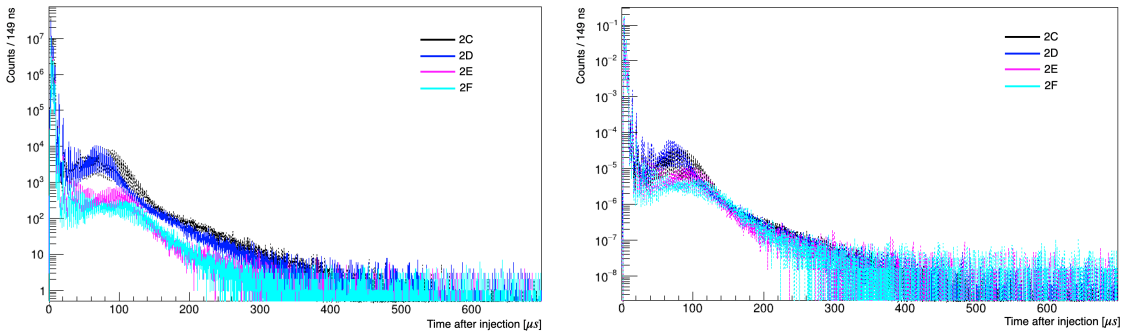


Figure 8.11: Left: The lost muons' time distribution, $L(t)$, found from triple coincidences in the 2C (black), 2D (blue), 2E (magenta) and 2F (cyan) datasets. Right: The same $L(t)$ as in the left plot but each distribution's integral is normalized to one. With the same normalization, the difference in shapes in more apparent. $L(t)$ from the 2C and 2D datasets suffer from a pronounced bump early on. The 2E and 2F datasets produce a bump that peaks later on. This shape was not observed in Run 1, though losses were much higher in Run 1 which could have concealed this feature. The bump region was found to be correlated to temperature, vertical beam position, and field settings [56].

An analytic form for the Ratio Method fit function is not easily written down. Instead, Equation 8.10 is passed through Equations 8.2-8.8 numerically in the fitting routine. Data is fit to the model function using SciPy's `least_squares` function, which minimizes the residuals between the data and the fit function. The function minimized by `least_squares` is

$$\chi^2 = \sum_i (N_i - R_i)^2/\sigma_i^2 \tag{8.19}$$

which is the sum of fit residuals divided by the bin error for bin i. N_i is the number of counts in the bin and R_i is the value of the Ratio model function in that bin. The bin uncertainty is given by

$$\sigma^2 = \frac{1-R^2}{U+V} \cdot \zeta \tag{8.20}$$

Bin uncertainties are enhanced by a factor of ζ due to the pileup subtraction. A derivation of the bin errors in the Ratio Method is given in Appendix A.

All 23 parameters are free for an initial T-Method fit. Since the Ratio Method is insensitive to some effects, results from the T-Method are used as initial inputs for the parameters in the Ratio fits. The Ratio Method fit has 21 free parameters. N_0 divides out during the Ratio construction so it does not appear in the model function at all. The muon loss parameter, K, is kept fixed in the model at the value extracted from the T-Method fit. The Ratio Method is highly insenstive to lost muons so cannot easily fit for K. Other parameters are bounded in the Ratio Method fit, such as the muon lifetime, and the beam oscillation lifetimes. The Ratio Method eliminates the exponential component of the time spectrum to first order, so all these lifetime terms are harder for the fitter to discern. Bounding τ_μ, τ_{CBO}, and τ_y to $\pm 1\%$ of the initial value returns good fit results. For fits of individual calorimeter spectra, these bounds are not enforced.

Fits to the time spectra (both T and Ratio) are done over the range 30.2-600 μs, amounting to 3820 bins. After beam scraping (t = 0 − 7 μs) the beam takes some time to stabilize. Choosing to start the fit too soon will result in problems, as the data will contain effects not described by the model function. Ending the fit too late introduces bins with insufficient statistics into the fit.

Dataset	SAM Dataset
2C	gm2pro_daq_offline_dqc_run2C_5122A
2D	gm2pro_daq_offline_dqc_run2D
2E	gm2pro_daq_offline_dqc_run2E
2F	gm2pro_daq_offline_dqc_run2F

Table 8.3: SAM dataset names for the datasets used in this analysis. Specific data quality cuts, gain corrections, and software versions can vary by SAM dataset, all of which is available in the dataset metadata. A User's Guide for SAM can be found at Reference [57].

The data analyzed in this thesis are packaged into SAM (Sequential Access via Metadata) datasets for widespread use within the collaboration. SAM is a Fermilab data handling system used to store and retrieve files and their metadata. The SAM datasets used in this analysis are listed in Table 8.3. The following sections present the results of the analysis of these datasets.

The results of the fits for all four datasets are listed in Figure **??** and the fits are drawn in Figure 8.12. In all fits, the χ^2/DoF is acceptable and FFTs of fit residuals' show no peaks about noise, indicating that the model accurately describes the data. Fit pulls and the FFT of fit residuals for the 2C dataset are shown in Figure 8.13, which are representative of all four datasets. Appendix C provides the correlation matrices for each dataset. The only fit parameter significantly correlated to R is ϕ_0, the $g-2$ phase. Though some other parameters have relatively large errors, the fact these parameters are not correlated with R improves the confidence in the R measurement. Beam oscillation parameters tend to be self-correlated.

The $g-2$ phases vary across datasets, presumably due to differences upstream of beam injection, where the initial polarization is determined. However, as described in Chapter 5, any effect that influences positron drift time can shift the measured phase. Data from other detectors upstream of the calorimeter can be used to determine the source of the small phase variations. Similarly, the $g-2$ asymmetry, A, moves around slightly across datasets. Changes in beam conditions incur changes in calorimeter acceptance which modulates the measured asymmetry. Considering the lost muon spectra for all datasets are not identical, it is reasonable to postulate that stored beams in different datasets carried small acceptance fluctuations.

Analysis of tracker data found ω_{CBO} to be about 2.3404 rad/μs [58]. The CBO frequencies in the 2D and 2E datasets are consistent with this estimate, though the CBO frequencies found from the 2C and 2F dataset vary at the ppt (parts per thousand) level. These differences can be attributed to reduced sensitivity to beam oscillations in the Ratio Method. Most fits returned results where higher order beam oscillation amplitudes carried errors comparable to the amplitudes themselves. These terms could be dropped from the fit model, but given their lack of correlation to R, these parameters were kept in the fits for consistency across datasets. Also, since this analysis used T-Method fits as guidance for the Ratio Method fits, it was appropriate to keep their fit models as comparable as possible.

The statistical uncertainties on R for the 2C, 2D, 2E, and 2F datasets are 0.63, 0.73, 1.22, and 1.14 ppm, respectively.

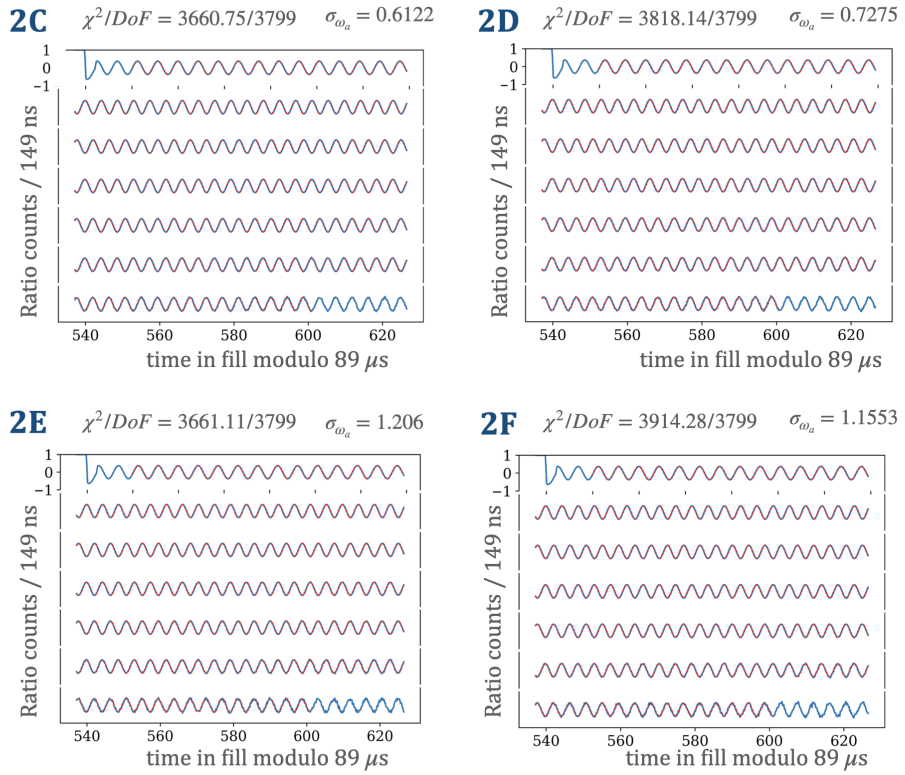


Figure 8.12: Calorimeter summed Ratio Method data for the 2C, 2D, 2E, and 2F datasets. The time spectrum starts at the top of the plot and wraps around modulo 89 μs. Data is drawn in blue and the fit result is overlaid in red, in the range 30.2-600 μs.

Observable Frequencies [MHz]		
anomalous precession	f_a	0.23
cyclotron	f_c	6.68
horizontal betatron	f_x	6.32
vertical betatron	f_y	2.26
coherent betatron oscillation	$f_{CBO} = f_c - f_x$	0.37
vertical oscillation	$f_{VO} = f_c - f_y$	4.42
vertical waist	$f_{VW} = f_c - 2f_y$	2.16

Table 8.4: The values listed are those found from an analysis of FFTs of the 2C dataset fit residuals. All frequencies, except f_a, are dependent on the field index, and therefore subject to change under different field conditions. These numbers are not static across all datasets or runs.

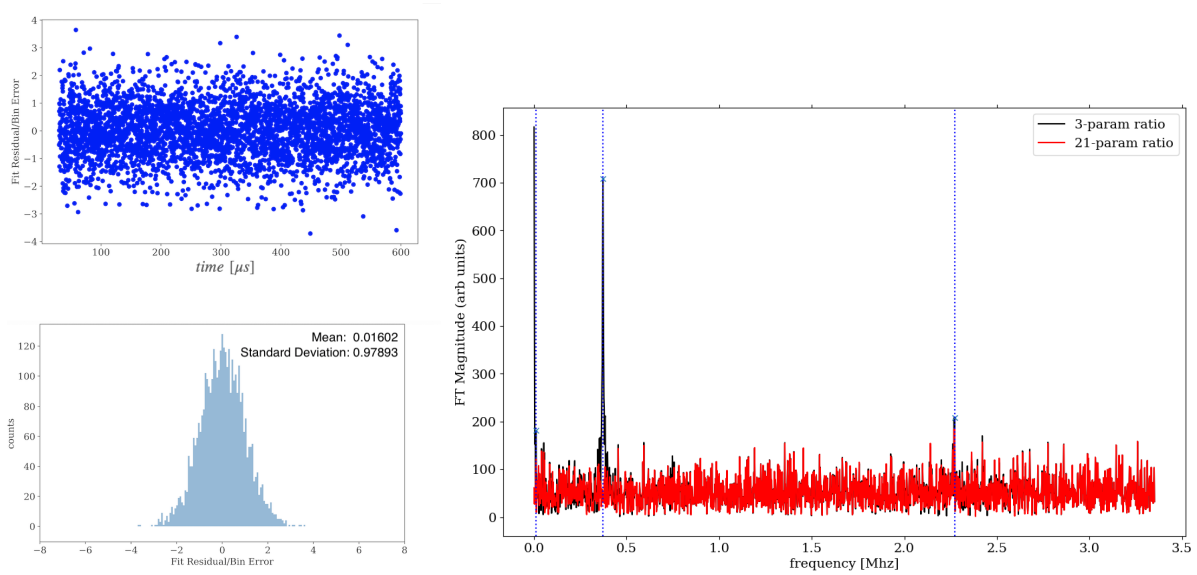


Figure 8.13: Left: Pulls (fit residuals over the bin uncertainties) for the 2C dataset. The pulls histogram has a Gaussian shape centered at zero and width of one. Right: FFT of fit residuals for the 3-parameter ratio fit model (black) and the 21-parameter ratio fit model (red). Blue dotted lines indicate the frequencies of lost muons ($\sim$ 0 MHz), CBO (0.3720 MHz), and vertical waist (2.27 MHz). No peaks above noise are present in the FFT of the 21-parameter fit.

Ratio Method Fit Results

	2C			2D			2E			2F			
χ^2/NDF	0.9466			1.0021			0.9611			0.987215			
p-value	0.9909			0.4603			0.9561			0.709503			
parameter	value	error	corr(R) %	value	error	corr(R)	value	error	corr(R)	value	error	corr(R)	bounds
A	0.37159	2.02×10^{-5}	0.5	0.36993	2.39×10^{-5}	0.5	0.37033	3.98×10^{-5}	0.5	0.3699	3.80×10^{-5}	0.5	–
R [ppm]	-51.195	0.6122	100.0	-52.513	0.7275	100.0	-52.694	1.1919	100.0	-49.088	1.1521	100.0	–
ϕ_0 [rad]	2.1667	0.00010072	-82.8	2.1655	0.00011969	-82.8	2.1638	0.00019856	-82.8	2.1684	0.00019009	-82.8	–
τ_μ [μs]	63.957	1.725	0.0	64.835	2.1206	0.0	63.781	3.3532	0.0	63.782	3.205	0.0	–
τ_{cbo} [μs]	276.21	53.664	-2.5	254.92	49.861	-2.5	257.29	88.766	-2.4	249.78	78.025	-2.2	–
ω_{cbo} [rad/μs]	2.3391	0.0007025	0.1	2.3401	0.00076653	0.3	2.3401	0.0013424	0.1	2.3427	0.0012497	0.5	[0,–]
A_{nx11}	0.0030905	0.00018859	3.4	0.0035156	0.00023006	3.5	0.0033246	0.00038045	3.3	0.0034324	0.00036607	3.2	–
ϕ_{nx11} [rad]	0.35263	0.060906	-0.3	0.34019	0.065353	-0.5	0.38714	0.11461	-0.4	0.36235	0.10663	-0.8	–
τ_y [μs]	78.813	20.233	-0.4	50.513	14.622	-0.2	47.356	22.842	-0.4	22.098	10.121	0.2	[0,–]
ω_{vw} [rad/μs]	14.263	0.0068575	-0.3	14.278	0.011857	-0.6	14.233	0.021006	-0.3	14.223	0.046483	-0.9	–
A_{ny22}	0.04452	0.014389	-0.4	0.085249	0.037722	0.0	0.056228	0.045177	0.5	0.19747	0.26228	-0.4	[-1,1]
ϕ_{ny22} [rad]	1.6643	0.31426	0.5	1.3972	0.45659	0.8	1.3907	0.8647	0.5	1.2599	1.4557	1.0	[0,2π]
A_{nx22}	0.00015863	4.69×10^{-5}	0.6	0.0002345	5.9×10^{-5}	0.9	0.00013792	9.40×10^{-5}	0.6	0.00029691	9.98×10^{-5}	0.8	–
ϕ_{nx22} [rad]	3.4266	0.29545	1.0	3.5409	0.25267	0.9	3.5127	0.68016	0.9	3.1168	0.33535	0.7	[0,–]
A_{ny11}	0.04852	0.040901	0.3	0.00042777	0.00023706	0.4	0.025235	0.019706	0.2	0.05575	0.05479	0.4	–
ϕ_{ny11} [rad]	4.2748	0.80305	0.5	0.9590734641	1.4349	0.0	4.325	1.4753	-0.2	4.127626092	1.4463	-0.2	–
ω_y [rad/μs]	14.431	0.018776	-0.4	15.039	0.027731	0.0	14.492	0.029919	0.1	11.405	0.042236	0.1	–
$A_{\phi x11}$	6.90×10^{-5}	7.22×10^{-5}	-0.5	8.65×10^{-5}	8.71×10^{-5}	0.0	0.00013031	0.00014357	0.2	0.00024043	0.00013941	0.7	–
$\phi_{\phi x11}$ [rad]	2.3142	1.0313	-0.8	-1.5869	1.0065	1.0	4.2425	1.1151	0.9	0.02621469282	0.58256	-0.1	–
A_{ax11}	0.00019	0.00015029	-2.0	0.00062846	0.00018645	-0.5	0.00024481	0.00030029	-1.9	0.00065901	0.00029775	-0.5	–
ϕ_{ax11} [rad]	7.3864	0.78919	-1.6	0.50187	0.29455	-2.5	2.2445	1.2347	1.5	0.42181	0.44853	-2.6	–
K	2.1408	–	–	2.7609			0.58074	–	–	0.1385	–	–	fixed

Table 8.5: Fit results for the 2C, 2D, 2E, and 2F datasets. All datasets share the same blinding offset. The muon loss parameter, K, is fixed at the value given by the corresponding T-Method fit. All fits begin at 30.2 μs and end at 600 μs. The bin width of all fitted histograms is 149.2μs.

8.4.1 Scans

To evaluate the quality of the fits and search for hidden systematic shifts, the data was cut up into various subsets and fitted. These scans include fits on individual calorimeter data, shifted fit start and end times, and various energy thresholds.

Fits to individual calorimeter time spectra were performed using the same model and procedure as the summed calorimeter spectra. All calorimeter fits were done on histograms with the nominal energy threshold and bin width, and the fit ranges were kept to 30.2-600 μs. Figure 8.14 shows the χ_2/DoF for the fits. With reduced statistics, the χ_2/DoF are higher than in the summed calorimeter fits but still reasonable and stable across calorimeter number. Figure 8.15 shows the fitted R values by calorimeter. These scans were fit to a straight line for each dataset, returning a fitted constant that is consistent with the calorimeter sum R values. Figures 8.16 and 8.17 show the asymmetries and $g-2$ phases for each calorimeter. Unlike R, these parameters are heavily modulated by the different acceptances which come from different calorimeter positions. The $g-2$ phases are correlated to the amount of material upstream from the calorimeter, which is especially evident at calorimeters 13 and 19 that sit behind tracker stations. The effect is consistent throughout datasets. Though R and ϕ_0 are correlated in general, the relatively large errors of the fit appear to hide any correlated effects on R. Figure 8.18 shows results of the calorimeter scan for first-order CBO parameters in the 2C dataset. The amplitudes of the CBO oscillations are about an order of magnitude larger than in the fits of summed calorimeter data. Values of the CBO phase range from 0 to 2π, as calorimeters sample different parts of the CBO oscillation. The CBO lifetime is consistent with the value from the summed calorimeter fit, though the errors are large since the Ratio construction reduces exponentially decaying contributions to the data.

Fits were also performed with varying fit start and end times. The statisically allowed deviation between two sets of data, where one is a subset of the other, is given by [22]

$$\sigma \approx \sqrt{\sigma_2^2 - \sigma_1^2} \tag{8.21}$$

where σ_2 is the error on the larger dataset and σ_1 is the error on the smaller sub-dataset. Improperly modeled effects will be observed in fit time scans as drifting away from the statistically allowed deviation. For example, in Run 1, the CBO frequency changed over the course of a fill, which was readily observed in a scan of the fit start times. Figure 8.22 shows that this effect has vanished in Run 2. Other start time scans are show in Figures 8.19-8.22. The asymmetry is stable with start time across datasets, indicating that the pileup subtraction has been corrected applied. Without pileup correction, the asymmetry will start several σ below the correct value and drift upwards with fit start time. This is because pileup contaminates the histogram at early times with low energy positrons which carry lower asymmetries. Similarly, the muon lifetime scan is stable only when the muon loss correction is properly applied, though this effect is really only visible in the T-Method fits. The Ratio Method is fairly insensitive to the muon lifetime, so the plots of τ_μ versus fit start time are not necessarily informative.

R versus start time appears consistent with statistical variations. The increased errors of the CBO amplitude and lifetime versus start time indicates that the CBO signal diminishes substantially in the fit with time. CBO frequency and phase drift outside the allowed statistical bands at late start times in the 2C dataset. In other datasets, CBO frequency stays within or close to the 1σ bands. These results are consistent with the assertion from the tracker data analysis that CBO frequency is constant with time in Run 2.

End time scans are performed when doing a Ratio Method analysis, since the ratio errors in later time bins are larger than in a T-Method histogram. Figure 8.23 shows that choice of fit end time does not bias

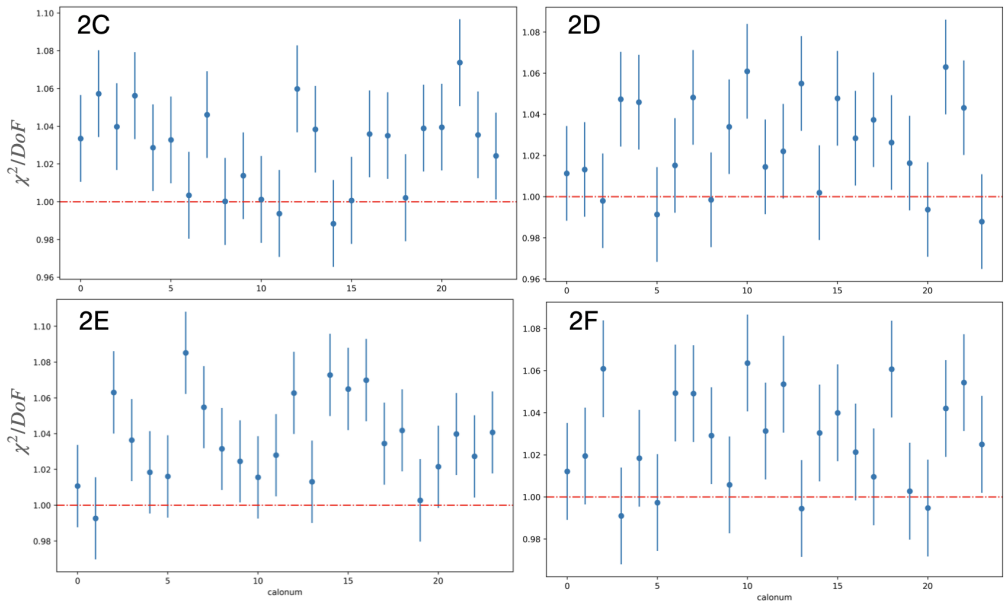


Figure 8.14: χ^2/DoF versus calorimeter number for datasets 2C, 2D, 2E, 2F. The red dashed line shows those calorimeter fits which are consistent with 1.

R. For datasets 2C, 2D, and 2E, R is consistent regardless of the energy threshold applied, shown in Figure 8.24. In the 2F dataset, R does drift away from the allowed statistical deviation, potentially indicating an incomplete energy calibration. Futhermore, the best fit value for R in the 2F dataset is farther from R in other datasets, which implies more investigation is required into the 2F dataset to develop confidence that data is not being modeled incorrectly.

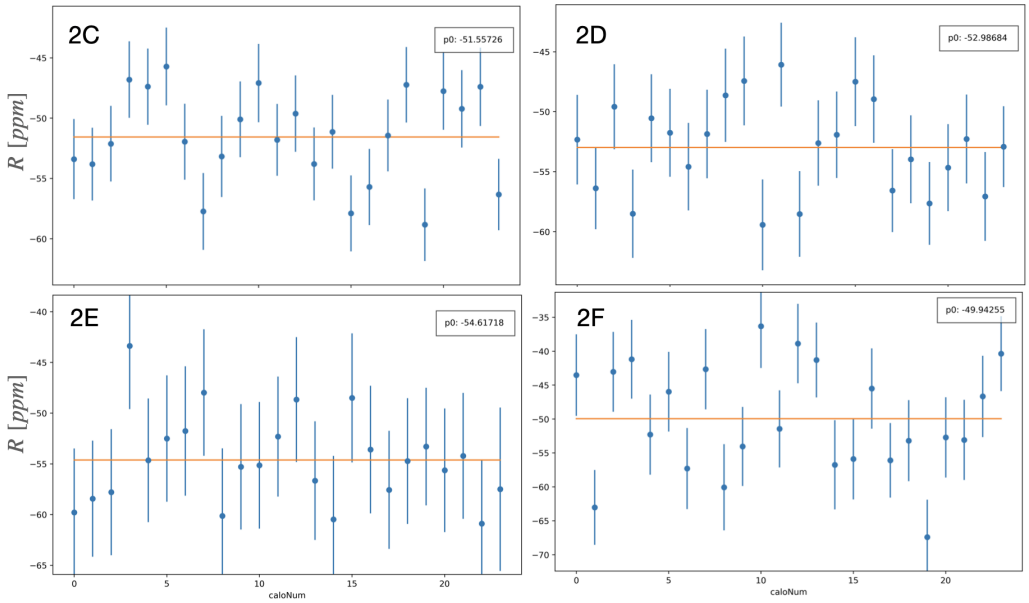


Figure 8.15: R versus calorimeter number for datasets 2C, 2D, 2E, 2F. A straight line fit was performed on the points, and the result is printed in the upper right as parameter p_0.

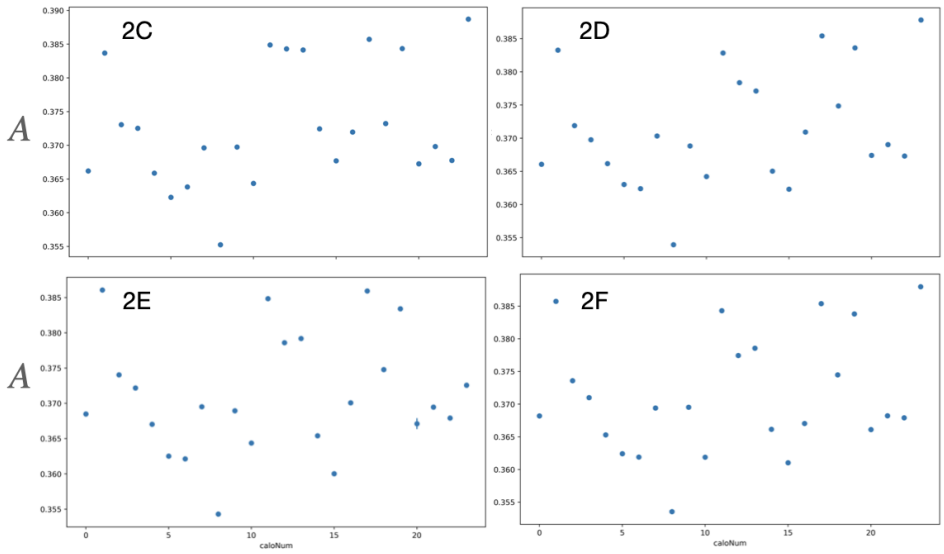


Figure 8.16: $g-2$ asymmetry versus calorimeter number for datasets 2C, 2D, 2E, 2F.

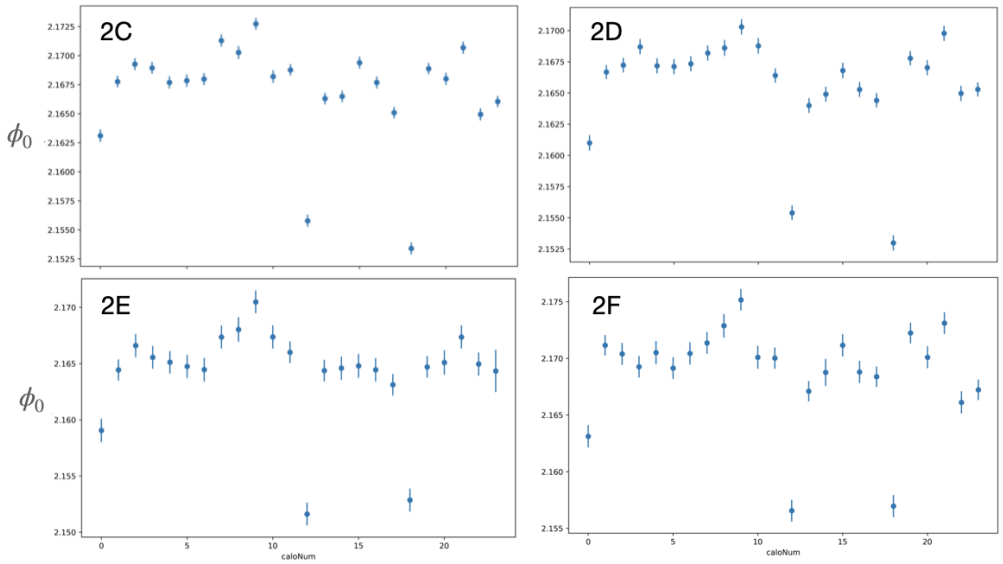


Figure 8.17: $g-2$ phase versus calorimeter number for datasets 2C, 2D, 2E, 2F.

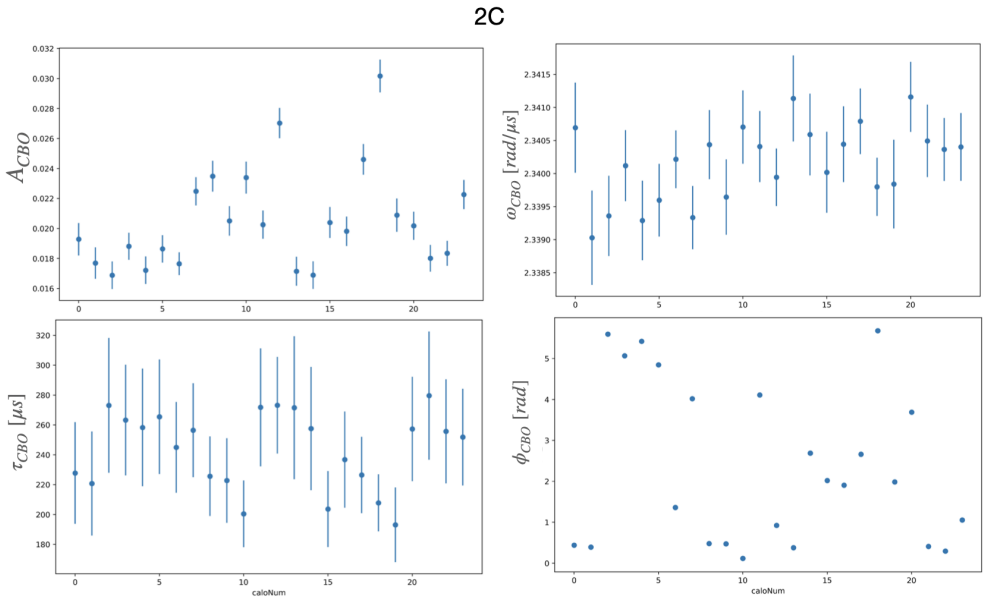


Figure 8.18: CBO parameters versus calorimeter number for the 2C dataset. These plots are typical of all datasets with minor variations.

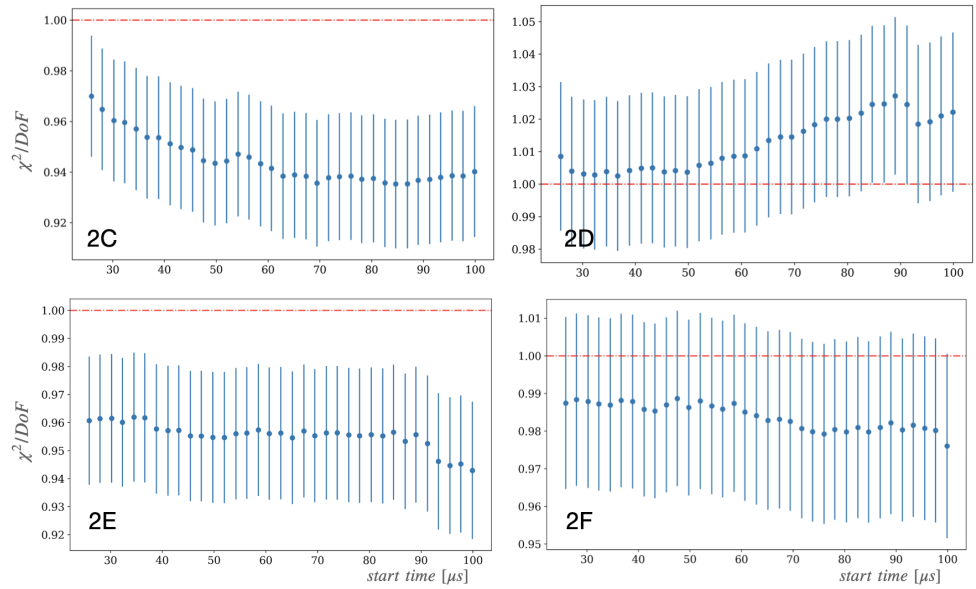


Figure 8.19: χ^2/DoF versus fit start time for datasets 2C, 2D, 2E, 2F. The red dashed line shows nearly all fits are consistent with, or below, 1.

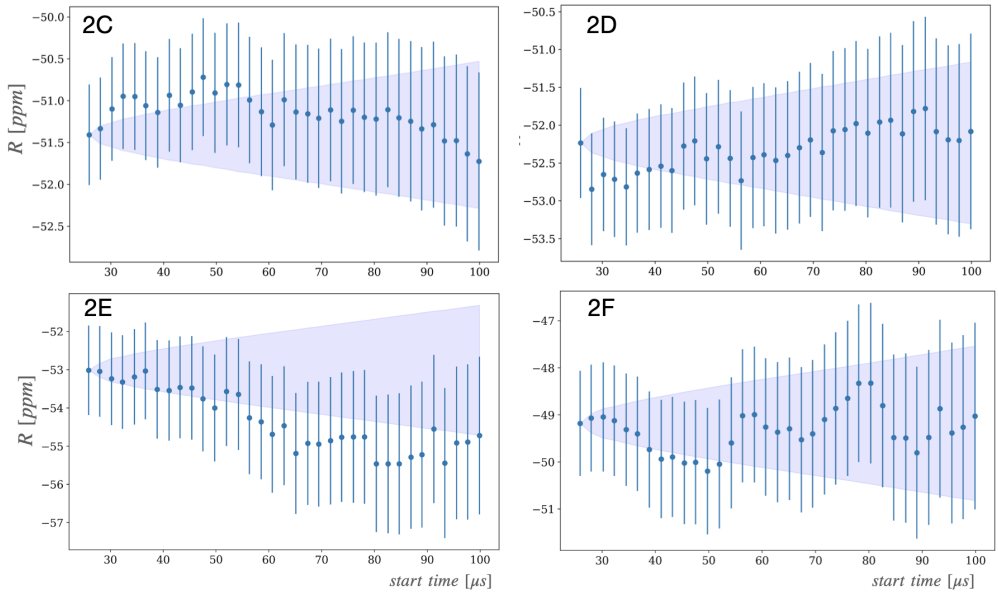


Figure 8.20: R versus fit start time for datasets 2C, 2D, 2E, 2F. The blue shaded band represents the 1σ statistically allowed deviation. In all datasets, the fit points lie within or around the statistical bands.

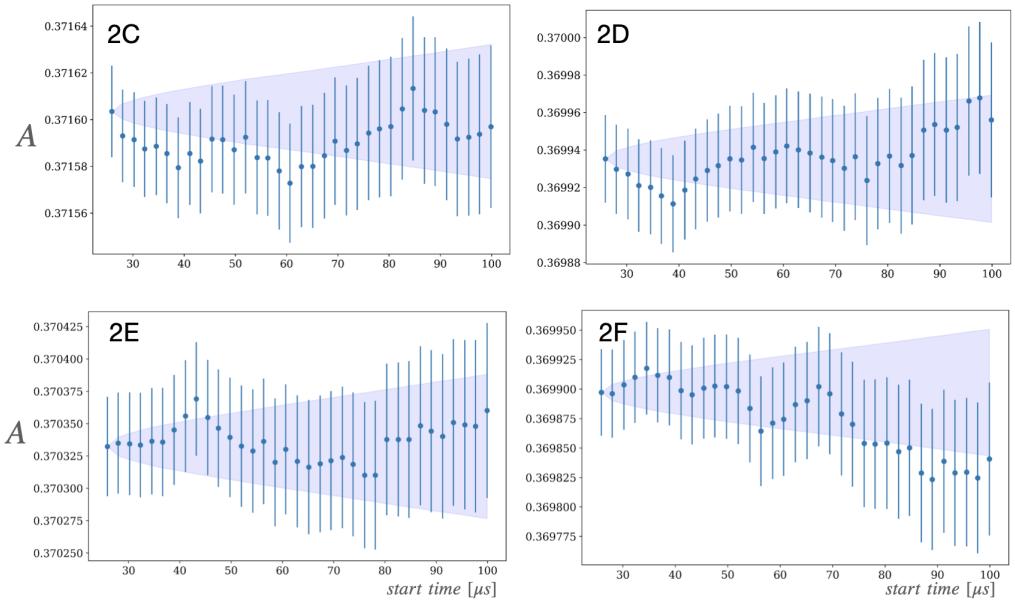


Figure 8.21: $g-2$ asymmetry versus fit start time for datasets 2C, 2D, 2E, 2F. The blue shaded band represents the 1σ statistically allowed deviation. In all datasets, the fit points lie within or around the statistical bands.

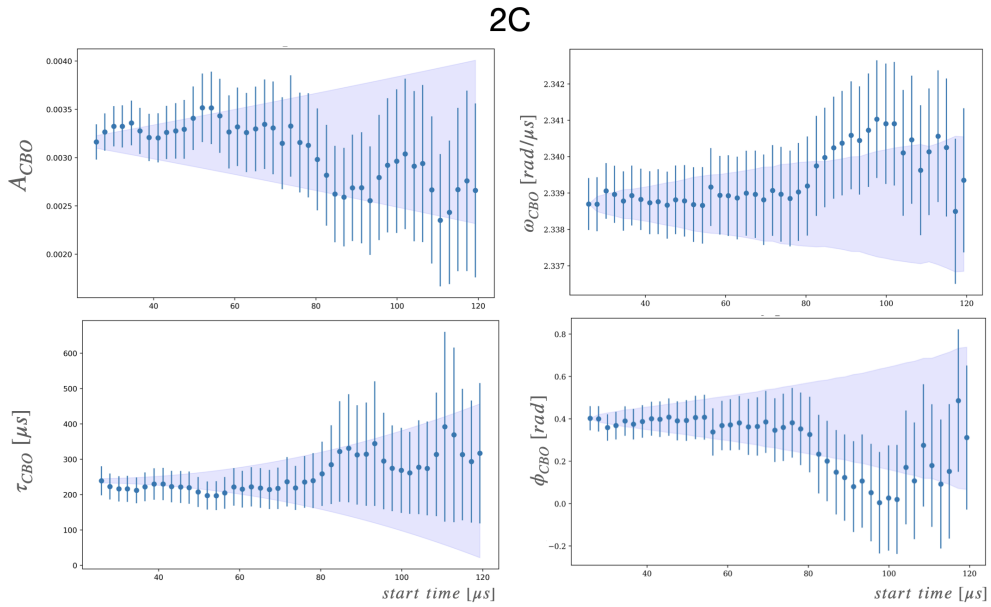


Figure 8.22: CBO parameters versus fit start time for the 2C dataset. These plots are typical of all datasets with minor variations. To check that the fluctuations between 90-100 μs for the CBO frequency and phase were not an indication of systematic drift, the fit start time scan was taken out to 120 μs

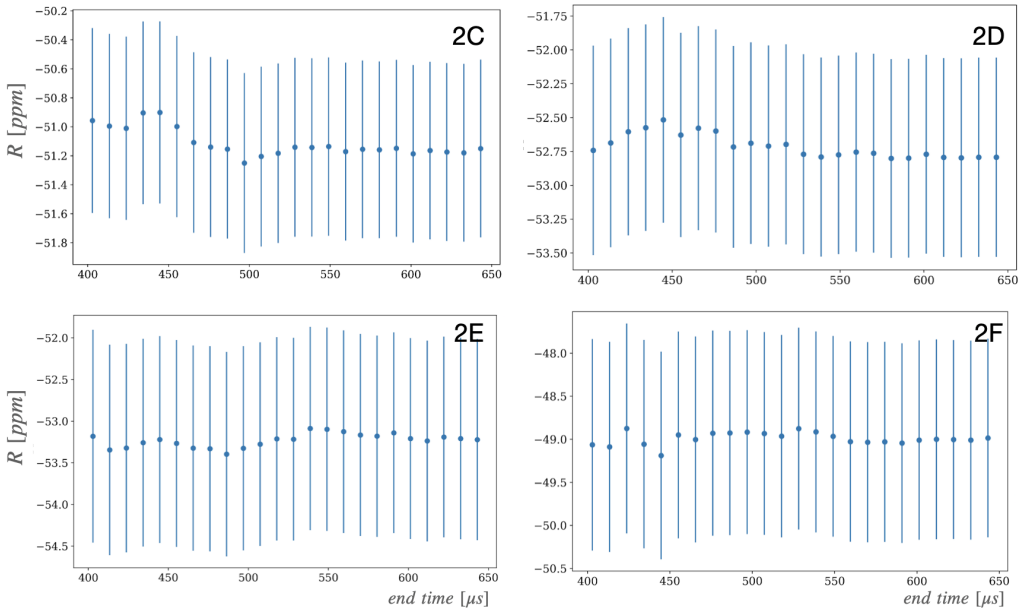


Figure 8.23: R versus fit end time for datasets 2C, 2D, 2E, 2F.

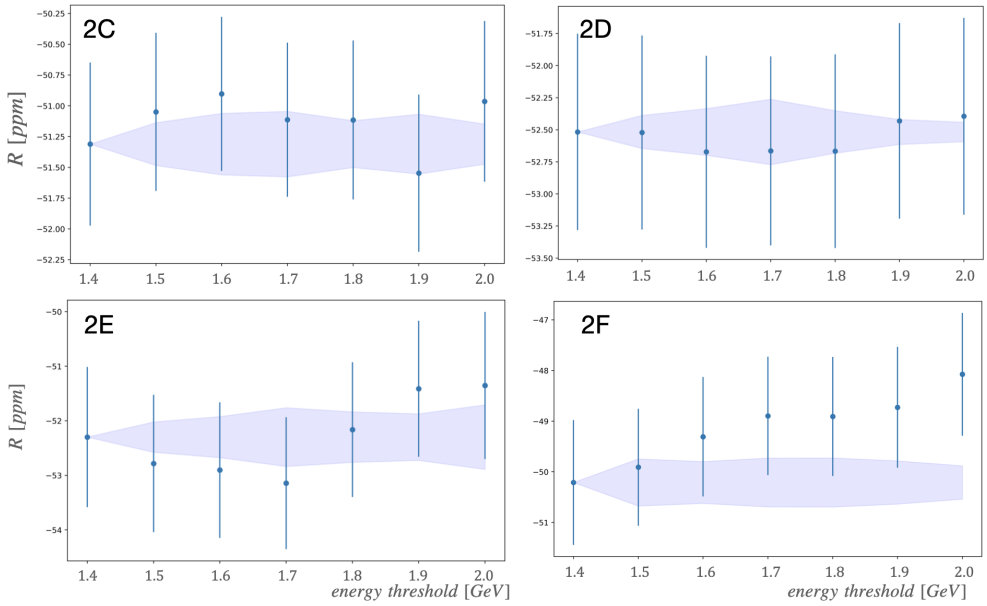


Figure 8.24: R versus energy threshold for datasets 2C, 2D, 2E, 2F. The blue shaded band represents the 1σ statistically allowed deviation. The 2F dataset exhibits some drift which requires further investigation.

8.5 Systematic Uncertainty Assessment

Run 1 finished with 56 ppb systematic uncertainty on ω_a [23]. The target for E989's final result is 70 ppb. Chapter 5 provided a description of the various uncertainties that can bias an ω_a measurement and several are calculated here for the 2C, 2D, 2E, and 2F datasets. The estimates given in this section should be understood as preliminary and not comprehensive. Many effects were left out of this calculation, and others will have to be re-calculated as new data quality cuts are applied, resulting in new datasets.

Most systematic effects arise from beam properties, which can vary across runs. Therefore, the magnitude of a systematic uncertainty, and even the technique for estimating it, can be change between datasets. At the same time, continued running provides more data from which to glean a cohesive understanding of the effects seen in the ω_a analysis. Beam simulations contribute to several systematic calculations, though no simulation results are presented here.

8.5.1 Pileup

The pileup correction method used in this analysis is the asymmetric shadow window method, described in Section 8.3, in which a pileup spectrum is constructed from the data by looking in time windows adjacent to trigger pulses for so-called shadow pulses. The time and energy models used in the pileup construction are

$$\begin{aligned} E_D &= C(E_1 + E_2) \\ t_D &= t_1 + t_G/2 \end{aligned} \tag{8.22}$$

where E_1 and t_1 are the energy and time of the trigger pulse, E_2 is the energy of the shadow pulse, t_G is the gaptime, and C is a calibration constant. The pileup spectrum is created by subtracting singlets from doublets. Afterwards this pileup spectrum is subtracted from the positron spectrum.

Systematic uncertainties arise from uncertainties in the pileup correction amplitude, as well as the time and energy models used. There are also a few systematic effects that do not manifest through the particular model described above but nevertheless are present in the data and should be estimated. Triple pileup, which occurs at a rate significantly less than double pileup, is not included in this correction, but is present in the data and therefore can introduce a systematic uncertainty as well. We can also estimate the systematic uncertainty that arises from unseen pileup, which is pileup that results from pulses below the detector energy threshold (approximately 50 MeV) combining with higher energy pulses.

Amplitude

Assuming the shape of the pileup correction matches reality, we can scale the amplitude by a multiplier to ensure the subtraction is not over or underestimating the pileup. The uncertainty due to this multiplier is evaluated by scanning over multipliers in the from 0.0 to 2.0, where 1.0 is the nominal value. At each point in the scan, the data is fit to extract R's sensitivity to the multiplier. A straight line was fit to the resulting plot and the slope was taken as dR/dP_m.

Customarily, the uncertainty on the multiplier is determined from the width of the parabola formed by the χ^2 versus R plot. The amount of pileup in the data is relatively small to begin with, and the Ratio construction reduces the fit's sensitivity to pileup, so there was no clear parabolic shape in the χ^2 versus P_m plot. Instead, the uncertainty on the amplitude was determined by analyzing the ratio of the cluster energy spectrum to the pileup energy spectrum. In the doublet energy range, the ratio of cluster energy

Pileup Amplitude Systematic Uncertainty			
Dataset	dR/dP_m [ppb]	σ_{P_m}	δR [ppb]
2C	57	0.05	3.9
2D	50	0.03	3.4
2E	45	0.06	1.0
2F	68	0.12	2.2

Table 8.6: Systematic uncertainty due to the pileup amplitude in the Ratio Method. The right-most column gives the systematic uncertainty on R.

to constructed pileup energy should be 1. The ratio was fit with a straight line and the deviation of the y-intercept was taken to be the error in the pileup amplitude, as shown in Figure 8.27. The systematic uncertainty on R due to the pileup amplitude was the product of the sensitvity dR/dP_m and the uncertainty on P_m. Results are given for all datasets in Table 8.5.

Energy Model

Pileup energy is constructed as the sum of the energies of the two singlets, as shown in Equation 8.22. Nominally, the scaling factor C is set to 1. Simulations performed using ReconEast clusters show that the ratio of pileup energy to the sum of the energies of the singlets is centered at 1, as shown in Figure 8.27. In these simulations, two positrons were fired at a calorimeter. When pileup occured, the reconstruction provided the true energy of the pileup cluster which was compared to the pileup energy derived from the energy model $E_1 + E_2$. This study also showed that at most the quantities E_{pileup} and $(E_1 + E_2)$ differed by 1% for energy sums above 1.7 GeV. Pileup events below 1.7 GeV showed more spread in the relative energies between doublets and singlet sums, however, these events are irrelevant as only clusters above 1.7 GeV enter the time histogram for ω_a extraction.

The systematic uncertainty due to choice of energy scaling was then calculated as the maximum change in R when applying a $\pm 1\%$ scale factor to the doublet energy. This amounts to setting $C = 0.99$ and $C = 1.01$ and taking ΔR from the subsequent fits. Results are listed in Table **??**.

Energy Scaling Systematic Uncertainty	
Dataset	δR [ppb]
2C	7.8
2D	6.9
2E	12.0
2F	4.4

Table 8.7: Systematic uncertainty due to choice of energy scaling the doublet energy model.

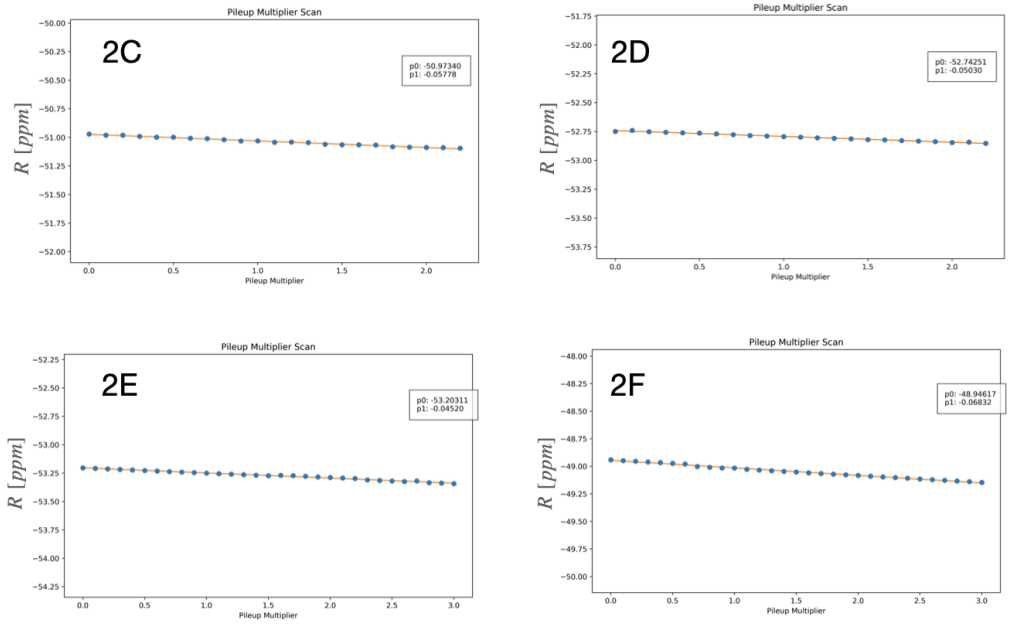


Figure 8.25: Pileup multiplier versus R for the 2C, 2D, 2E, and 2F datasets. The slope provides the sensitivty of R to the pileup multiplier.

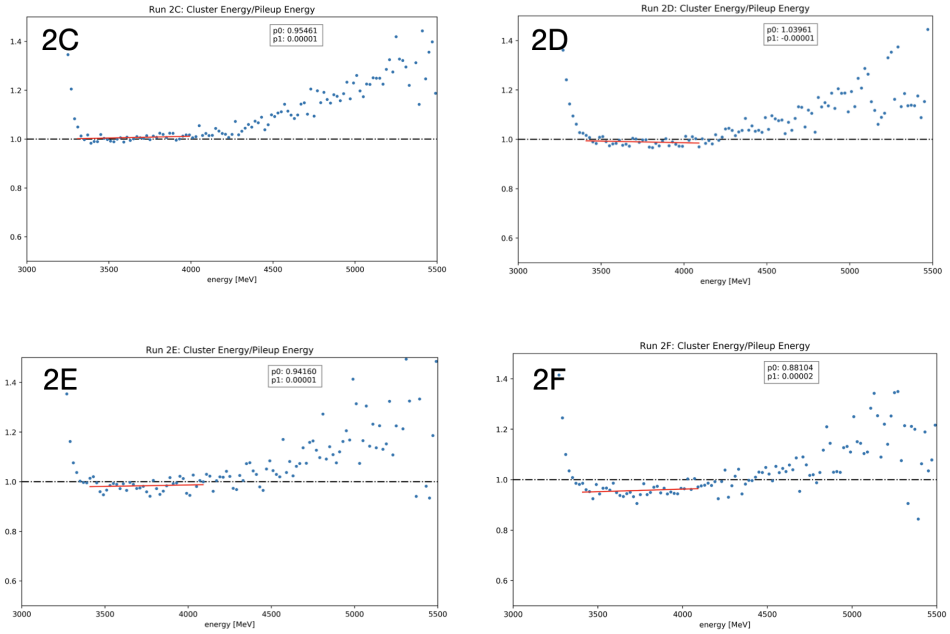


Figure 8.26: Cluster energy divide by pileup energy, using nominal $P_m = 1$. When pileup is corrected constructed, the ratio of cluster energy over pileup energy is 1 in the doublet energy range ($\sim$3.1-4 GeV). The deviation from 1 is determined by fitting a straight line to the doublet energy region and taking the y-intercept. The position of the red fit line relative to $y = 1$ shows how much the pileup is over- or under-inflated by the uncertainty in the pileup multipler.

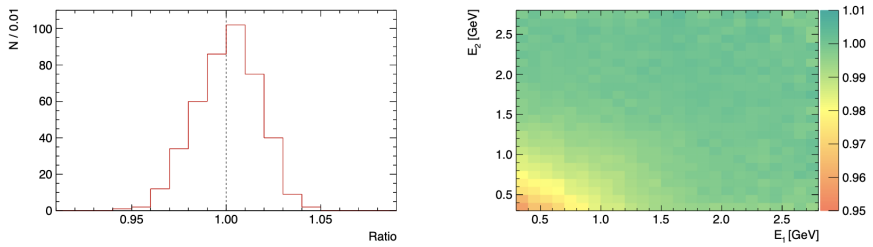


Figure 8.27: Results from simulations performed by D. Sweigart. Left: The ratio of pileup (doublet) energy to the sum of the two singlets for two positrons each with energy 2 GeV. Right: The average ratio of the pileup energy to the sum of the two singlets as a function of singlet energies. Figures reproduced from Reference [**?**].

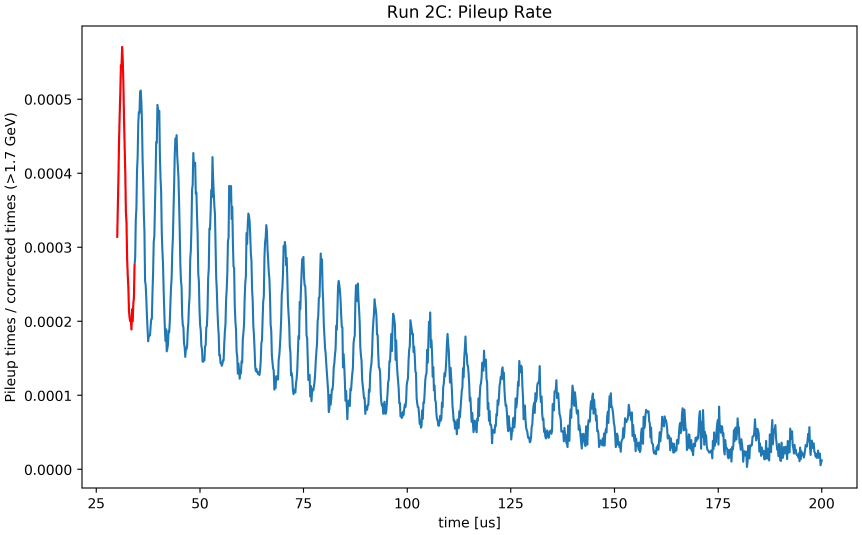


Figure 8.28: Rate of double pileup, taken as the ratio of the pileup time spectra over the pileup-corrected time spectra for clusters with energies above 1.7 GeV. The average rate is taken from the part of the spectrum highlighted in red, which represents the first T_a after fitting begins. Even at early times, the pileup rate is low due to robust detector performance and pulse separation techniques in the reconstruction. Data from the 2C dataset.

Triple Pileup Systematic Uncertainty						
	Pileup Rate ($\times 10^{-4}$)		R [ppm]			
Dataset	Average	Max	with Pileup Corr	without Pileup Corr	ΔR [ppb]	δR [ppb]
2C	3.50	5.70	-51.17	-51.167	3	0.001
2D	3.36	5.69	-52.795	-52.741	54	0.02
2E	3.27	5.36	-53.25	-53.204	46	0.015
2F	3.24	5.57	-49.016	-48.96	20	0.006

Table 8.8: Systematic uncertainty due to exclusion of triple pileup in the pileup correction. The average and maximum pileup rates are taken from the rate of doublet pileup during the first $g-2$ period of the fit. R is measured with and without the subtraction of pileup from the time histograms in the Ratio Method. The systematic uncertainty is the product of the maximum pileup rate and ΔR, and is listed in the final column.

Triple Pileup Estimation

Triple pileup refers to events where three positrons hit the calorimeter too close in space in time to be resolved individually. Triples are most visible in the energy spectrum as residual events above ~6 GeV and can be responsible for imperfect construction in doubles regime (< 6 GeV) as well, shown in Figure 5.7. Triple pileup is not constructed during the pileup correction in this analysis so it introduces a systematic uncertainty. This systematic uncertainty is estimated by multiplying the rate of triple pileup by the difference in R with and without pileup subtraction. The rate of triples is approximated by the rate of doubles during the first $g-2$ period in the fit, drawn in Figure 8.28. As the probability of three positrons piling up is smaller than the probability of two positrons piling up, using the rate of double pileup assumes a higher level of triple pileup than is likely present in the data. The systematic uncertainty estimations that result from this approach are conservative, and even more so when considering the fact that the rate drops throughout the fill. Table **??** summarizes the results of the triple pileup systematic uncertainty estimation.

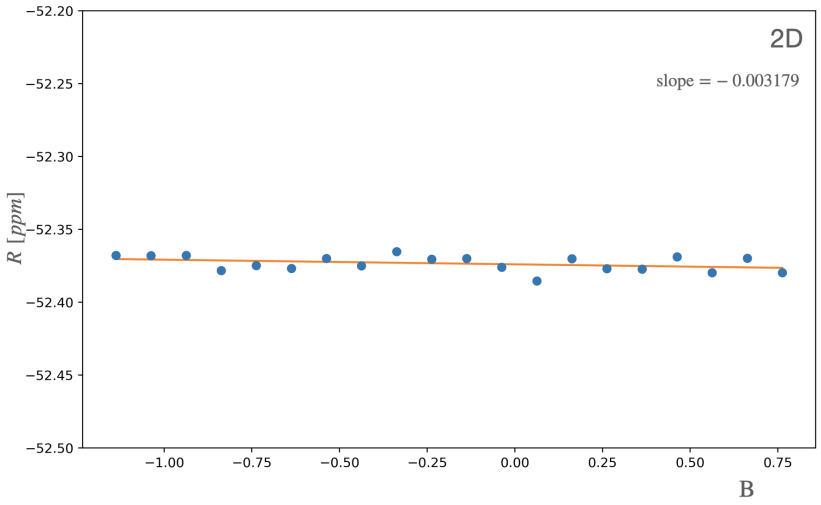


Figure 8.29: The CBO decoherence parameter, B, is fixed to different values and R is taken from the resulting fits. The slope of the fittes line (orange) gives the sensitivity of R to B. Data is from the 2D dataset.

CBO Envelope Constant from Fit			
Dataset	B (Ratio Method)	B (T-Method)	dR/dB [ppm]
2C	-0.11634 ± 0.42259	0.22023 ± 0.1569	0.003919
2D	-0.061334 ± 0.45577	-0.13734 ± 0.20034	-0.003179
2E	0.29809 ± 1.7202	-0.11535 ± 0.33456	0.004669
2F	-0.27132 ± 0.48128	-0.10139 ± 0.34491	0.003174

Table 8.9: The parameter B was allowed to float in the T-Method and Ratio fits. The fit returned small values with large errors for all datasets. The sensitivity of R to B for each dataset was calculated by scanning over values of B in Ratio Method fits and extracting the slope.

8.5.2 Coherent Betatron Oscillations

Assuming that the beam dynamics models used in the fit function are correct, CBO should not bias ω_a. The CBO model consists of a decoherence component and a frequency component, composed as an exponentially decaying cosine with a constant frequency. The decoherence envelope can be evaluated by including a floating parameter B to the envelope,

$$e^{t/\tau_{CBO}} \rightarrow e^{t/\tau_{CBO}} + B \tag{8.23}$$

and observing the change in R due to this new parameter. Since the Ratio Method is less sensitive to CBO, both the T-Method and R-Method fit results are shown for B. The errors are relatively large but the values are consistent between the T-Method and the Ratio Method. The parameter B did not change the value of ω_{CBO} in the fits, though in general, it did cause the errors on τ_{CBO} to increase by roughly a factor of 2. The sensitivity of R to the choice of B was taken by scanning over values of B and taking dR/dB from the results. An example is shown in Figure 8.29. The best fit value of B and dR/dB for each dataset are shown in **??**. The systematic uncertainty due to the decoherence envelope is the product of the sensitivity dR/dB and the uncertainty on B.

Future studies could test other decoherence models, such as those with a polynomial component, as in

$$e^{t/\tau_{CBO}} \cdot (B_0 + B_1 t + B_2 t^2 + ...) \tag{8.24}$$

So far there is no evidence that including a polynominal to the CBO decoherence envelope changes R or the fit significantly. Simulations have shown that vertical waist oscillations could reasonably recohere, whereby the fit model would be incorrect which allow for the possibility of bias to the $g-2$ phase. It is possible that the CBO could recohere after some time, though with a longer lifetime we could reasonably expect the effect to only emerge later in a fill.

As for the frequency model, the start time scans show ω_{CBO} does meander slightly from the best fit value. Though tracker measurements have confirmed confirmed that the CBO is constant, these small deviations in the start time scans require further investigation. In Run 1, ω_{CBO} changed by about 0.2 rad/μs between fit start and fit end. If this data had been treated with a fixed frequency modeled, the bias on R would have been around 100 ppb. So far there is no indication of such a large effect in Run 2 but at minimum, CBO could change by $\Delta\omega = 1.7 \times 10^{-3}$ rad/μs due to instability in the quad HV pulsers [59]. Tracking analysis shows that other frequency models are not necessarily more effective at matching the data than the

constant frequency model used here and perhaps not sensitive to an effect at this level [60]. Fixing ω_{CBO} to $\omega_{CBO} \pm \frac{\Delta\omega}{2}$ and refitting the data, corresponds to a change in R of 2 ppb, 5 ppb, 2 ppb, and 1 ppb for the 2C, 2D, 2E, and 2F datasets, respectively. The systematic uncertainty due to the CBO decoherence envelope and constant frequency model are summarized in Table **??**.

Because the betatron oscillations in E989 are complicated by non-ideal circumstances, it is important to use a variety of technques to resolve what is really occuring in the beam. The fit models used in ω_a analyses approximate the number of moments in the muon distribution to be less than three, for example. This analysis has also not considered how beat frequencies or aliased frequencies might appear in the data if some contributing frequencies are a function of time-in-fill.

CBO Model Systematic Uncertainty			
Dataset	δR_{env}	δR_{freq}	δR_{total}
2C	0.16	2	2.0
2D	0.14	5	5.0
2E	0.80	2	2.2
2F	0.15	1	1.0

Table 8.10: The systematic uncertainty due to the CBO model. The uncertainties on B come from the fits listed in Table **??**. The second column gives the systematic uncertainty due to the decoherence envelope, the third column gives the systematic uncertainty due to the constant frequency model, and the fourth column gives the quadrature sum for each dataset. All values are in ppb.

8.5.3 Muon Losses

The Ratio Method is too insensitive to K to converge on a value in the fit so the value used in the model is fixed at the value determined from the T-Method fit. To determine the systematic uncertainty due to this procedure of fixing K, the value of K was scanned over in the fits and the sensitivity dR/dK was taken from the scans. An example is shown in Figure 8.31. The uncertainty on K itself was taken from the T-Method fit result. The systematic uncertainty due to the K was calculated as the product of the sensitivity dR/dK and the uncertainty on K. Results are shown in Table **??**.

8.5.4 Ratio Construction

Since the Ratio construction uses T_a as an input, there is potential for bias. The sensitivity to the ratio construction parameter was found by scanning over shifts in T_a and fitting for R. A scan over 2C data found a 1.3 ppb shift in R per 1 ppm shift in T_a. Since T_a is known to less than 1 ppm, a conservative estimate for the systematic uncertainty is 1.3 ppb. It is safe to assume that all datasets will behave in the same manner with respect to the ratio construction. Therefore, the uncertainty is conservatively taken to be 2 ppb for all datastets.

8.5.5 Systematic Uncertainty Summary

During Run 1, the benchmark for whether a systematic uncertainty is significant is 10 ppb. Most of the uncertainties estimated here are less than 10 ppb. However, several crucial systematic uncertainties were not

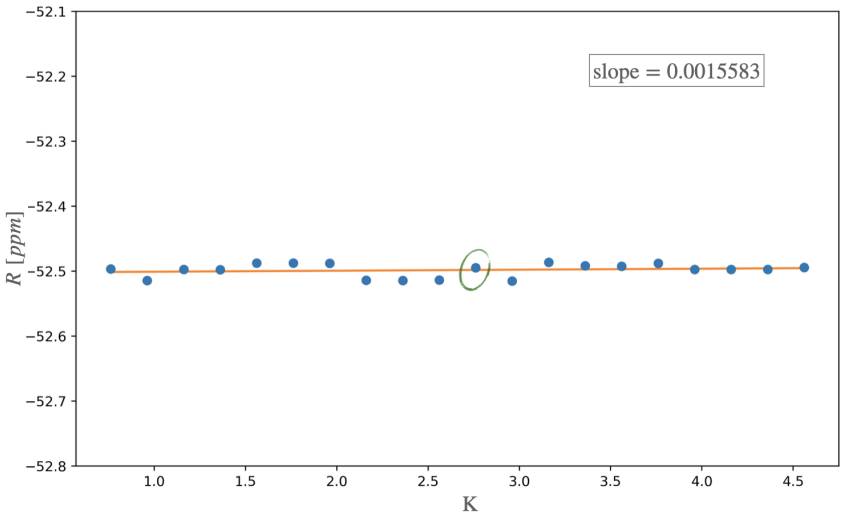


Figure 8.30: The muon loss parameter, K, is fixed to different values and R is taken from the resulting fits. The slope of the fittes line (orange) gives the sensitivity of R to K. Data is from the 2D dataset. The point circled in green is the nominal K value.

Fixed Muon Loss Parameter Systematic Uncertainty			
Dataset	σ_K	dK/dR	δR [ppb]
2C	0.3673	0.0001142	<0.1
2D	0.3962	0.001558	0.6
2E	0.7038	0.001501	0.1
2F	0.7585	0.00085	<0.1

Table 8.11: Systematic uncertainty due to fixing the lost muon parameter in the Ratio Method. The uncertainty on K and sensitivty to K are in units of ppm and 1/ppm, respectively.

calculated, such as those from gain variations, the time model used in the pileup construction, and unseen pileup. In Run 1 the largest systematic uncertainties were from gain or CBO. Since the CBO is behaving as expected in Run 2, it is likely that more uncertainty will arise from gain variations than other sources in Run 2. A complete Ratio Method analysis would also include a study of the random splitting of data into four groups to determine if the choice of random seed could bias R. The uncertainties estimated in this section are summarized in Table **??** for each of the four datasets.

ω_a **Systematic Errors in Run 2**				
Source	2C	2D	2E	2F
Pileup	8.72	7.69	12.04	4.92
CBO	2.00	5.00	2.20	1.00
Lost Muons	0.1	0.06	0.1	0.1
Ratio construction	2.00	2.00	2.00	2.00
Quadrature Sum	9.1	9.3	12.4	5.4

Table 8.12: Summary of the uncertainties on ω_a estimated in this chapter. Many other uncertainties remain to be calculated. The value for the total uncertainty presented here is a preliminary accounting of some of the most important sources of uncertainty. All values in the table are in ppb. For all four datasets combined, the total uncertainty for the effects considered in this section is estimated at 20 ppb.

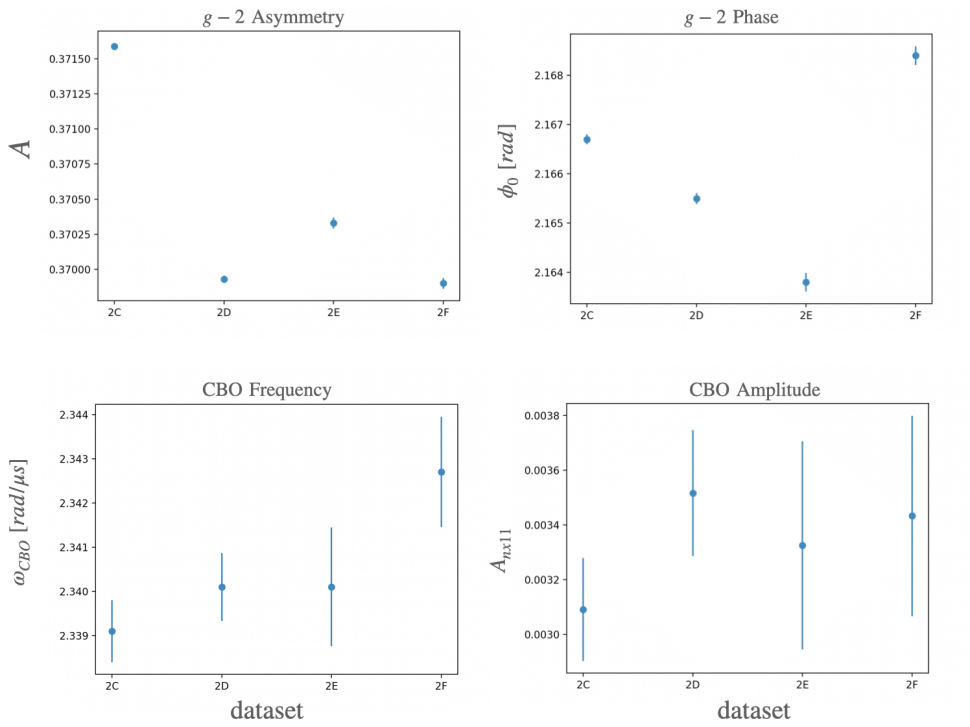


Figure 8.31: Best fit parameter values for the 2C, 2D, 2E, and 2F datasets. From top left, clockwise: asymmetry, g-2 phase, CBO amplitude, and CBO frequency. In choosing which datasets to combine, consistentcy among fit parameters values is considered.

8.6 Combining Datasets

In Run 1, conditions varied between datasets such that combining their results was nontrivial. Similarly in Run 2, there is evidence that all the data is not quite equivalent. Figure 8.31 shows how key parameters vary across datasets. Regardless, considering the results of a combination of datasets is worthwhile. Since the 2D and 2E datasets have fit results with the most in common, their combination was fit using the procedure for the individual datasets. Results in Table 8.7 show that the combined dataset, refered to as 2D+2E, is consistent with both separate datasets and unsurprisingly provides an improved statistical precision on R.

The main difference between the 2D and 2E datasets are their sizes. When added together, the 2E dataset accounts for a quarter of the combined dataset. Therefore, any features seen in 2D are expected to dominate in the combined dataset. For example, as the 2D dataset is larger, the combined lost muon spectrum more closely resembles the 2D lost muon spectrum.

To combine the datasets, the same histograms were used for the main analysis were added together before subtracting pileup and constructing the ratio. Each constituent n_i in the ratio and corresponding pileup histograms from the 2D dataset were summed with the matching histograms in the 2E dataset. More explicitly,

$$\begin{aligned} n_{i,(2D+2E)'} &= n_{i,2D'} + n_{i,2E'} \\ PU_{i,(2D+2E)} &= PU_{i,(2D)} + PU_{i,(2E)} \end{aligned} \tag{8.25}$$

where a ' in the subscript indicates histograms without pileup subtraction. Carrying out the pileup subtraction

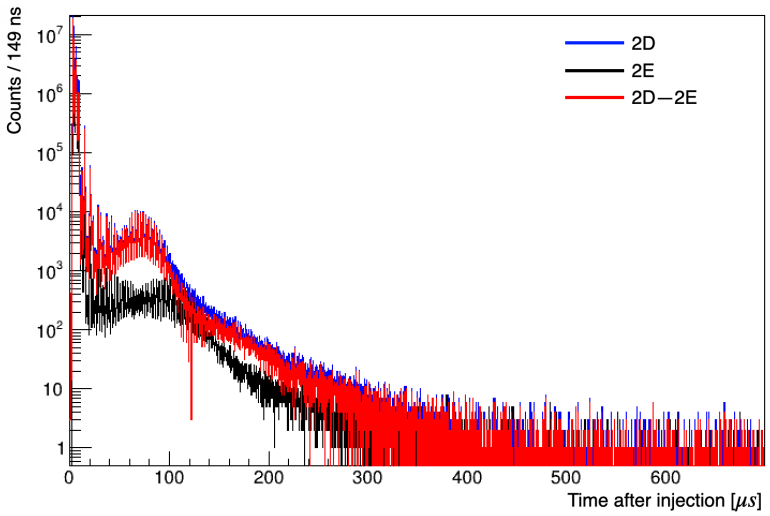


Figure 8.32: The lost muons' time distribution, $L(t)$, from the 2D and 2E datasets. Their difference is drawn in red, and is practically indistinguishable from the 2D dataset's $L(t)$. When fitting 2D and 2E together, the lost muon time distribution from 2D will dominate.

then proceeds as normal,

$$n_{i,(2D+2E)} = n_{i,(2D+2E)'} - PU_{i,(2D+2E)} \tag{8.26}$$

and the ratio is also formed in the same manner as shown in Equations 8.6-8.8. The resulting histogram R_{2D+2E} is fit with the 21 parameter model keeping K fixed at the value from the corresponding T-Method fit result. The lost muon time spectra $L(t)$ are summed in the same way as in Equation 8.24, and incorporated into $\Lambda(t)$ in the fit model as in Equation 8.18. Since the combined datasets are statistically independent, bin uncertainties are treated the same as in the individual dataset fits.

A brief overview of the success of this procedure is shown in the following tables and figures. Mainly, the combined dataset fit returns an R consistent with the individual datasets. No peaks above noise appear in the fit residuals' FFT and all fit parameters are steady with changing fit start time. No abnormal behavior is observed in this cursory exercise, though any such effects will be washed out and more difficult to spot in a larger dataset. The different time distributions for lost muons in the individual datasets are a reminder that these datasets come from different muon beams. These differences could either average out or exacerbate unknown biases on ω_a, and more study will be required to determine which option is occuring.

If future Runs are more stable throughout, the analysis will benefit from the full samples, rather than the smaller piecemeal samples that have to be averaged together after the fact. A fuller dataset would provide improved sensitivity to effects that are hidden in the smaller statistics of individual production datasets. Determining the compatibility of different datasets and even Runs is somewhat uncharted territory at this moment in E989 but it is likely that the lessons of Run 1 and Run 2 will assist in this endeavor.

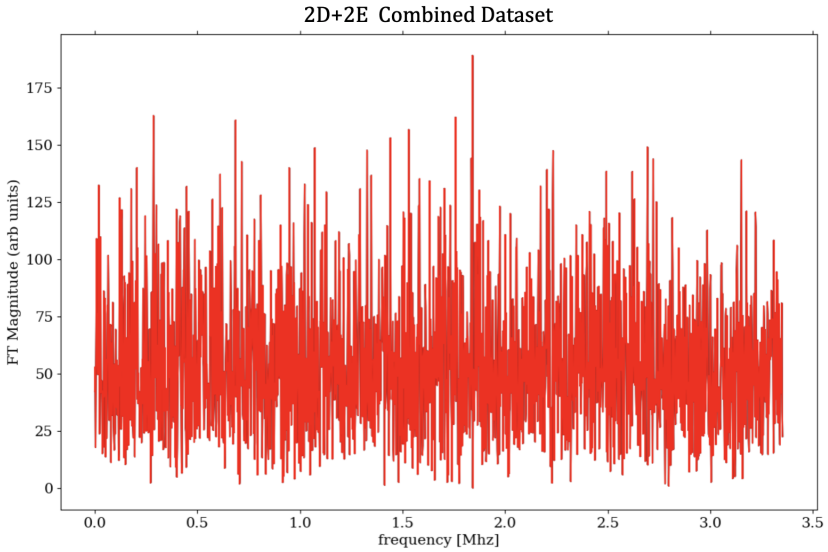


Figure 8.33: The FFT of the fit residuals using the 21-parameter Ratio model on the combined 2D+2E dataset. There are no clear frequency peaks above the noise floor, suggesting that the model adequately describes the data.

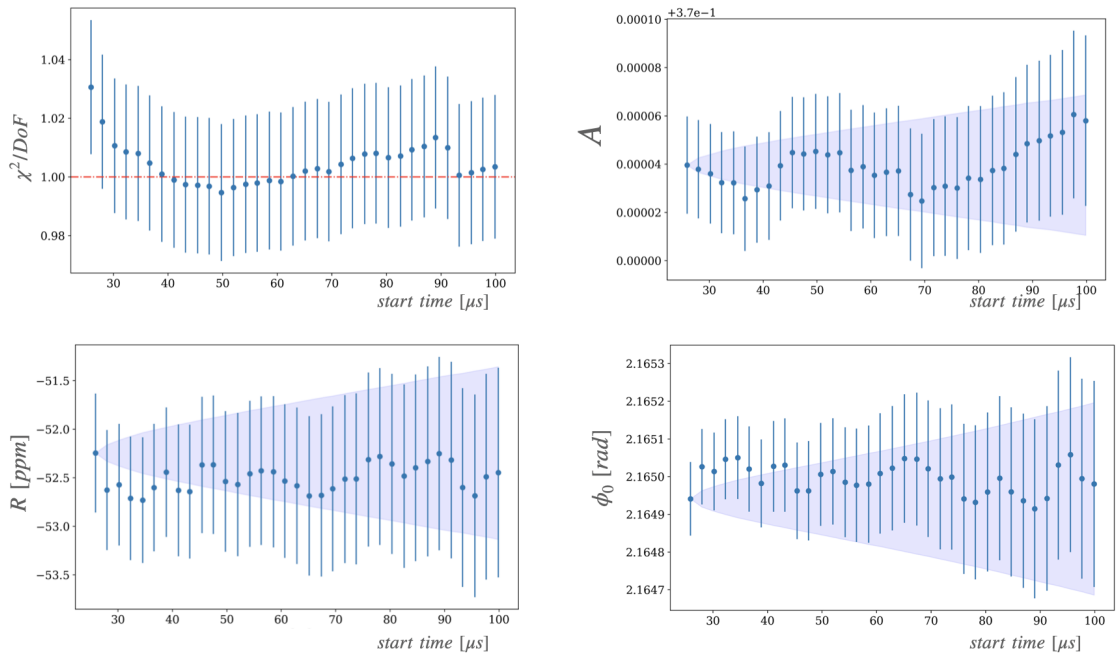


Figure 8.34: Fit start time scan using the 21-parameter Ratio model on the combined 2D+2E dataset. χ^2/DoF is consistent with 1 throughout. The most important fit parameters (R, A, ϕ_0) remain within or around the 1σ allowed statistical deviation (blue shaded bands), indicating that the model correctly captures the $g-2$ oscillation.

	2D	2E	2D+2E
χ^2/DoF	1.0021	0.9611	0.9950
p-value	0.4603	0.9561	0.5820
R [ppm]	-52.513 ± 0.7275	-53.24 ± 1.2066	-52.559 ± 0.6221
A	$0.36993 \pm 2.39 \times 10^{-5}$	$0.37033 \pm 3.98 \times 10^{-5}$	$0.3700 \pm 2.04 \times 10^{-5}$
ϕ_0 [rad]	2.1655 ± 0.00011969	2.1638 ± 0.00019856	02.165 ± 0.0001023

Table 8.13: Comparison of the main fit parameters from the combined 2D+2E dataset with the results of the fits from the individual datasets.

Chapter 9

Conclusion

The analysis presented here of the 2C, 2E, 2D, and 2F datasets is preliminary and ongoing. Figure 9.1 shows E989's data collection progress in terms of E821 datasets. With Run 3 now finished, E989 is about halfway through total data taking, though data analysis will follow behind as different problems and effects arise in the data which require careful study. Data quality filtering and production processing is still underway for Run 2, meaning much of the work shown here will have to be repeated as new cuts are made and updated calibration constants are applied. However, the Ratio Method was shown to be an effective complement to the archetypal T-Method analysis, returning consistent measurements for R with improved precision.

A continuation of the work presented here would focus on evaluating systematics due to gain drift, the pileup time model, and time randomization during histogramming. Independent analysis groups within the collaboration are working on estimating differential decay, pitch, and electric field corrections, so these are not necessarily the responsibility of an ω_a analyzer. Next steps in the work shown here also include figuring out when it is appropriate to combine datasets and how to do so without rendering the fit model inaccurate. Though all datasets returned reasonable results, some questionable behavior was observed in the 2F dataset energy scan, indicating a possible systematic effect. An advanced analysis will continue to look for effects such as these and identify the source so that any unwanted biases to ω_a can be corrected.

The total statistical uncertainty on ω_a from the Run 2 data analyzed here is 418 ppb and the minimum systematic uncertainty is estimated at $\sim$20 ppb. Regarding the magnetic field measurement, the target systematic error on ω_p is 70 ppb [24]. Using these values, the uncertainty on a_μ is bounded below by

$$\sigma_{a_\mu} \approx \sqrt{(20\,\text{ppb})^2 + (418\,\text{ppb})^2 + (70\,\text{ppb})^2} = 424\,\text{ppb} \tag{9.1}$$

for the Run 2 data analyzed in this dissertation. This is a very rough approximation, neverthless, it is useful for the purpose of comparing to Run 1 which had a total σ_{a_μ} of 460 ppb.

So far, E989 has confirmed the discrepancy between theoretical prediction and experimental measurement of a_μ, hinting at the exciting possibility of physics beyond the Standard Model. Since the data analyzed here remains blinded, it is unknown whether Run 2 data will confirm or deny the existing discrepancy. In any case, the data analyzed in here presents a 16 ppb improvement in the statistical uncertainity on ω_a which remains the dominant source of error. In the coming months, a full analysis of Run 2 data should emerge from the combination of multiple analysis groups, adding another chapter to the story of a_μ.

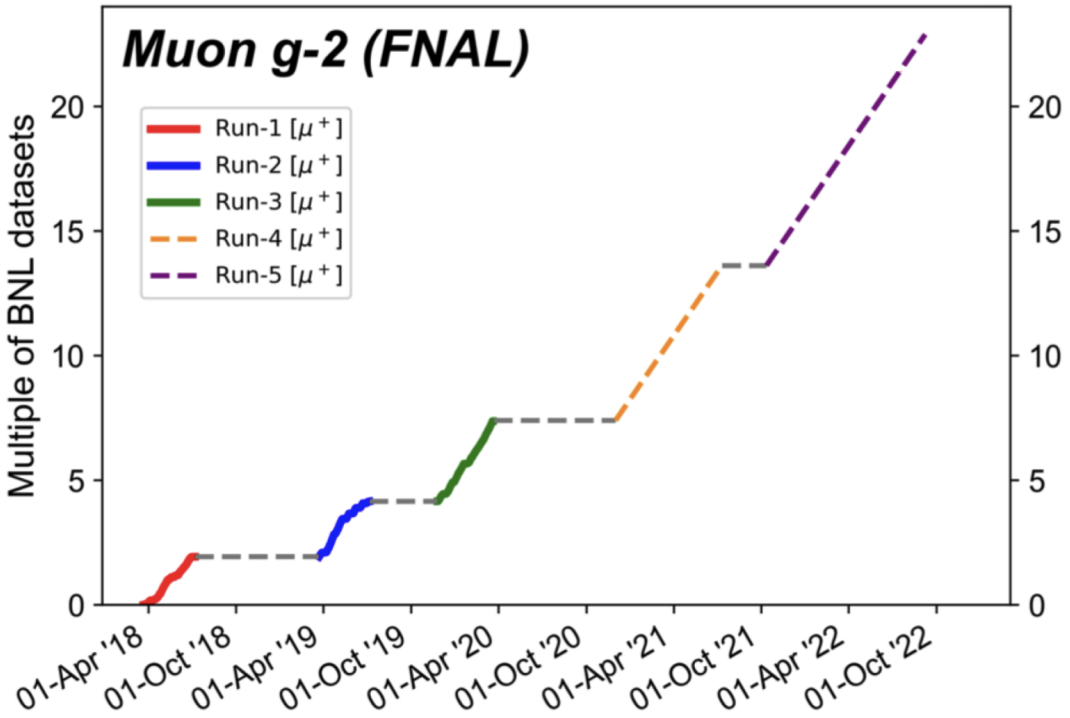


Figure 9.1: Timeline of E989 runs. Runs 1-3 have been completed, with analysis currently underway on Runs 2 and 3. The amount of E989 data is quantified in terms of the final E821 dataset size. Data quality cuts have not been applied here, so the actual amount of data used to perform the ω_a analysis is somewhat reduced.

Appendix A

Ratio Method

The Ratio Method was first concieved and implemented during E821 [53]. The derivation presented here is consistent with the presentation of the Ratio Method in previous E821 and E989 analyses [61, 32].

A.1 Ratio function derivation

Consider a function that describes the positron time spectrum, N(t). Before forming the ratio, the positron data is randomly split into four equal subsets and two of these subsets are shifted in time by half a $g-2$ period. The resulting histograms are described by

$$\begin{aligned} n_1(t) &= \frac{1}{4}N(t+T_a/2) \\ n_2(t) &= \frac{1}{4}N(t-T_a/2) \\ n_3(t) &= \frac{1}{4}N(t) \\ n_4(t) &= \frac{1}{4}N(t) \end{aligned} \tag{A.1}$$

where T_a is the $g-2$ period known a priori to high precision. Constructing the ratio then consists of combining $n_1 - n_4$ as

$$\begin{aligned} U(t) &= n_1(t) + n_2(t) \\ V(t) &= n_3(t) + n_4(t) \\ R(t) &= \frac{V(t)-U(t)}{V(t)+U(t)}. \end{aligned} \tag{A.2}$$

Plugging in the time spectra to R(t) gives

$$R(t) = \frac{2N(t) - N(t+T_a/2) - N(t-T_a/2)}{2N(t) + N(t+T_a/2) + N(t-T_a/2)}. \tag{A.3}$$

This is the general form of the ratio for any N(t). In the case of the five parameter function,

$$N(t) = N_0 e^{-t/\tau} \cdot Acos(\omega_a t + \phi) \tag{A.4}$$

the ratio construction produces a simplified fitting function, which follows from plugging in A.4 to A.3

and letting $\phi = 0$ for simplicity. R(t) becomes

$$R(t) = \frac{2N_0e^{-t\tau} \cdot Acos(\omega_a t) - N_0e^{-(t+T_a/2)\tau} \cdot Acos(\omega_a(t+T_a/2)) - N_0e^{-(t-T_a/2)\tau} \cdot Acos(\omega_a(t-T_a/2))}{2N_0e^{-t\tau} \cdot Acos(\omega_a t) + N_0e^{-(t+T_a/2)\tau} \cdot Acos(\omega_a(t+T_a/2)) + N_0e^{-(t-T_a/2)\tau} \cdot Acos(\omega_a(t-T_a/2))} \tag{A.5}$$

Common terms N_0 and $e^{-t/\tau}$divide out.

$$R(t) = \frac{2(1 + Acos(\omega_a t)) - e^{-T_a/2\tau}(1 + Acos(\omega_a t + \omega_a T_a/2)) - e^{T_a/2\tau}(1 + Acos(\omega_a t - \omega_a T_a/2))}{2(1 + Acos(\omega_a t)) + e^{-T_a/2\tau}(1 + Acos(\omega_a t + \omega_a T_a/2)) + e^{T_a/2\tau}(1 + Acos(\omega_a t - \omega_a T_a/2))} \tag{A.6}$$

The phase term $\omega_a T_a/2$ within the cosine functions turns out to be a small deviation from π. Recall that ω_a is what we measure while T_a is an estimate derived from a previous measurement of ω_a. If T_a and the the value of ω_a that we are measuring agree, then the phase is exactly π. In reality, there will be a small discrepancy $\mathcal{O}(10^{-5})$ between the estimate of T_a that we use in the formulation, and the true value $T_{a,true}$. This results in a phase slightly offset from π, which we can name δ. More precisely,

$$\delta = \pi \times (T_a - T_{a,true})/T_{a,true}. \tag{A.7}$$

By setting $\omega_a T/2 = \delta$ in equation A.6 and using the trig identity $cos(a \pm b) = cos(a)cos(b) \mp sin(a)sin(b)$, the cosine terms in $R(t)$ become

$$cos(\omega_a t \pm \delta) = cos(\omega_a t)cos(\delta) \mp sin(\omega_a t)sin\delta$$

Since $\delta << 1$, we can use $cos\delta = 1 - \delta^2$ and $sin\delta = \delta$ such that

$$cos(\omega_a t \pm \delta) \approx cos(\omega_a t)1 - \delta^2 \mp sin(\omega_a t)\delta \approx cos(\omega_a t)$$

Putting this back into R(t) gives

$$R(t) = \frac{2(1 + Acos(\omega_a t)) - e^{-T_a/2\tau}(1 + Acos(\omega_a t)) - e^{T_a/2\tau}(1 + Acos(\omega_a t))}{2(1 + Acos(\omega_a t)) + e^{-T_a/2\tau}(1 + Acos(\omega_a t)) + e^{T_a/2\tau}(1 + Acos(\omega_a t))} \tag{A.8}$$

The exponential terms can be rewritten in terms of the expansion

$$e^{T/2\tau} = 1 + \frac{T}{2\tau} + \frac{1}{2}\left(\frac{T}{2\tau}\right)^2 + \dots \tag{A.9}$$

Using this in Equation A.8 reduces the expression to

$$R \approx \frac{Acos(\omega_a t) - C(1 - Acos(\omega_a t))}{1 + C(1 - Acos(\omega_a t))} \tag{A.10}$$

where

$$C = \frac{1}{16}\left(\frac{T_a}{\tau}\right)^2 \approx 2.8 \times 10^{-4}. \tag{A.11}$$

Since C is small, the geometric series expansion: $1/(1 + x) = 1 - x + \dots$ can be used to manipulate the

denominator of Equation A.10:

$$R(t) \approx Acos(\omega_a t) - C(1 - Acos(\omega_a t)) \cdot (1 - C(1 - Acos(\omega t))) \approx Acos(\omega_a t) - C + CA^2 cos^2(\omega_a t) \quad \text{(A.12)}$$

The last term is omitted since it has a minimal effect on the fitted value of ω_a [62]. Finally, the model function for the ratio spectrum is

$$R(t) \approx Acos(\omega_a t) - C. \quad \text{(A.13)}$$

This is the 3 parameter ratio fit model. Many approximations are made in this derivation. Most of these can be avoided by changing the weighing of the histograms such that n_i look like

$$\begin{aligned} n_1(t) &= \frac{e^{T_a/2\tau}}{2 + e^{T_a/2\tau} + e^{-T_a/2\tau}} N(t + T_a/2) \\ n_2(t) &= \frac{e^{-T_a/2\tau}}{2 + e^{T_a/2\tau} + e^{-T_a/2\tau}} N(t - T_a/2) \\ n_3(t) &= \frac{1}{2 + e^{T_a/2\tau} + e^{-T_a/2\tau}} N(t) \\ n_4(t) &= \frac{1}{2 + e^{T_a/2\tau} + e^{-T_a/2\tau}} N(t). \end{aligned} \quad \text{(A.14)}$$

Using these histograms in the ratio formulation, the only approximation made is at $\mathcal{O}(10^{-10})$ and results in no C term in the final fit function R(t). This approach is used in Reference [32].

Returning to Equation A.3, consider a different time spectrum described by the 23 parameter function introduced in Section 8.1,

$$N(t) = Z(t) \cdot N_0 e^{-t/\tau} \cdot Acos(\omega_a t + \phi) \quad \text{(A.15)}$$

where Z(t) represents all the beam dynamics models (Equations 8.12-8.16) included in the fit model. The expression for the ratio in this case is

$$R(t) = \frac{2Z(t)N(t) - Z(t + T_a/2)N(t + T_a/2) - Z(t - T_a/2)N(t - T_a/2)}{2Z(t)N(t) + Z(t + T_a/2)N(t + T_a/2) + Z(t - T_a/2)N(t - T_a/2)}. \quad \text{(A.16)}$$

Simplifying the expression for the ratio becomes more difficult as more terms are added into the fit model. In fact, no analytic expression is written down for the ratio formulation of Equation A.16, but fortunately the fitting algorithm can resolve $R(t)$ on a bin-by-bin basis. Using this more complete fit model for the positron time spectrum results gives greater confidence in the fit results.

A.2 Ratio Bin Errors

Since the constituent datasets of the ratio construction are statistically independent, standard error propagation is used to determine the errors on the bins in the ratio histogram.

$$\begin{aligned} \sigma_R(t)^2 &= \left(\frac{\partial R(t)}{\partial V(t)}\right)^2 \delta V(t)^2 + \left(\frac{\partial R(t)}{\partial U(t)}\right)^2 \delta U(t)^2 \\ \delta U(t)^2 &= \delta n_1(t)^2 + \delta n_2(t)^2 = n_1(t) + n_2(t) = U(t) \\ \delta V(t)^2 &= \delta n_3(t)^2 + \delta n_4(t)^2 = n_3(t) + n_4(t) = V(t) \end{aligned} \quad \text{(A.17)}$$

Calculating derivatives and combining terms gives

$$\sigma_R^2 = \frac{4UV}{(V+U)^3} = \frac{1-R^2}{V+U} \tag{A.18}$$

Appendix B

Pileup Corrected Bin Errors

Before pileup subtraction, bin errors on the standard T-Method histogram are given by

$$\sigma_i = \sqrt{N_i} \tag{B.1}$$

where i is the bin index and N_i is the number of counts in bin i. After pileup subtraction, the number of counts in each bin is modified. Specifically, in the shadow method used in this analysis, pileup events are statistically constructed and subtracted from the data. The pileup spectra are formed as a sum of doublets minus singlets,

$$PU = D - S.$$

In the case of no energy threshold, this would mean each pileup event contributes one doublet subtracts two singlets, resulting in a net loss of one count. However, since there is an energy threshold, singlets will be be included in the count only if they pass the energy threshold. For example, imagine a trigger pulse of 1.6 Gev that has a pulse within its shadow window of 1.5 GeV. If the energy threshold for inclusion in the histogram is 1.7 GeV, a doublet will be constructed but neither singlet will be included in the pileup histogram. In this case a net count of 1 is added to histogram PU. In general, there are four types of pileup events that depend on the energy threshold. These configurations are listed as I, II, III, and IV in table B.1.

Given the different possible combinations, the counts that go into the pileup histogram are

$$PU = \sum (N_D - N_S) = -N_I + N_{IV} \tag{B.2}$$

Pileup is the sum of type I and IV doublets. Type II and III doublets contribute zero net counts to the

Doublet type	Singlet energy $> E_{min}$	PU	Net counts
I	S_1 & S_2	D - S_1- S_2	-1
II	S_2	D - S_2	0
III	S_1	D - S_1	0
IV	neither	D	+1

Table B.1

pileup histogram. From Equation B.2, the errors are then

$$\sigma_{PU} = \sqrt{N_I + N_{IV}}. \tag{B.3}$$

The pileup corrected time spectrum consists of subtracting constructed pileup from the measured positron spectrum,

$$N_{corr} = N_{meas} - PU \tag{B.4}$$

There are counts in N_{meas} that are also in PU. We can write N_{meas} in terms of singlets above threshold to separate out the different contributions.

$$N_{meas} = N_{NP} + 2N_I + N_{II} + N_{III} \tag{B.5}$$

where N_{NP} are singlets that do not get used in the pileup construction. Then

$$\begin{aligned} N_{corr} &= N_{NP} + 2N_I + N_{II} + N_{III} + N_I - N_{IV} \\ &= N_{NP} + 3N_I + N_{II} + N_{III} - N_{IV} \end{aligned} \tag{B.6}$$

The bin errors on the pileup corrected histograms are then

$$\sigma_{N_{corr}} = \sqrt{N_{NP} + 9N_I + N_I I + N_I I + N_I V} \tag{B.7}$$

Using Equation B.6 to plug in for N_{NP} in Equation B.7 let's us remove the dependence of the errors on the unknown quantity N_{NP}. The result is then

$$\begin{aligned} \sigma_{N_{corr}} &= \sqrt{N_{corr} + 6N_I + 2N_{IV}} \\ &= \sqrt{N_{corr}} \cdot \sqrt{1 + (6N_I + 2N_{IV})/N_{corr}} \\ &= \sqrt{N_{corr}} \cdot \sqrt{\gamma(t)} \end{aligned} \tag{B.8}$$

where $\gamma(t)$ is the pileup correction factor. Since the counts that contribute to the pileup correction factor are small and decay at approximately the muon lifetime, the change in the errors in less than 1% at the fit start time.

For the Ratio Method, we can apply the result above to the individual sub-datasets, as in

$$\sigma_{n_i} = \sqrt{n_{i,corr}} \cdot \sqrt{\gamma(t)} \tag{B.9}$$

The correction factor can be written as $\gamma(t) = 1 + \gamma e^{-t/\tau}$, where the constant $\gamma \approx 0.5\%$ is derived in Reference [63]. Recasting the errors on the histograms n_i, we get

$$\begin{aligned} \delta U(t)^2 &= \delta n_1(t)^2\gamma(t) + \delta n_2(t)^2\gamma(t) = \gamma(t)(n_1(t) + n_2(t)) = \gamma(t)U(t) \\ \delta V(t)^2 &= \delta n_3(t)^2\gamma(t) + \delta n_4(t)^2\gamma(t) = \gamma(t)(n_3(t) + n_4(t)) = \gamma(t)V(t) \end{aligned} \tag{B.10}$$

Plugging these new errors on U and V into Equation A.17, σ_R^2 becomes

$$\gamma(t) \cdot \sigma_R^2 \tag{B.11}$$

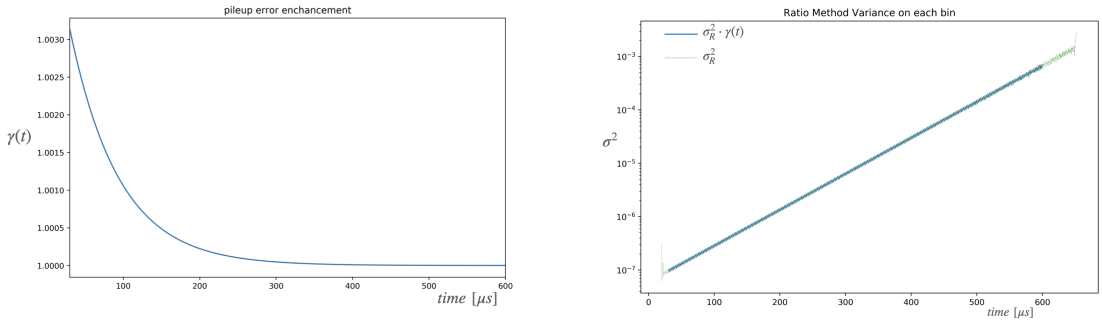


Figure B.1: Left: Pileup uncertainty enhancement factor. Right: Bin uncertainties in the Ratio Method histogram. Applying the pileup uncertainty enhancement to the nominal bin uncertainties has a marginal effect.

As in the case of the T-Method histograms, the uncertainty enhancement is small and decaying with the muon lifetime. Figure B.1 illustrates the effect of the pileup enhancement on the bin errors in the Ratio Method.

Appendix C

Correlation Matrices

Correlation matrices for the 21-parameter fits to the 2C, 2D, 2E and 2F datasets are included here. Most parameters are uncorrelated with each other. Frequencies and phases of the same oscillation tend to be somewhat correlated. Likewise, amplitudes and lifetimes of the same oscillation tend to be somewhat correlated. In the case of the $g-2$ oscillation, R is strongly correlated with ϕ_0. No other parameters are significantly correlated to R.

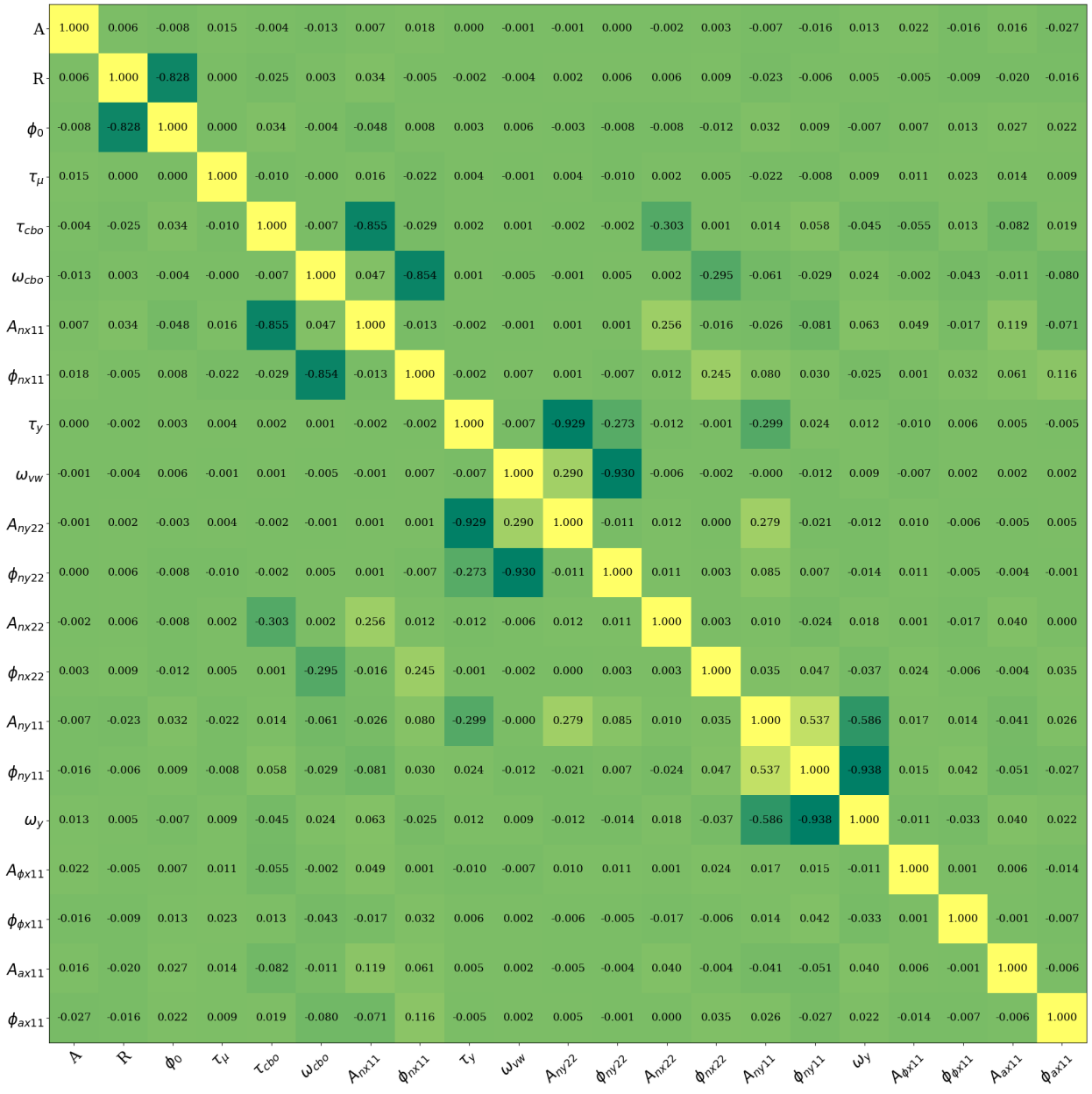


Figure C.1: Correlation matrix for the 21-parameter Ratio fit to the 2C dataset. R is 82.8% correlated to the $g-2$ phase, ϕ_0. All other parameters are effectively uncorrelated with R.

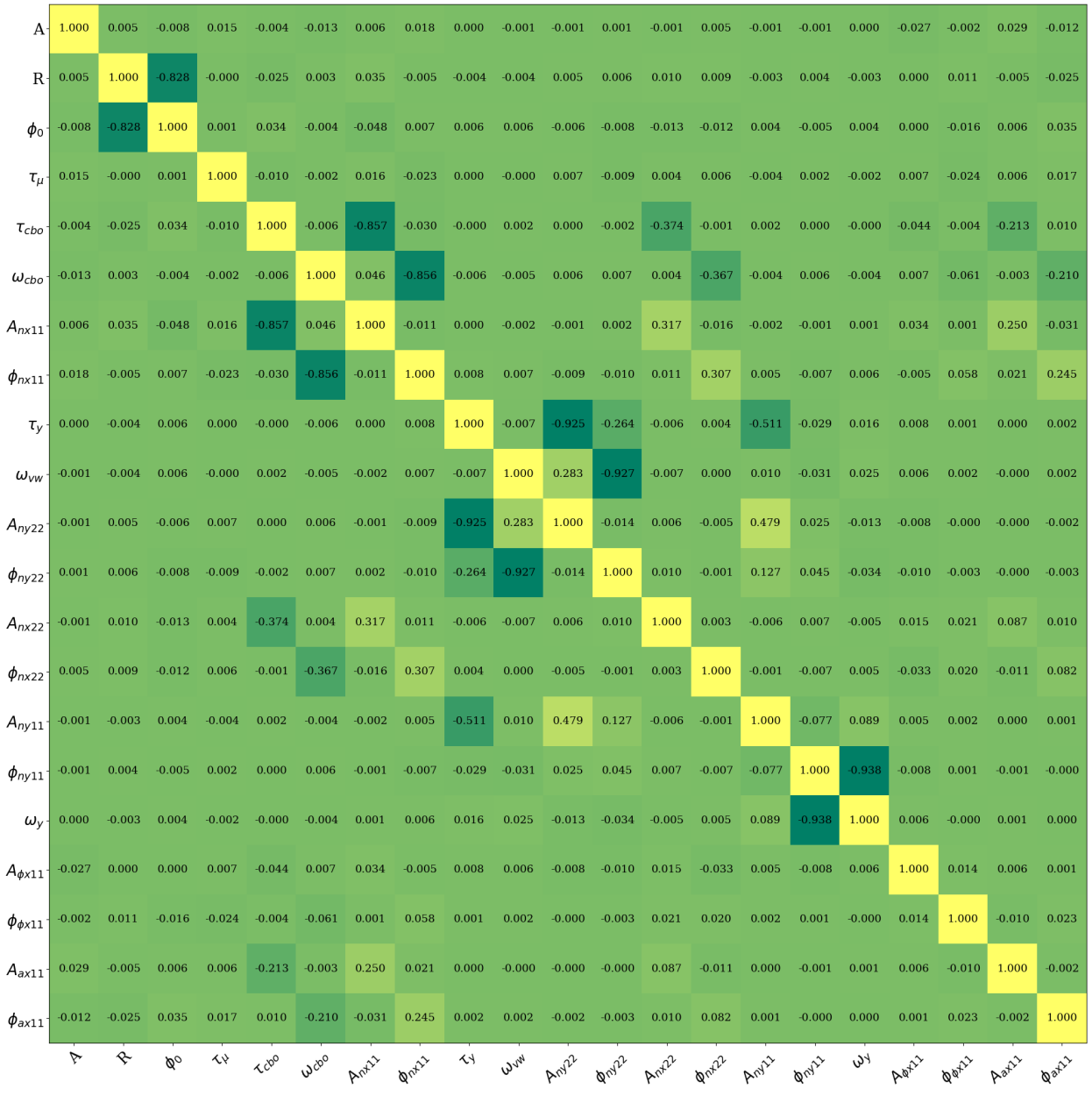


Figure C.2: Correlation matrix for the 21-parameter Ratio fit to the 2D dataset. R is 82.8% correlated to the $g-2$ phase, ϕ_0. All other parameters are effectively uncorrelated with R.

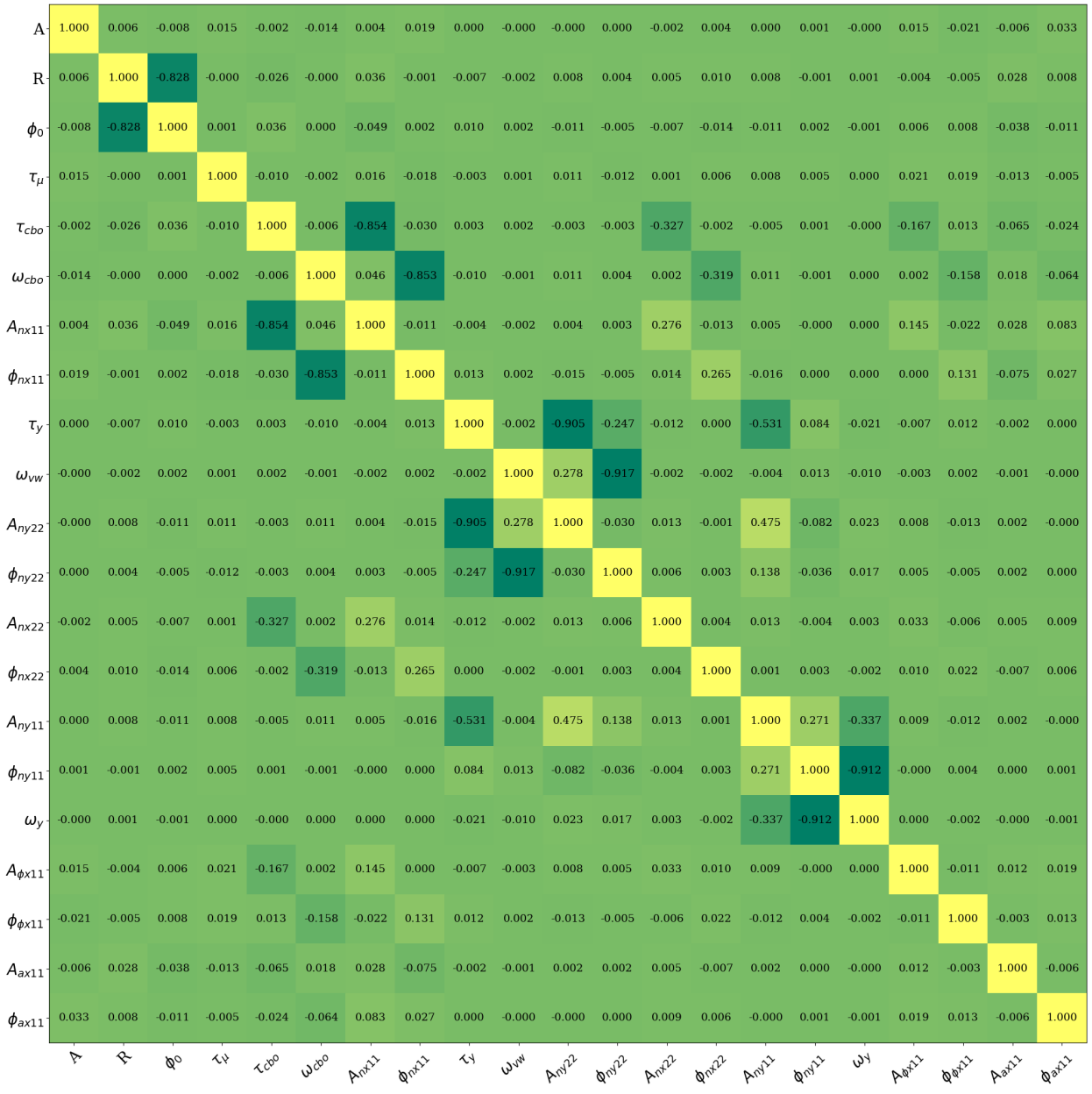


Figure C.3: Correlation matrix for the 21-parameter Ratio fit to the 2D dataset. R is 82.8% correlated to the $g-2$ phase, ϕ_0. All other parameters are effectively uncorrelated with R.

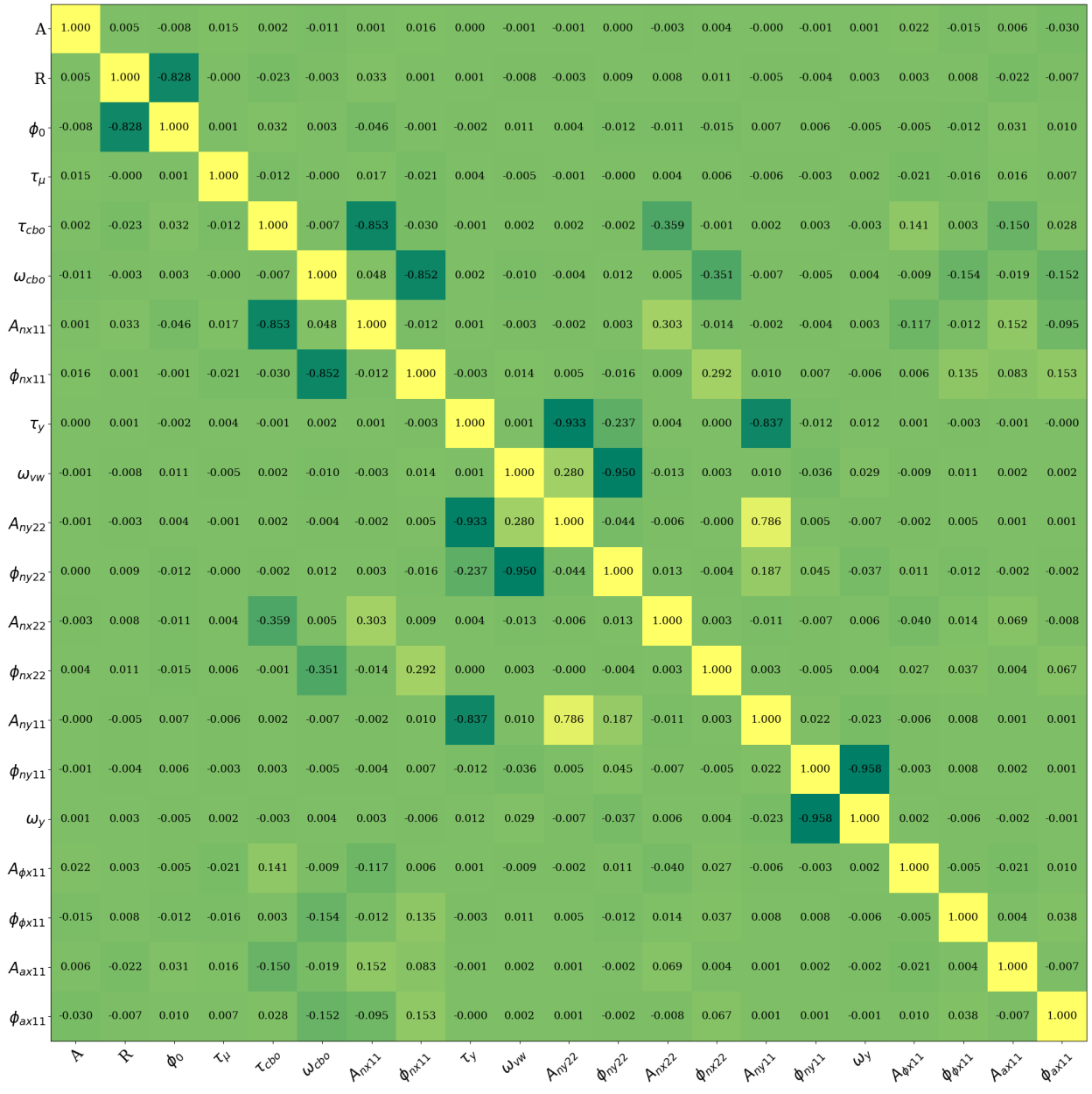


Figure C.4: Correlation matrix for the 21-parameter Ratio fit to the 2D dataset. R is 82.8% correlated to the $g-2$ phase, ϕ_0. All other parameters are effectively uncorrelated with R.

Bibliography

[1] B. Abi et al. Measurement of the positive muon anomalous magnetic moment to 0.46 ppm. *Phys. Rev. Lett.*, 126:141801, Apr 2021.

[2] C. Polly. *A Measurement of the Anomalous Mangetic Moment of the Negative Muon to 0.7 ppm.* PhD thesis, University of Illinois at Urbana-Champaign, 1996.

[3] T. Aoyama et al. The anomalous magnetic moment of the muon in the standard model. *Physics Reports*, 887:1–166, Dec 2020.

[4] T. Aoyama et al. Quantum electrodynamics calculation of lepton anomalous magnetic moments: Numerical approach to the perturbation theory of qed. *Progress of Theoretical and Experimental Physics*, 2012.

[5] Peter J. Mohr, David B. Newell, and Barry N. Taylor. Codata recommended values of the fundamental physical constants: 2014. *Rev. Mod. Phys.*, 88:035009, Sep 2016.

[6] M. et al Tanabashi. Review of particle physics. *Phys. Rev. D*, 98:030001, Aug 2018.

[7] Richard H. Parker, Chenghui Yu, Weicheng Zhong, Brian Estey, and Holger Müller. Measurement of the fine-structure constant as a test of the standard model. *Science*, 360(6385):191–195, Apr 2018.

[8] T. Aoyama, T. Kinoshita, and M. Nio. Theory of the anomalous magnetic moment of the electron. *Atoms*, 7(1), 2019.

[9] T. Aoyama, T. Kinoshita, M. Nio, and M. Hayakawa. Complete tenth-order qed contribution to the muong-2. *Physical Review Letters*, 109(11), Sep 2012.

[10] A. Czarnecki, W. Marciano, and A. Vainshtein. Refinements in electroweak contributions to the muon anomalous magnetic moment. *Phys. Rev. D*, 67:073006, Apr 2003.

[11] Muon g-2 theory, 2020.

[12] A. Keshavarzi, D. Nomura, and T. Teubner. $g-2$ of charged leptons, α(mz2), and the hyperfine splitting of muonium. *Physical Review D*, 101(1), Jan 2020.

[13] C. Gnendiger et al. The electroweak contributions to $(g-2)_\mu$ after the higgs-boson mass measurement. *Physical Review D*, 88(5), Sep 2013.

[14] T. Aoyama et al. Phys. rev. d97, 36001. 2018.

[15] A. Keshavarzi et al. Phys. rev. d97, 114025. 2018.

[16] C. Gnendiger et al. Phys. rev. d88, 53005. 2013.

[17] A. Czarnecki and W. Marciano. Muon anomalous magnetic moment: A harbinger for "new physics". *Phys. Rev. D*, 64:013014, Jun 2001.

[18] M. Pospelov. Secluded U(1) below the weak scale. *Phys. Rev. D*, 80:095002, Nov 2009.

[19] G. Charpak et al. Measurement of the anomalous magnetic moment of the muon. *Physical Review Letters*, 6(3):128, 1961.

[20] J. Bailey et al. Precision measurement of the anomalous magnetic moment of the muon. *Physics Letters B*, 28(4):287–290, 1968.

[21] J. Bailey et al. Final report on the cern muon storage ring including the anomalous magnetic moment and the electric dipole moment of the muon, and a direct test of relativistic time dilation. *Nuclear Physics B*, 150:1–75, 1979.

[22] G.W. Bennett et al. Final report of the e821 muon anomalous magnetic moment measurement at bnl. *Physical Review D*, 73(7):072003, 2006.

[23] T. Albahri et al. Measurement of the anomalous precession frequency of the muon in the Fermilab Muon $g-2$ Experiment. *Phys. Rev. D*, 103:072002, Apr 2021.

[24] T. Albahri et al. Magnetic-field measurement and analysis for the muon $g-2$ experiment at fermilab. *Phys. Rev. A*, 103:042208, Apr 2021.

[25] Muon g 2 Collaboration. Beam dynamics corrections to the run-1 measurement of the muon anomalous magnetic moment at Fermilab. *Phys. Rev. Accel. Beams*, 24:044002, Apr 2021.

[26] P. A. Zyla et al. Review of Particle Physics. *PTEP*, 2020(8):083C01, 2020.

[27] J. Grange et al. Muon $(g-2)$ technical design report. 2015.

[28] A. Chapelain. Attempt at estimating the beam-line positron contamination from fiber harps data and simulation. *E989 DocDB 10758*, 2018.

[29] A. Fienberg. *Measuring the Precession Frequency in the E989 Muon $g-2$ Experiment.* PhD thesis, University of Washington, 2019.

[30] A. Fienberg. The ω_a measurement. *E989 DocDB 12873*, 2018.

[31] D. Rubin. Evolution of the muon distribution in the g-2 ring. *E989 DocDB 4098.*

[32] N. Kinnard. *Muon Spin Precession Frequency Extraction and Decay Positron Track Fitting in Run 1 of the Fermilab Muon $g-2$ Experiment.* PhD thesis, Boston University, 2020.

[33] E. Konopinski. The experimental clarification of the laws of beta-radioactivity. *Annual Review of Nuclear Science*, 9(1):99–158, 1959.

[34] G.W. Bennett et al. Statistical equations and methods applied to the precision muon (g-2) experiment at bnl. *Nuclear Instruments and Methods in Physics Research*, 579(3):1096–1116, 2007.

[35] R. Osofsky. Improving magnetic field uniformity in the $g-2$ storage ring. *E989 DocDB 12497.*

[36] M. Smith. *Developing the Precision Magnetic Field for the E989 Muon g–2 Experiment.* PhD thesis, University of Washington, 2017.

[37] A. Chapelain. Development of the electromagnetic calorimeter waveform digitizers for the Fermilab Muon $g-2$ experiment. *PoS*, EPS-HEP2015:280, 2015.

[38] A. Fienberg et al. Studies of an array of PbF2 Cherenkov crystals with large-area SiPM readout. *Nuclear Instruments and Methods in Physics Research Section A: Accelerators, Spectrometers, Detectors and Associated Equipment*, 783:12–21, 2015.

[39] K.S. Khaw et al. Performance of the Muon $g-2$ calorimeter and readout systems measured with test beam data. *Nuclear Instruments and Methods in Physics Research*, 945:162558, 2019.

[40] A. Anastasi et al. The laser control of the Muon $g-2$ experiment at fermilab. *Journal of Instrumentation*, 13(02):T02009–T02009, feb 2018.

[41] K. Labe. E989 Clock System Manual. *E989 DocDB 10995*, 2018.

[42] W. Gohn. Data Acquisition with GPUs: The DAQ for the Muon $g-2$ Experiment at Fermilab. *PoS*, page 174, 2016.

[43] K. Labe and D. Sweigart. Reconstruction East. *E989 DocDB 16351*, 2019.

[44] J. Kaspar et al. Design and performance of sipm-based readout of pbf2 crystals for high-rate, precision timing applications. *Journal of Instrumentation*, 12(01), 2017.

[45] P. Girotti. Laser corrections for Run 2/3. *E989 DocDB 23357*, 2020.

[46] J. Crnkovic et al. Lost muon study for the muon g-2 experiment at fermilab. In *8th InternationalParticle Accelerator Conference (IPAC 2017).*

[47] F. Farley. Pitch correction in (g-2) experiments. *Physics Letters B*, 42(1):66–68, 1972.

[48] D. Seleznev. Extraction of the Muon Beam Frequency Distribution via the Fourier Analysis of the Fast Rotation Signal. *E989 Note 130.*

[49] H. Binney. Measurement of the Phase-Momentum Correlation Lost Muon Systematic Error. *E989 Note 248*, 2020.

[50] J. Crnkovic. Data Based Estimate of Differential Decay Effect. *E989 DocDB 24300.*

[51] D. Sweigart. *A Measurement of the Anomalous Precession of the Positive Muon.* PhD thesis, Cornell University, 2020.

[52] C. Green et al. The *art* framework. *Journal of Physics: Conference Series*, 396(2):022020, dec 2012.

[53] J. Kindem. *The anomlalous magnetic moment of the positive muon.* PhD thesis, University of Minnesota, 1998.

[54] S. Ganguly, J.D. Crnkovic, K. T. Pitts, and C. C. Polly. Lost Muon Studies for the Muon g-2 Experiment at Fermilab. In *Proc. 9th International Particle Accelerator Conference (IPAC'18), Vancouver, BC, Canada, April 29-May 4, 2018*, number 9 in International Particle Accelerator Conference, pages 3573–3576, June 2018. https://doi.org/10.18429/JACoW-IPAC2018-THPAK139.

[55] S. Ganguly. Muon losses: Data vs MC. *E989 DocDB 11340*.

[56] H. Binney. Lost Muon Bump Update. *E989 DocDB 19724*, 2019.

[57] Fermilab Computing. User's Guide for SAM.

[58] J. Mott. *UW Tracking Analysis Elog 205*, 2020.

[59] W. Morse. Voltage Change on Quad Electrodes. *E989 DocDB 11352*, 2017.

[60] J. Mott. *UW Tracking Analysis Elog 206*, 2020.

[61] L. Duong. The Ratio (Orlov-Kindem) Method. *E821 Note 366*, 2000.

[62] L. Duong. *A Precise Measurement of the Anomalous Magnetic Moment of the Positive Muon*. PhD thesis, University of Minnesota, 2001.

[63] J. Paley. *Measurement of the Anomalous Magnetic Moment of the Negative Muon to 0.7 Parts Per Million*. PhD thesis, Boston University, 2004.